Coplanar Anode Implementation in Compressed Xenon Ionization Chambers

by

Scott Douglas Kiff

A dissertation submitted in partial fulfillment
of the requirements for the degree of
Doctor of Philosophy
(Nuclear Engineering and Radiological Sciences)
in the University of Michigan
2007

Doctoral Committee:

Associate Professor Zhong He, Chair
Professor Frederick D. Becchetti, Jr.
Professor Ronald F. Fleming
Associate Professor David K. Wehe

ACKNOWLEDGEMENTS

I would first like to thank Prof. Zhong He for guiding my education over the past four years. I have appreciated his willingness to help when I needed it most, allow me to try new ideas when I had them, and help me grow as an engineer. I expect that I will still be learning from him years from now.

Professors Franklyn Clikeman, Chan Choi, and Martin Lopez de Bertodano of Purdue University have supported me for nearly a decade now, and for that I am most grateful. Prof. Choi first encouraged me to pursue a Ph.D. when I did not believe I was capable; Prof. Clikeman, Ed Merritt of Purdue, and Dr. Robert Bean of Idaho National Laboratory introduced me to the wonderful worlds of radiation detection and nuclear reactors. Prof. Bertodano guided me through the bumpy ride I call my master's thesis—and showed me how to apply the course material I had been learning to actual problems.

Professors Glenn Knoll and David Wehe of the University of Michigan have taught me in courses and provided much technical insight and career guidance over the past few years. In addition, they must be very pleased that I am finally graduating so that I will stop asking for scholarship and employment reference letters, letters for which I express my deepest gratitude. Along this line, Ed Birdsall and Peggy Gramer, also of the University of Michigan, have provided countless hours of assistance with computers, facilities, scholarship applications, and navigating Rackham's sea of requirements.

Drs. Aleksey Bolotnikov, Royal Kessick, Pavel Kiselev, and Prof. Gary Tepper have all been invaluable resources in my helping me fill my detectors and understand experimental results. The National Science Foundation has provided me great flexibility in pursuing my education via a Graduate Research Fellowship. I am appreciative of their support and their willingness to continue to fund me after changing universities and research topics not once, but twice.

The members of my research group have always been very supportive and helpful: Profs. Jim Baciak and Ling-Jian Meng; Drs. Clair Sullivan, Cari Lehner, Feng Zhang, Dan Xu, and Keitaro Hitomi; soon-to-be Dr. Ben Sturm; Jim Berry; and Steve Anderson, Miesher Rodrigues, Weiyi Wang, Yuefeng Zhu, Willy Kaye, and Chris Wahl. Thanks for years of help on the Shockley-Ramo Theorem, Geant4, LabVIEW, Matlab, peak-hold circuits, and just being good friends.

Dave Griesheimer, Heath Hanshaw, Troy Becker, Greg F. Davidson, and Jeremy Conlin have provided countless instances of help with topics such as math and computer programming, in addition to great conversations and good friendships. My experience at Michigan would not have been half as enjoyable without them.

Will, Kirsten, Caitlin, and Mackenzie White (and now Victoria!) deserve special mention in these acknowledgements. How could Natalie and I have survived Ann Arbor without Will's grilling expertise? Or brownies? Thanks for almost three years of letting us spend weekends with you, decompressing, playing with Caitlin and Mackenzie, and knowing exactly what best friends are.

Non-Wolverine friends have also been very supportive over the years: Mat Mattox, Tony Waltman, and Jason Larson have been wonderful friends since high school, and will continue to be for decades; Natalie Yonker, Josh Walter, Derek Hounshel, and Travis Croy made long hours in the Nuclear Engineering Building very enjoyable.

Finally, I could not have completed this dissertation and the years of education leading up to its culmination without the unconditional support of my family: my parents, my sister Cori, Dennis and Ella, and Lindsay and Eric (and Emma!). Above all I would like to thank Natalie, who has been by my side every step of the way for more than a decade showing her love and support. These family members have truly helped me through the periods of stress, shared with me in elation, and have worked overtime to try to figure out exactly what nuclear engineering is.

TABLE OF CONTENTS

LIST OF FIGURES

LIST OF TABLES

CHAPTER 1

INTRODUCTION

1.1 Properties of High-Pressure Xenon

High-pressure xenon (HPXe) gas is an attractive gamma-ray detection medium due to several of its physical and nuclear properties. HPXe has a large detection efficiency for gamma ray energies on the order of 100s of keV, due to its large atomic number (Z = 54), which translates into high photoelectric absorption and Compton scattering cross sections; in addition, the detection efficiency of these devices is enhanced by the ability to use a high density of up to about 0.6 g/cm^3 [1], coupled with a large sensitive volume (commonly on the order of liters). The mean energy to produce an ionization in HPXe, commonly referred to as *w*, is relatively low for a gas, less than 21 eV per electron-ion pair [1]. In addition, the Fano factor for HPXe is quite good, measured near 0.13 ± 0.1 [2]. These two parameters combine to give HPXe ionization chambers an attractive theoretical energy resolution of about 0.5% full-width at half-maximum (FWHM) at 662 keV, the energy corresponding to gamma rays emitted from a ^{137}Cs source.

There are other attractive qualities of HPXe as well. For example, HPXe ionization chambers are ideal for use in uncontrolled environments, as detector response has been shown to be uniform over large temperature ranges (20°C to 170°C) [3]; this is postulated to be due to the relatively large ionization energy of xenon, which makes thermal excitation a negligible factor [4]. HPXe ionization chambers can be operated at room temperature, so there is no need for providing a cooling source. Unlike solid detection media that derive their radiation detection capabilities from their crystal structure, HPXe performance is not degraded by high radiation fluences, although

exposure to a significant neutron flux can activate the xenon. The primary isotopes responsible for this induced activity are ^{129}Xe and ^{131}Xe, which form metastable states that decay with half-lives on the order of ten days via transitions of 236 and 164 keV, respectively [5, 6]. As a final point, the cost of HPXe gas is relatively inexpensive, around $1/g, resulting in a cost per detector on the order of 100s of U.S. dollars [7].

Radiation interactions in HPXe create many excited Xe_2 molecules; these molecules return to the ground state by emitting detectable scintillation light [8-10]. Ionized atoms that recombine at the ionization site will also create scintillation. This scintillation light can be useful in marking gamma-ray interactions for timing purposes. Also, electrons accelerated through high electric fields in Xe also cause scintillation light emission, and this light can be collected by a photomultiplier tube for spectroscopic purposes. For this to occur, the ratio of the electric field magnitude to the atom density of the gas must be greater than the scintillation threshold of 2.9×10^{-17} V/cm^2 [11].

A summary of important properties of compressed xenon gas is listed in Table 1.1, along with a comparison to other common detection media [8, 12]. In this table, common thicknesses of the media being compared to HPXe are given, along with an equivalent thickness of HPXe that counts the same number of particles per unit area for a planar gamma ray source emitting photons of energy 662 keV. This measure probably underestimates the true efficiency of HPXe by neglecting the larger area of the detector.

Table 1.1. A comparison of common radiation detection media.

Medium	Density (g/cm^3)	Atomic numbers	*w* (eV/ion pair)	Thickness (cm)	Equivalent HPXe (cm)
NaI:Tl	3.67[1]	11, 53	~100	5.08	37.5[2]
Ge	5.33[3]	32	2.98[3]	2	20.2[2]
$Cd_{0.8}Zn_{0.2}Te$	6[3]	48, 30, 52	5.0[3]	1	11.8[2]
HgI_2	6.4[3]	80, 53	4.3[3]	1	14.9[2]
HPXe	0.5	54	21.9	—	—

[1] From G.F. Knoll, Radiation Detection and Measurement, 3rd ed., Table 8.3.

[2] Photon attenuation data is from the NIST XCOM database.

[3] From G.F. Knoll, Radiation Detection and Measurement, 3rd ed., Table 13.3.

1.2 Possible Applications for HPXe Ionization Chambers

HPXe is an attractive detection medium for applications that require a detector to have better energy resolution than can be provided by scintillators, better efficiency than semiconductors can offer, and the ability to operate without cooling and over a wide range of temperatures without sacrificing performance. One of the applications of greatest interest is detecting special nuclear materials (SNM) at borders and ports. Detecting SNM requires sensitivity over a large energy range, from ^{235}U gamma rays with energies between 150 and 200 keV up through 2614 keV, a gamma emitted by the ^{232}Th and ^{232}U daughter product ^{208}Tl [13]. The energy resolution must be good enough such that nearby gamma lines do not interfere in measuring the lines of interest; for example, the ^{235}U 186-keV complex should be distinguishable from the 238-keV line originating from U and Th daughter products [14]. HPXe chambers have been identified as a medium that can meet the sensitivity and resolution needs for SNM monitoring.

A second application of great interest for HPXe is environmental monitoring of radioactive soils, which can demand good spectroscopic performance while lowering a detector into a borehole up to depths of 250 feet [15]. Radioisotopes of interest in these surveys typically emit gammas with energies on the order of 1 MeV, and a detector must be sensitive enough to measure contaminant activities near the naturally-occurring background level, while rugged enough to withstand dose rates near 1 krad/hr in highly contaminated soils. Temperatures in deep wells can rise above 100°C, complicating the measurement [16]. HPXe chambers can provide the combination of sensitivity, temperature stability, and energy resolution needed for these activities.

There has been interest in using HPXe ionization chambers for basic science as well. Researchers have been attracted by the combination of high efficiency, good energy resolution, and radiation hardness offered by HPXe, sending multiple HPXe detectors into orbit aboard the MIR space station to study gamma-ray bursts [17, 18]. Another interesting proposal for HPXe chambers is to assist in the investigation of neutrinoless double beta decay, a study which can help to understand the neutrino and quantify its mass [19]. ^{136}Xe, which constitutes 8.9% of natural Xe, undergoes the $2\beta(0\nu)$ transition with the large decay energy of 2.48 MeV. Because HPXe ionization chambers contain large quantities of gas, are simple to build and operate, have good

energy resolution near 2.5 MeV, and are the source of these decays, they have been explored by two different groups for $2\beta(0\nu)$ experiments [19, 20].

1.3 Development of Gridded HPXe Ionization Chambers

The first attempts at using HPXe ionization chambers in the early 1980s employed ionization chambers with Frisch grids. The purpose of these grids is to shield the anode from signal generation when charges drift through the bulk of the detector; a detailed discussion will follow in Chapter 2 of this dissertation. Electrostatically shielding the anode from moving charge in a large portion of the detector results in a net anode signal that is generally only a function of the number of electrons collected by the anode. A Frisch grid is typically formed from several small-diameter wires (10s to 100s of μm); many of these wires are stretched to form a parallel array or a crossed grid, which is placed near the anode. A crossed Frisch grid structure is shown in Figure 1.1 [15]. Wire separation is often an order of magnitude larger than the individual wire diameter. The grid is held at a potential that: (i) creates a sufficient electric field in the ionization region, which is between the cathode and the Frisch grid, to minimize electron attachment; and (ii) minimizes charge collection on the Frisch grid itself. To accomplish the latter goal, the electric field magnitude between the Frisch grid and the anode typically must be significantly greater than the field magnitude in the ionization region [21].

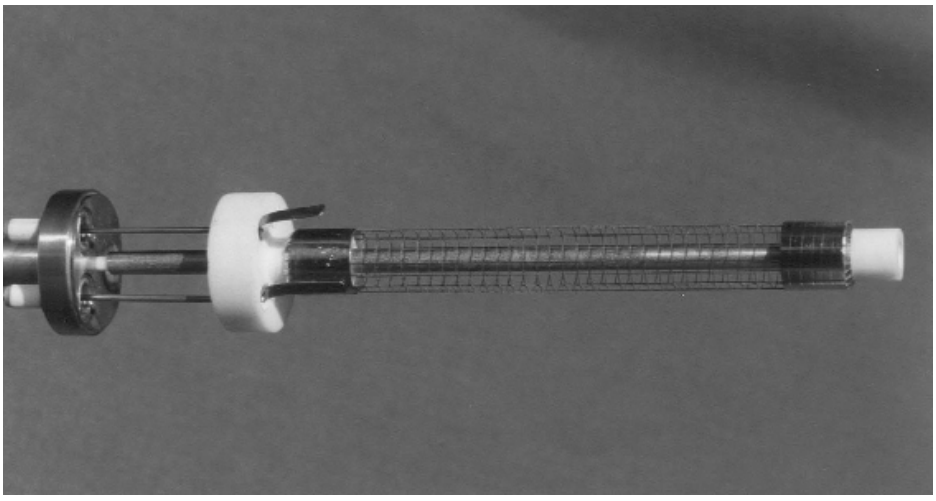

Figure 1.1. A typical Frisch Grid with 4 wires/mm pitch.

Gridded ionization chambers can be found in two distinct geometries: planar and cylindrical. Planar configurations are convenient due to the uniform axial electric field; it will be shown later that the charge created at the site of the initial interaction recombines at a rate that is a function of the electric field. Thus, recombination effects can be made uniform throughout the device. Cylindrical chambers are advantageous because of the inherent lower capacitance this geometry affords, the potential for a balanced tradeoff of charge induction and charge recombination as a function of radial interaction location, and better utilization of the xenon gas space.

1.3.1 Planar Configuration

The first reported measurements using a HPXe ionization chamber were done with a planar configuration [22, 23]. The HPXe ionization chamber incorporated a dual drift region, utilizing a central anode plane with sensitive volumes on either side, accompanied by a cathode/Frisch grid set on each side of the anode plane. This geometry creates a uniform electric field, which is maintained near the periphery via the use of several drift electrodes. Each half of the active volume had a 93-mm diameter and a 38-mm height. The gas density was 0.2 g/cm^3, and the gas was doped with a small amount of H_2 gas (0.5%). The incorporation of a small admixture of H_2 will be discussed in more detail in Chapter 7; the purpose is to greatly increase the drift velocity of electrons with only a small effect on other gas properties. The reported energy resolution measured with this chamber was 2.7% FWHM for a ^{137}Cs gamma-ray source. By measuring the pulse amplitude as a function of the applied drift field and extrapolating to the infinite field case, *w* of HPXe was measured with this system to vary from (21.4 ± 0.3) eV/ion pair to (20.8 ± 0.3) eV/ion pair as the gas pressure was increased from 1.5 to 4.1 MPa [23].

This geometry was also used in several other investigations [5, 6, 17, 19, 24-32]. A significant limitation of the Frisch grid was revealed by measurements using a dual-drift-region HPXe chamber aboard the MIR space station: the measured energy resolution degraded from 2.0% FWHM at 1 MeV during pre-flight testing to between 3 and 4% during flight, a change attributed to microphonic vibrations aboard MIR [26].

Using another planar configuration, Bolotnikov et al. studied the effects of gas pressure on the measured energy resolution of HPXe ionization chambers [33]. The geometry used was very basic, with a single anode, cathode, and Frisch grid forming a single drift region. In this case, a ^{207}Bi source was implanted on the surface of the cathode; ^{207}Bi has a relatively complex energy spectrum due to its multiple modes of radioactive decay [34]. Increasing the Xe gas density had no measurable effect on the energy resolution below 0.6 g/cm^3, as the resolution was only a function of charge carrier statistics. However, above a density of 0.6 g/cm^3 the energy resolution degraded rather quickly. After ruling out other possible sources of this degradation, the reason was found to be ion-electron recombination along the δ-ray tracks in the ionization clouds. This physical limitation on energy resolution is responsible for the optimal HPXe density being just underneath this threshold of 0.6 g/cm^3. This result was verified by Levin, Germani and Markey [2, 20], who concluded that the intrinsic energy resolution is not governed by Poisson statistics at high pressures.

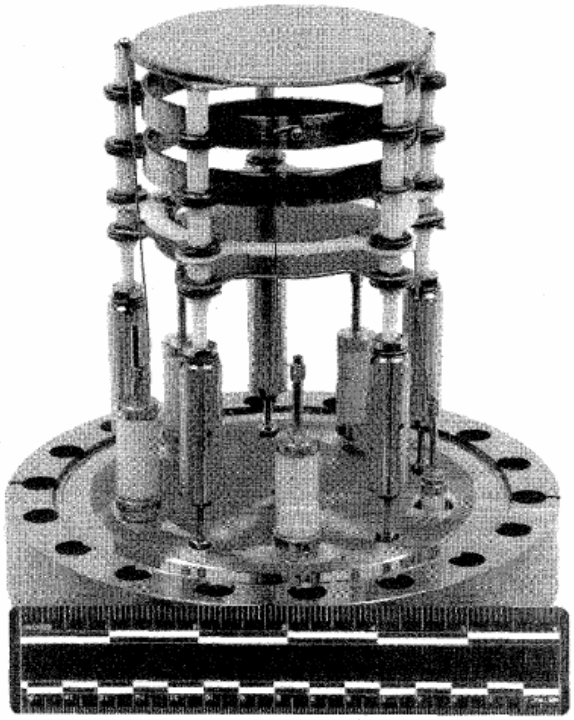

Figure 1.2. A parallel-plate gridded HPXe chamber. The vertical columns are supporting (from top) the cathode, two field rings, the Frisch grid (white border), and the anode. The cathode and anode are separated by 6.0 cm; the sensitive volume's diameter is 6.4 cm.

Finally, Mahler et al. [35] used a single-drift-region HPXe ionization chamber to produce a spectrometer for field use with a sensitive volume of 160 cm^3; this detector is shown in Figure 1.2. With a collimated source in a lab setting, this device achieved 2% FWHM resolution at 662 keV, which is the best reported resolution to date in a planar HPXe ionization chamber. By maintaining the high voltage across capacitors and charging the system for 10 seconds every 30 minutes using batteries, a portable device was created that measured 2.5% FWHM at 662 keV without source collimation. Biasing the detector in this fashion reduced peak broadening from high-voltage ripple.

1.3.2 Cylindrical Configuration

Ulin et al. [36, 37] desired a HPXe chamber with high detection efficiency and good energy resolution. To achieve these goals, a cylindrical geometry utilizing a Frisch grid was developed; in the cylindrical geometry, the sensitive volume is a larger fraction of the total gas space, and the Frisch grid makes charge induction on the anode more uniform as a function of radial position. This detector's sensitive region was 36 cm in length and 8.3 cm diameter, a sensitive volume of nearly 2 liters. The chamber was filled with Xe+0.2%H_2 for improved electron drifting, limiting the total electron drift time to less than 10 μs. The measured energy resolution for a ^{137}Cs gamma source was 4.0% FWHM, including electronic noise. Nearly identical HPXe chambers were developed [4-6, 13, 28, 31, 32, 38-41], with Ulin et al. achieving 2.9% FWHM at 662 keV using a HPXe volume of just over 5 liters [38].

The next notable set of improvements in cylindrical gridded HPXe detectors focused on reducing Frisch grid microphonics [29, 30, 42, 43]. In this study the overall detector dimensions and fill gas were nearly identical to the previous study, but the grid was formed from a metallic foil of thickness 0.25 mm, into which a regular pattern of 5-mm by 3-mm holes was introduced for transparency to drifting electrons; the rectangular holes were separated by 0.25 mm in either direction. This is a sturdier design than an array of individual wires, and vibrational issues were expected to diminish via this design. In addition, the grid was not just held in place at each end, but also at two intermediate locations using ceramic insulators. This feature further dampened microphonic vibrations. The total energy resolution at 662 keV was measured as 2.4%

and 2.2% FWHM for irradiation of the chamber side wall and end, respectively. Bolotnikov and Ramsey investigated a similar mesh design at about the same time, with nearly identical energy resolution measurements [44, 45]. The development of sturdier shielding grids led to many subsequent investigations [14, 15, 31, 32, 46-48]. A schematic of a typical cylindrical gridded chamber is shown in Figure 1.3; this chamber includes an electroformed mesh grid with periodic spacers for microphonic reduction [49].

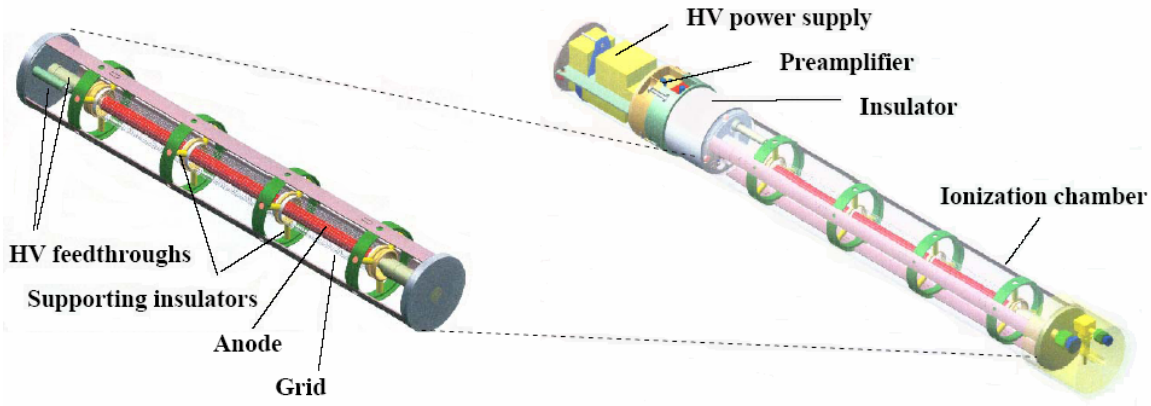

Figure 1.3. A typical cylindrical gridded HPXe chamber. The cathode is not shown.

1.4 Alternatives to the Gridded HPXe Ionization Chamber

Obviously the energy resolution using gridded HPXe chambers can be quite good, as shown in the previous section. Often, good chambers will obtain total energy resolution values near 2% FWHM at 662 keV for small-dimension chambers (drift distances of around 2 cm), or between 3-4% FWHM for larger chambers (drift distances of about 5 cm). Although the measured resolution is superior to most scintillators, and is approaching the performance of good room-temperature semiconductor devices, there is still a large gap between the measured performance and the theoretical energy resolution of 0.5% FWHM at 662 keV. It is commonly thought that microphonic vibration of the Frisch grid plays a major role in resolution degradation; this effect was measured using a planar gridded detector and found to be significant [26].

In addition, design, construction, and operational problems can be associated with Frisch grids. The grid wire diameter, spacing, and operating potential must be chosen correctly: the grid must effectively shield the anode from electron motion in the ionization region, while being transparent to electrons so that as many as possible pass through the grid and generate a signal on the anode. Assuming the anode is grounded, the optimal grid bias is a function of the bias applied to the cathode due to electrostatics, as well as the gas density because of charge recombination arguments (i.e., the optimal grid bias will balance any spatial variation in charge recombination with the shielding inefficiency of the grid). Finally, Frisch grids can be difficult to manufacture due to their delicate wires, the need for exact geometry, and the need for proper tensioning of each wire.

Given these drawbacks to Frisch grid use, much effort has been spent on finding a viable functional alternative. Some efforts have focused on simple two-electrode devices due to their simplicity; some try to use pulse height compensation based upon electron drift time; some use more complex anode structures that function as both the signal electrode and the shielding grid; and there have also been efforts to use post-measurement data processing to filter out the effects of grid vibrations. Each technique will be discussed in more detail in this section, along with its inherent advantages and disadvantages.

1.4.1 Uncompensated Cylindrical Two-Electrode Devices

Two-electrode devices, which are the simplest detectors because they have only a single anode and a single cathode, were among the earliest HPXe detectors developed. Because there is no Frisch grid, microphonic degradation of energy measurements should be minimized, and the reduced detector capacitance should improve electronic noise. On the other hand, the lack of a Frisch grid means the pulse amplitude will be a function of the gamma's interaction location, but this can be somewhat improved by using a cylindrical geometry.

Dmitrenko et al. reported results on a two-electrode device in 1981 [50]. This detector was expected to exhibit energy resolution of 5.4% FWHM, calculated by considering a uniform distribution of photoelectric absorptions and the radial distribution

of the induced charge on the anode. Using a gas mixture including 0.3% H_2, the measured energy resolution was 6% FWHM for a ^{137}Cs gamma-ray source. Other published experiments have been based upon this initial design [3, 4, 16, 28-32, 41, 51-53].

The best result in this geometry was reported by Dmitrenko et al. [3], and separately by Ulin et al. [16]. This device had a measured energy resolution of 4% FWHM at 662 keV. In addition, a temperature study was done in which the detector response was measured from 20ºC to 170ºC; the maximum temperature was determined by the integrity of the pressure vessel under increasing gas pressure. This study found no measurable shift in photopeak centroid, and the energy resolution remained unchanged within experimental error.

1.4.2 Rise Time-Compensated Cylindrical Two-Electrode Devices

The drawback of uncompensated cylindrical two-electrode devices is that there is a significant dependence of the signal amplitude upon the gamma-ray interaction location. To remove this detrimental effect, the pulse rise time can be measured and used to separate events into small bins based upon electron drift distance. Pulse height normalization can then be applied to each bin.

This technique was first reported by Bolotnikov and Ramsey [44, 45]. A HPXe chamber of diameter 4.8 cm was used, and events with rise times measured between 14 and 16 μs were accepted. This rise time envelope corresponded to events near the cathode, and resulted in an energy spectrum with a measured resolution of 2.5% FWHM at 662 keV. For comparison, without rise time selection the energy spectrum of all events in the device had a measured resolution of about 8% FWHM. A similar attempt by Troyer, Keele, and Tepper had less-satisfactory results [54]. Smith, McKigney, and Beyerle measured the rise time of each event and implemented a correction factor derived from simulations to correct the pulse amplitude [55].

Measuring the rise time of the anode's preamplifier signal can introduce a significant amount of uncertainty into the compensation process. Because electrons drift quite slowly through Xe or even Xe+H_2 mixtures, and generally the noise fluctuations are fairly significant when compared to the signal amplitude, good estimations of the start

and stop time can be difficult to make. One alternative is to use scintillation light as the start and stop signals to measure electron drift time. There are a few technical challenges in this method [56]: coupling a photomultiplier tube to a high-pressure chamber is difficult; the emitted scintillation light is in the ultraviolet range, meaning wavelength shifters or UV-sensitive photocathodes must be used; and finally the number of scintillation photons emitted is quite small, so the system must be sensitive to a small signal.

Lacy et al. employed scintillation light collection for electron drift time measurement in a cylindrical HPXe ionization chamber [11]. A light guide was mated to a transparent window at one end of the chamber, and a photomultiplier tube was coupled to this light guide. Scintillation light created from de-excitation and recombination at the ionization site marked the start time of the signal. As a result of a very large electric field near the anode surface—over 50 kV/cm—electrons drifting near the anode transferred enough energy in collisions to create excitations that emitted scintillation light upon returning to ground state. This secondary scintillation marked the end of electron drift. By correcting the anode pulse amplitude according to the measured drift time, the energy spectrum for ^{22}Na improved from essentially no 511 keV photopeak without pulse-height correction to 2.3% FWHM when the correction was employed.

1.4.3 Non-Standard Geometries

One of the earliest attempts at using HPXe ionization chambers had a geometry akin to the familiar silicon drift detector [57]. In this case, a chamber was created between two plates separated by 1.5 cm. Distributed along the plates were conducting strips placed at regular intervals and biased in uniform steps. An anode wire was placed midway between the two plates near one end of the detection volume. The electrostatic field created in this detector focused any electrons onto the anode, and the geometry removed nearly all position dependence of the anode signal due to the excellent electrostatic shielding provided by the field electrodes. The measured energy resolution was 3.1% FWHM using a ^{137}Cs gamma-ray source. Because of the small width of this chamber, a significant x-ray escape peak was measured. A similar principle was employed by Bolotnikov et al., who implemented a Frisch collar design in HPXe [58].

The drawback of these concepts is that charge induction requirements prevent the use of large-volume chambers.

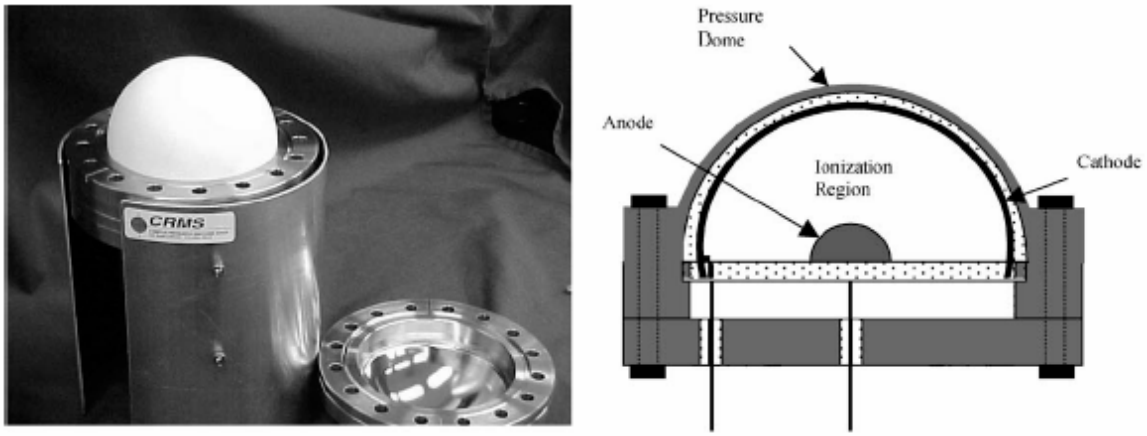

Figure 1.4. A hemispherical HPXe chamber. The cathode diameter is 3.5 inches.

One interesting attempt at using a novel geometry, shown in Figure 1.4, was reported by Kessick and Tepper [59]. This detector employed a hemispherical geometry, which is theoretically superior to the cylindrical two-electrode chamber in terms of charge-induction uniformity throughout the entire device: this is because in a cylinder the charge-induction deficit will go as $\ln(r)$, whereas in a spherical geometry the deficit goes as $1/r$, which is more ideal. The source of this advantage ends up being the Achilles' heel of the hemispherical detector: the electric field goes as $1/r^2$, which means that an extremely large bias must be applied across the detector to obtain an acceptably small recombination rate and a uniform drift velocity throughout the detector. The measured energy resolution for a ^{137}Cs spectrum was 6% FWHM.

1.4.4 Multiple-Anode Chambers

Another category of detectors that can be used to replace the Frisch grid in HPXe ionization chambers is multiple-anode chambers. In the designs reviewed, the presence of more than one anode channel allows the anode to function both as the readout channel and as the Frisch grid, since the recorded anode signal is largely independent of charge

movement in most of the detection volume. These designs tend to be relatively insensitive to microphonics.

The first attempts at incorporating multiple-anode structures into HPXe chambers were in the Ph.D. dissertation of Sullivan [60, 61]. These detectors implement coplanar anodes, which are shown in Figure 1.5. Coplanar anode theory will be discussed in great detail in Chapter 2, so only a brief description will be given now. Coplanar anodes are two symmetric anodes that are operated with a potential bias applied between them: electrons are thus preferentially collected on one anode, deemed the *collecting anode*. Because of the charge induction properties of this device, the collecting anode's induced charge less that on the noncollecting anode gives a resulting signal that is functionally equivalent to the electrostatic shielding of a Frisch grid. Therefore, if the anode structure is resistant to microphonics, a vibration-resistant alternative to the Frisch grid can be employed. The major disadvantage to coplanar-anode HPXe chambers is that since there are two readout channels and thus two preamplifiers, the net subtracted signal suffers from increased electronic noise due to the presence of two noise sources instead of just one.

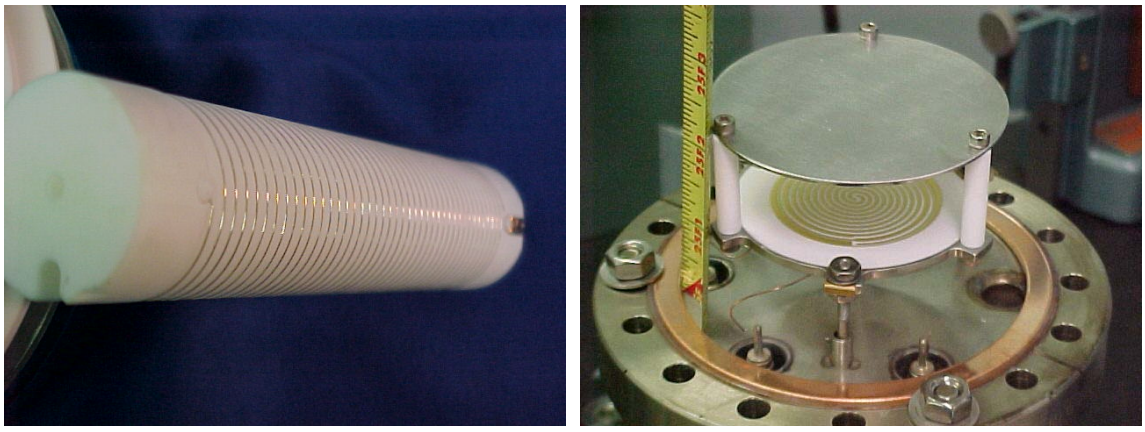

Figure 1.5. The first coplanar anodes implemented in HPXe. (Left) The helical anode. (Right) The spiral anode and the back of the cathode.

The first coplanar anode design incorporated two wires wound around an insulating rod, forming a double-helical anode structure. This rod formed the central axis in a cylindrical HPXe ionization chamber. The best energy resolution obtained with this

device was 9% FWHM using a ^{137}Cs point source, which is quite poor: this was postulated to result from incomplete charge collection on the collecting anode. A second anode design incorporated two spiraling anode strips metallized on a flat ceramic plate; this anode was used in a parallel-plate HPXe chamber. The best energy resolution obtained from this detector with a ^{137}Cs source was 12.7% FWHM.

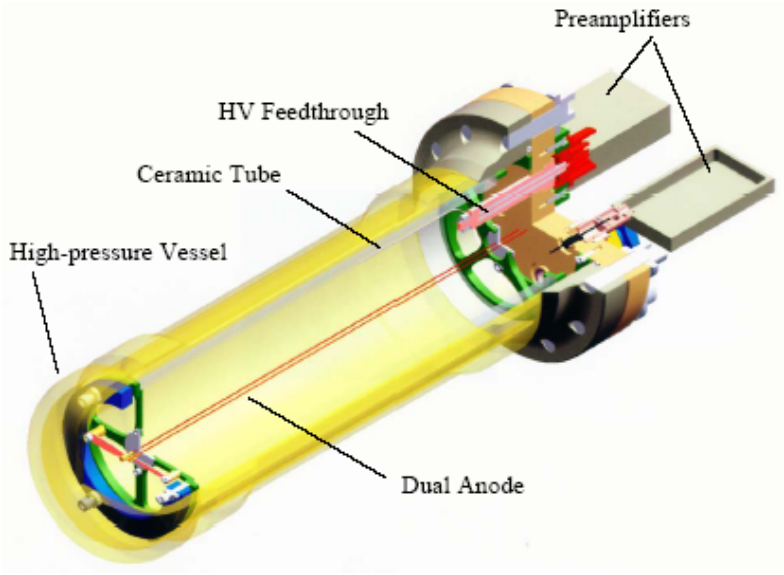

Figure 1.6. A schematic of the DACIC concept with two symmetric anode wires.

A concept similar to coplanar anodes was introduced by Bolotnikov et al. [58, 62], termed the dual-anode cylindrical ionization chamber, or DACIC. In the DACIC two symmetric anode wires are stretched axially in a cylindrical HPXe ionization chamber; these anode wires are each displaced from the central axis by a few millimeters. A schematic of the DACIC is shown in Figure 1.6. These wires electrostatically shield one another, thereby functioning as the Frisch grid; unlike the Frisch grid, the wires can be made relatively large to dampen microphonic vibration. The DACIC concept has been used in subsequent investigations [63, 64]. The DACIC has been operated in two modes: quasi-coplanar readout and individual wire readout.

Quasi-coplanar operation refers to the fact that although one anode signal is subtracted from the other, there is no potential bias applied between the anode wires, as traditional coplanar theory requires: thus, collection on only one anode wire cannot be

ensured. Besides the potential for charge sharing, the charge induction on the two anodes is not uniform in the anode plane, contributing to unnecessary peak broadening. Finally, if an incoming gamma ray creates energy depositions on opposite sides of the chamber, those two charge clouds will be collected by opposing wires, and the subtraction step will greatly reduce the recorded energy. Given these facts it is not surprising that the energy resolution was 4% FWHM at 662 keV, which is not as good as gridded chambers can achieve.

Using individual wire readout introduces a tradeoff: because the final signal includes only one noise source instead of the combination of two independent noise sources, electronic noise is expected to be lower. However, the charge induction is expected to be even less ideal, although the lack of signal subtraction removes problems related to signal amplitude reduction when charge is shared or a multiple-site event is recorded. The measured energy resolution was 3% FWHM at 662 keV, a good result for a large-diameter chamber.

Finally, a pixellated anode has been proposed for use in HPXe ionization chambers by Feng et al. [65]. In this concept, four 1-cm x 1-cm pixels are metallized onto an insulating plate and form independent anode channels; they are separated by a noncollecting grid which is held at a lower potential to help focus the electrons onto the pixels. Each pixel is electrostatically shielded from charges moving far from the anode plane by the neighboring pixels and noncollecting grid. This concept introduces more readout complexity due to the potential for many independent anodes, but is resistant to microphonic degradation. In addition, electronic noise broadening is expected to be quite small due to the relatively small detector capacitance for each pixel. Finally, this concept has the potential for three-dimensional position sensing of gamma-ray interaction positions, which would be a new contribution to HPXe ionization chambers.

1.4.5 Signal Noise Filtering

Seifert et al. took a different approach to the problem of microphonic degradation of energy spectra [66]. Instead of developing robust hardware to functionally replace the Frisch grid, signal noise filtering was applied using a standard gridded HPXe detector. Pulse waveforms were collected using LabVIEW and converted to frequency domain;

this allowed for investigation of the problematic frequencies arising from microphonics. Using digital filtering to remove each problematic frequency band individually, the detector's energy spectrum could be restored to its non-perturbed resolution when the system was exposed to only that particular driving frequency. It is unclear whether this method could be implemented in real time, or if it could be used when the detector is exposed to a broad range of driving frequencies. Nonetheless, the fact that this technique could effectively filter out the microphonic noise from a gridded detector is a noteworthy contribution. The principle advantage of this approach is that it can be used with standard hardware, so in this respect it is a very practical technique. The downside of this approach is the need for substantial computations to perform the noise filtering, which is unattractive because although a common detector can be used, it must now be attached to specialized data processing equipment, which will reduce operational flexibility.

1.5 Sensing the Gamma-Ray Interaction Position in HPXe

The gamma ray's interaction position can be useful information to collect. The interaction location might allow one to determine the direction of the incoming gamma rays; perform detector diagnostics, such as ensuring proper biasing and gas purity by looking at the distribution of interaction positions; or improve spectroscopic results by correcting pulse amplitudes based upon interaction positions, or possibly by rejecting events that register in undesired locations. Undesired locations might include volumes inside the detector where the electric field is known to be nonuniform, or possibly locations physically located outside the detector, which would indicate an improperly-recorded event.

There have been very few attempts at position sensing in HPXe ionization chambers; most have been in the last decade. Generally these methods fall into one of two broad categories: methods employing scintillation collection to convert drift time to interaction position, and methods using the ratio of signals on two or more electrodes to deduce the interaction coordinate. Many of the detectors mentioned in the previous section (Section 1.4) are capable in principle of some type of position sensing; however, only those experiments in which position sensing capabilities were explicitly reported are summarized here.

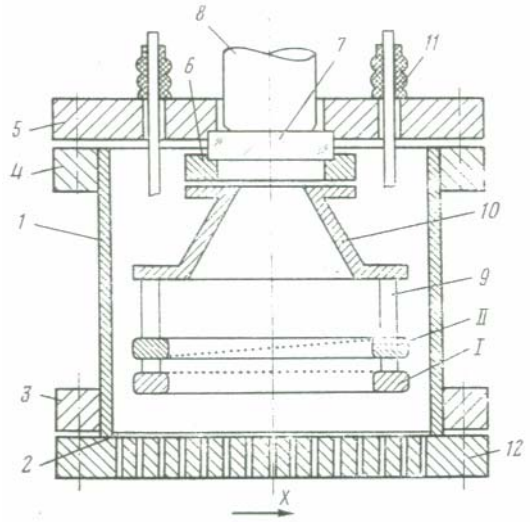

Figure 1.7. Position sensing along the X coordinate (as shown). Scintillation light is generated in the varying gap between electrodes I and II, then directed by a light guide (10) to a window (7) for collection by a photomultiplier tube (8).

1.5.1 Position Sensing with Scintillation Time Stamps

The first reported attempt at position sensing in HPXe was by Goleminov, Rodionov, and Chepel [67]. This detector utilized a single-drift-region planar HPXe chamber; the noteworthy design feature was that the spacing between the Frisch grid and anode was not uniform, but changed linearly as a function of lateral location. A photomultiplier tube was coupled to the detector, and by using an appropriate electric field between the Frisch grid and anode plane, scintillation light could be produced during an electron's full traversal of the gap. Thus, the length of the scintillation light pulse was linearly related to the position of the gamma ray interaction. A schematic is shown in Figure 1.7.

Tepper and Losee [56] reported a design incorporating a photomultiplier tube mated to a dual-drift-region planar HPXe chamber; only the initial scintillation light was measured in this system, with the end of the pulse determined by the anode signal formation. The authors pointed out that xenon scintillation light decays with two distinct decay times, a fast component at 2.2 ns and a slow component at 27 ns, and that heavy ion tracks have an enhanced fast component due to the higher ionization density. Thus, the scintillation pulse can be used to reject background events originating from cosmic

rays, in addition to converting total drift time to distance for calculating the interaction depth between the anode and cathode. It should be noted that no experimental results were reported from this system.

1.5.2 Position Sensing with Electrode Signal Ratios

Athanasiades, Lacy, and Sun conceived a cylindrical gridless HPXe chamber that utilizes a segmented cathode [68]. The central anode provides an estimation of the charge deposited in the detector, and the ratio between the charge induced on each of the six cathode strips and the anode can be used to localize the radial and azimuthal interaction coordinates. The calculated radial coordinate can then be used to correct the measured anode signal amplitude for the radial dependence of the induced charge. No experimental results were presented, but it is likely that problems might arise from two sources: (i) the authors assumed electronic noise from each channel would be quite low, but it seem likely that there will be a large capacitance between cathode strips that substantially increases electronic noise in those signal channels; and (ii) using the methodology presented it is difficult to know how multiple-site events would be registered.

A similar concept was employed in an experiment by Athanasiades et al. [69], but this detector used a single insulating cathode covered with a slightly conductive paint. Six pickup wires were placed just outside the chamber in 60° intervals. The overall position-sensing methodology remained the same as previously described. The position resolution was less than 2 mm FWHM in the radial direction, and between 5.6° and 7.2° FWHM in the azimuthal direction. This particular system likely performs better than the segmented cathode due to the small capacitance between pickup wires.

1.6 Objectives of This Work

The goal of this study is to develop a coplanar-anode HPXe chamber that provides competitive energy resolution while being insusceptible to microphonic degradation. It is felt that coplanar anodes, while being limited more severely by electronic noise than other configurations, provide a rigid structure that is easy to operate and has the potential for excellent signal amplitude uniformity throughout the entire

active volume. Coplanar anodes provide the ability to perform position sensing in a very straightforward manner, which will be demonstrated; this information is useful for device diagnostics and spectroscopic improvements, and position sensing can be performed with a coplanar-anode chamber more easily than any of the aforementioned position-sensing techniques. Finally, an essential point of this effort is to understand the contributions to photopeak broadening and to determine if these degradation sources can be suppressed. This will allow an understanding of whether coplanar anodes can provide an attractive alternative to gridded HPXe ionization chambers in the future.

The presentation of the aforementioned work in this dissertation will begin with a theoretical discussion of charge induction on detector electrodes, and discuss how coplanar anodes functionally replace the Frisch grid, as well as the premise for position sensing using coplanar anodes. Detector modeling will follow, with a description of the different simulations performed to accurately model detector response. Established theory and modeling results will then be applied to the detector design; the basic concept is discussed, as is electrode optimization and the critical biasing conditions for complete electron collection upon the desired electrode.

Detector filling will be discussed alongside the initial testing, with results from the first gamma-ray detection experiments. Position-sensing theory specific to this detector geometry is developed next, and its application to the experiment is presented alongside detailed simulations. Finally, the factors impacting photopeak energy resolution are investigated through a series of simulations and experiments to quantitatively determine the contribution of each source, and whether improvements can be made. The conclusions will follow, along with suggestions for future work.

CHAPTER 2

SIGNAL INDUCTION THEORY

2.1 Signal Induction on a Conductor by Moving Point Charges

Radiation interactions in ionization chambers create electron and positive ion distributions at the interaction site. To register an interaction, an electric field is applied across the detection volume, causing the electrons and ions to drift toward the anode and cathode, respectively. As these point charges move through the detector, they induce measurable charge on the electrodes. It is important to understand the dependence of this signal upon the instantaneous position of the point charges over the entire duration of charge movement: this information can then be used to extract the desired information of the initial radiation interaction.

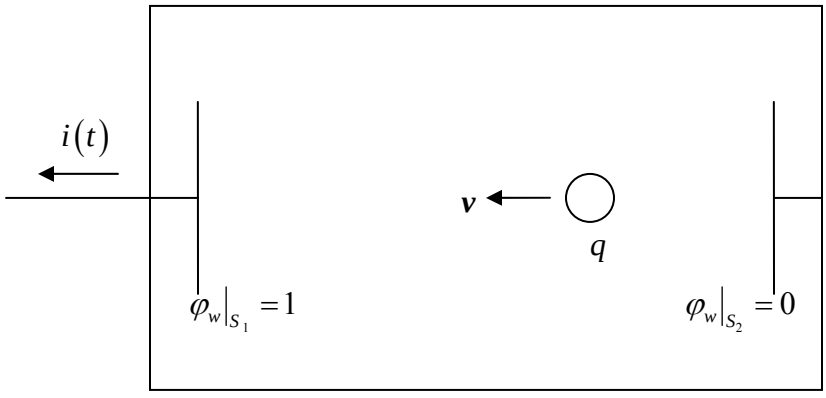

Figure 2.1. An illustration of important parameters in the Shockley-Ramo Theorem.

The instantaneous induced current on an electrode from the motion of a point charge is given by the Shockley-Ramo Theorem [70, 71]. This theorem is derived using

a conservation of energy argument by He [72], so a detailed derivation will not be presented at this time. Referring to Figure 2.1, the induced current $i(t)$ on an electrode due to a moving point charge q is proportional to the scalar product of the local particle velocity $\boldsymbol{v}$ and a parameter called the weighting field, denoted $\boldsymbol{E}_w$:

$$i(t) = q\boldsymbol{v} \cdot \boldsymbol{E}_w \tag{2.1}$$

The weighting field and a related parameter, the weighting potential φ_w, are governed by the equations and boundary conditions

$$\begin{aligned} \nabla^2 \varphi_w &= 0 \\ -\nabla \varphi_w &= \boldsymbol{E}_w \\ \varphi_w\big|_{S_1} &= 1 \\ \varphi_w\big|_{S_2} &= 0 \end{aligned} \tag{2.2}$$

In (2.2) the boundary conditions are defined along two surface sets: surface S_1 refers to the conducting surface—or surfaces, if multiple conductors form an electrode—for which the induced charge is of interest, while surface S_2 encompasses all other conducting surfaces. Equations (2.2) show that the weighting field and the weighting potential are calculated using the same equations as those governing the operating electric field and potential distributions in electrostatics, with the exceptions of the boundary conditions and the exclusion of space charge distributions (even if space charge is present, it does not affect the weighting potential distribution). The weighting potential φ_w is dimensionless; the weighting field $\boldsymbol{E}_w$ has units of inverse distance.

Physically, the weighting potential is the normalized instantaneous charge $Q(\boldsymbol{x})$ induced on surface S_1 by point charge q located at position $\boldsymbol{x}$. This can be easily seen after manipulating equation (2.1) into a form that is often more convenient for analysis, equation (2.4). Let us first convert the scalar product of the particle velocity and weighting field into an equivalent expression:

$$\begin{aligned} \boldsymbol{v}\cdot\boldsymbol{E}_{\boldsymbol{w}} &= \sum_k v_k E_{w,k} \\ &= \sum_k \frac{dx_k}{dt}\left(-\frac{d\varphi_w}{dx_k}\right) \\ &= -\frac{d\varphi_w}{dt} \end{aligned} \tag{2.3}$$

Since the induced current is the time derivative of the induced charge $Q(\boldsymbol{x})$, the final expression for the induced charge is simply equation (2.3) substituted into (2.1) and integrated over the drift time of the moving charged particle. This expression is

$$\Delta Q(\boldsymbol{x}) = -q\left[\varphi_w(\boldsymbol{x}) - \varphi_w(\boldsymbol{x}_0)\right] \tag{2.4}$$

It is important to point out that although charge induction on electrodes is determined by the weighting potential and is therefore purely geometrical in nature, charge motion through the detector is governed by the operating potential distribution and is therefore influenced not only by geometry, but also by the actual biases applied to the electrodes.

2.2 Single-Polarity Charge Sensing

Single-polarity charge sensing refers to signal generation that is only sensitive to the motion of either positive or negative charges (but not both). Often it is beneficial to design electrodes that are sensitive only to electron motion. Let us examine signals generated in a simple two-electrode detector as the motivation for single-polarity charge sensing. Then the Frisch grid and coplanar anodes will be introduced as methods of implementing single-polarity charge sensing.

2.2.1 Planar Two-Electrode Systems

Consider a gamma-ray interaction in a detector that creates n electron-ion pairs in a simple detector with a single planar anode located at $x = 1$ and a cathode forming the plane $x = 0$. The drifting electrons move toward the anode with total charge $q_e = -ne$,

where e is the elementary charge; the ions drift toward the cathode with a cumulative charge of $q_i = +ne$. Using the Shockley-Ramo Theorem in the form of equation (2.4), the total charge induced on the anode is the sum of the electron and ion contributions:

$$\begin{aligned}\Delta Q_{anode}(t) &= -q_e\left[\varphi_w\left(\mathbf{x}_e(t)\right)-\varphi_w\left(\mathbf{x}_0\right)\right]-q_i\left[\varphi_w\left(\mathbf{x}_i(t)\right)-\varphi_w\left(\mathbf{x}_0\right)\right] \\ &= ne\left[\varphi_w\left(x_e(t)\right)-\varphi_w\left(x_0\right)\right]-ne\left[\varphi_w\left(x_i(t)\right)-\varphi_w\left(x_0\right)\right] \\ &= ne\left[\varphi_w\left(x_e(t)\right)-\varphi_w\left(x_i(t)\right)\right]\end{aligned} \tag{2.5}$$

The weighting potential is calculated by setting the anode surface to unity and the cathode to zero. The solution is very simple in this geometry: $\varphi_w = x$.

If the electrons and positive ions are fully collected at the anode and cathode, respectively, then $\varphi_w\left(x_e\left(t\to\infty\right)\right)=1$ and $\varphi_w\left(x_i\left(t\to\infty\right)\right)=0$ in equation (2.5). In this case, then the final anode signal becomes $\Delta Q_{anode} = ne$; since the final signal is proportional to the number of initial ionizations, it becomes straightforward to make gamma-ray spectrometry measurements.

Often, though, full collection of the positive ions is impractical or even impossible. In gaseous detection media such as HPXe, positive ions have very small drift velocities, on the order of 1/1000th that of electrons. It becomes quite impractical to wait for complete ion collection, as this limits one to low count-rate applications and imposes difficult requirements upon the pulse-height measurement electronics. Therefore, it is desirable to measure the pulse only over a short duration, often just longer than the maximum electron collection time. In this case, however, the ion movement is negligible, and the induced charge on the anode is $\Delta Q_{anode} \cong ne\left(1-x_0\right)$. The final signal is now not only a function of the number of ionizations created in the radiation interaction, but also the interaction location; spectroscopy now is much more difficult, if possible at all.

2.2.2 The Frisch Grid

The Frisch grid [73] was developed to restore the proportionality between the anode signal and the amount of charge created in ionization chambers. Frisch grids are located near the anode (at location $x = 1 - P$ for this example) and are typically formed from several small-diameter wires; many of these wires are stretched to form a parallel array or a crossed grid. The effect of this grid is to create a nearly-ideal anode weighting potential distribution. The grid is operated at a potential that maintains a sufficient field at all points in the detector for full charge collection, and such that electrons can pass through the grid without premature collection.

To calculate the weighting potential, the anode is again set to unity, the cathode once more to zero; the Frisch grid is set to zero, since we are interested in the anode signal, and the Frisch grid is an independent electrode. The weighting potential distribution is now

$$\varphi_w(x) = \begin{cases} 0 & x \in [0, 1-P) \\ \dfrac{x-(1-P)}{P}, & x \in [1-P, 1] \end{cases} \tag{2.6}$$

A schematic of the gridded ionization chamber and the weighting potential distribution is shown in Figure 2.2.

Returning to the first line of equation (2.5), the anode signal is generally a summation of the electron and positive ion contributions. With a Frisch grid appropriately spaced from the anode, however, for nearly all interactions the point of origin will be between the Frisch grid and the cathode. For these events, the positive ions are always located in a region where the weighting potential is zero: it does not matter if the ion drift velocity allows for significant motion during the signal readout time or not. Thus, the Frisch grid is one configuration that allows for single-polarity charge sensing, since only the motion of electrons will generate an anode signal. Furthermore, as long as the electrons are created between the cathode and the grid, $\varphi_w(x_0) = 0$, the final anode signal is $\Delta Q_{anode} = ne$, and proportionality to the number of ionizations is restored.

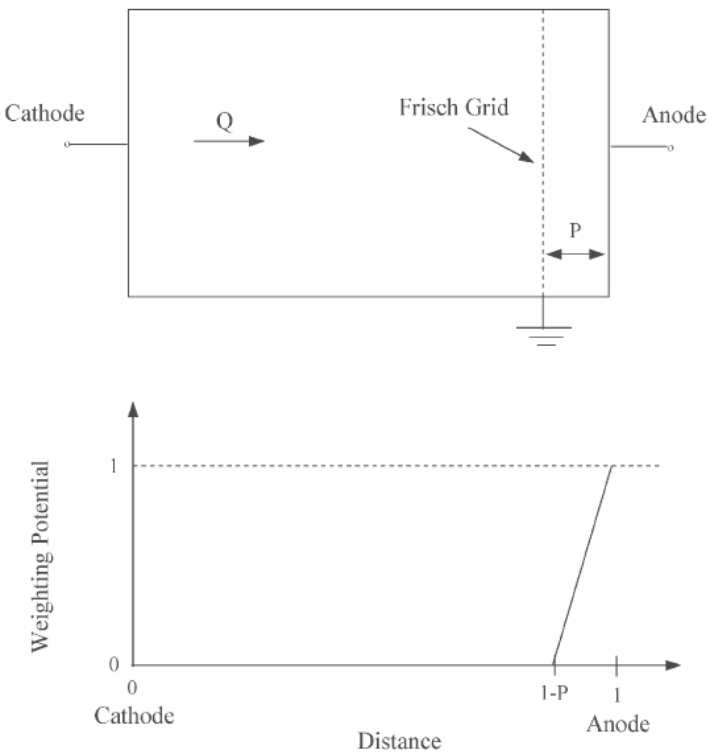

Figure 2.2. A schematic of a gridded ionization chamber (top). The weighting potential distribution in a gridded chamber (bottom).

2.2.3 Coplanar Grid Anodes

The coplanar grid was first reported by Luke in 1994 as a method of reproducing the effect of the Frisch grid in CdZnTe room-temperature semiconductor detectors [74]. CdZnTe suffers from a poor hole mobility-lifetime product, which creates the same position dependence as the slow drift of positive ions in HPXe gas. Due to the immense challenges of placing a Frisch grid electrode inside the semiconductor, an alternative was necessary.

Coplanar grid anodes are formed from a symmetric pattern of strips that are connected into two independent anode sets. See Figure 2.3 for a schematic of a detector utilizing coplanar anodes. As charges drift in the detector, they induce a signal on each anode as governed by the Shockley-Ramo Theorem. Figure 2.3 also shows the weighting potential of each electrode. The signal of either anode is obviously not independent of position. Yet, by designing the two anodes such that the induced charge is uniformly

distributed between the anodes throughout much of the volume, the weighting potential difference is independent of position, except for within a small region near the coplanar anodes. Electrons created through most of the detection volume will create an anode difference signal equal to their full charge if properly collected, and hole motion will not be sensed because holes will be moving through the bulk region. Thus, coplanar grid anodes can reproduce the single-polarity charge sensing functionality of a Frisch grid when signal subtraction is implemented.

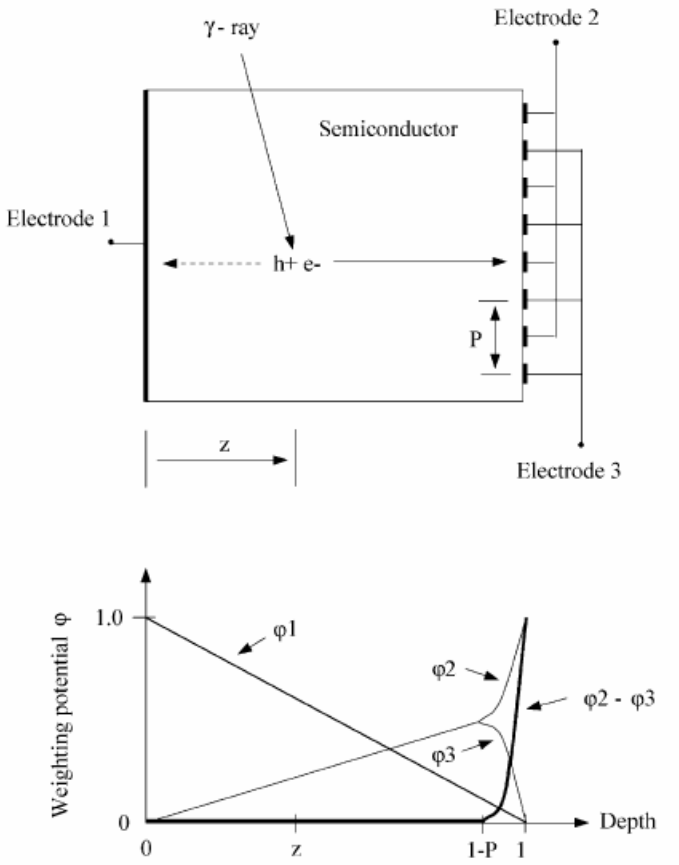

Figure 2.3. A coplanar grid anode with cathode 1, collecting anode 2, and noncollecting anode 3 (top). The anode weighting potential difference is largely independent of position (bottom).

Let us assume that N electrons are created by a gamma ray interacting in the detector. The signals on electrodes 2 and 3 (as shown in the figure) are

$$\begin{aligned}\Delta Q_2 &= -e\sum_{j=1}^{N}\left(\varphi_{2f}^{j}-\varphi_{2i}^{j}\right)\\ \Delta Q_3 &= -e\sum_{j=1}^{N}\left(\varphi_{3f}^{j}-\varphi_{3i}^{j}\right)\end{aligned} \tag{2.7}$$

In these equations, the subscripts *i* and *f* denote the weighting potential at the initial and final electron positions, and the superscript j refers to a specific particle. Due to the weighting potential uniformity, for nearly all interaction locations it is true that $\varphi_{2i}^{j}=\varphi_{3i}^{j}$ for every electron. The measured signal difference will then be

$$\begin{aligned}\Delta Q_{diff} &= \Delta Q_2 - \Delta Q_3\\ &= -e\sum_{j=1}^{N}\left(\varphi_{2f}^{j}-\varphi_{2i}^{j}\right)+e\sum_{i=1}^{N}\left(\varphi_{3f}^{j}-\underbrace{\varphi_{3i}^{j}}_{\varphi_{2i}^{j}}\right)\\ &= -e\sum_{j=1}^{N}\left(\varphi_{2f}^{j}-\varphi_{3f}^{j}\right)\end{aligned} \tag{2.8}$$

Equation (2.8) shows that $\Delta Q_{diff}=-Ne$ if every electron is collected at electrode 2, in which case $\varphi_{2f}^{j}=1$ and $\varphi_{3f}^{j}=0$ for each electron. Thus, every electron carries a weight of +1. However, if some electrons are collected at electrode 3, then for these particles $\varphi_{2f}^{j}=0$ and $\varphi_{3f}^{j}=1$, giving them a weight of -1. This will reduce the measured signal amplitude, which is undesirable. To counter this problem, a potential difference is applied between electrodes 2 and 3 that directs all electrons to electrode 2 for proper collection. Due to this biasing, electrode 2 is denoted the *collecting anode*, whereas electrode 3 is called the *noncollecting anode*. Thus, for coplanar grid anodes to be successfully employed, three conditions must be met: the two anodes must have uniform weighting potential through most of the volume; the measured signal must be the difference of the two anodes; and a bias must be applied between the anode sets to ensure proper electron collection.

The proper bias between the two anodes can be calculated theoretically using electrostatics. To fully collect all electrons at the collecting anode, there must be no field

lines inside the detector that originate at the noncollecting anode, since electron drift opposes the field line orientation. This condition can be ensured by finding the critical interanode bias that satisfies the condition

$$\left.\frac{\partial \varphi}{\partial z}\right|_{z=1} \leq 0 \tag{2.9}$$

under the center of a noncollecting anode strip, with the coordinate system used in Figure 2.3 [75]. In this equation φ refers to the operating potential distribution, not the weighting potential. The center of a noncollecting strip is the critical location due to the periodic nature of the potential distribution in planes that are parallel to the anode surface: if electrons created directly underneath the strip's center drift to the collecting anode, then electrons created at any other location will as well. Biasing the detector in accordance with equation (2.9) creates a saddle point directly underneath the noncollecting anode strip; electrons moving toward the noncollecting anode will reach a point at which they cannot continue toward that strip due to a falling potential, so they will drift upward in potential toward one of the neighboring collecting anode strips.

Equation (2.9) assumes that electrons exactly follow the field lines established by the applied electrode biases. This is generally a good assumption, as drifting electrons collide frequently with atoms in the detection medium, which causes the electron energy distribution to be nearly in thermal equilibrium with the atoms in the detection medium. A more exact approach is to change the critical condition slightly such that the potential drop between the saddle point and the noncollecting anode surface is at least as large as the kinetic energy of a drifting electron [76]. However, since electrons in common detectors are essentially in thermal equilibrium with the surrounding medium, their kinetic energies are well below 1 eV, and equation (2.9) is a justifiable approximation.

2.2.4 Position Sensing Using Coplanar Grid Anodes

Position sensing capabilities provide useful information for detector characterization and spectroscopic performance improvement. For example, the ability to observe spectral changes as a function of interaction location allows one to determine if

the detector has nonuniform material properties in the case of a semiconductor, or insufficiently-pure gas in the case of HPXe ionization chambers. Likewise, since electron trapping in a CdZnTe crystal or varying recombination in HPXe tend to shift the photopeak location as a function of interaction location, this effect can be compensated if the interaction coordinates can be calculated.

After first reporting the development of coplanar grid anodes, Paul Luke observed that although the difference of the anode signals is independent of interaction location, the amplitudes of the individual anode signals are a function of the interaction depth between the cathode and anodes, and that a ratio of these signals could provide information on the interaction depth [77]. He et al. pointed out that the cathode weighting potential in planar devices is a linear function of depth multiplied by the amount of drifting charge in the detector, whereas the individual anode signals can have slight variations for a given depth; thus, the ratio of the cathode signal to the subtracted anode signal gives a better approximation of the interaction depth [78]. Denoting the cathode and anode difference signals as S_{cat} and S_{sub}, respectively,

$$\frac{S_{cat}}{S_{sub}} \cong \frac{k_{cat} \cdot E_{\gamma} \cdot f(d)}{k_{sub} \cdot E_{\gamma}} \propto f(d) \tag{2.10}$$

where E_{γ} is the energy deposited by the gamma ray, k_{cat} and k_{sub} constants of proportionality between the deposited energy and the respective cathode and subtracted anode signals, d the interaction depth, and $f(d)$ a function of the depth, which is linear for a planar geometry. The measured depth should vary between 0 and 1, with near-anode events resulting in a depth near 0 and cathode-side events a depth near 1. The constants k_{cat} and k_{sub} should theoretically be equal if the same readout electronics are used for the cathode and subtracted anode signals; however, different equipment settings, such as different shaping time constants, may become necessary and destroy this equality. In addition, ballistic deficit may noticeably reduce the cathode signal gain relative to the anode signal, again resulting in unequal gain.

This depth-sensing technique could be applied to a gridded ion chamber, although the depth calculation would not be quite as accurate because the cathode signal varies linearly between the cathode and Frisch grid, but is zero between the grid and the anode. Thus, all interactions between the grid and the anode would give $d = 0$, and events in the rest of the detector would have to be scaled for the slight offset between the calculated and true depth.

It is interesting to note that equation (2.10) is valid only when the positive charge carriers are completely immobile; although this is not strictly true in practice, the better the approximation, the more accurate the calculated depth. The reason is that when the positive charge carriers move, they induce signals on the two anodes and the cathode; however, for most events in a coplanar-anode detector, the anode weighting potentials will be nearly identical along the entire path of the positive charge carriers, producing an anode difference signal that is insensitive to positive carrier motion. Therefore, the calculated depth for these events will be artificially large, since the cathode signal amplitude will increase with positive charge carrier motion, whereas the anode difference will generally be insensitive to those charges.

In this simple planar geometry, the positive carriers will induce a signal contribution that is uniform throughout most of the device, which will simply introduce a constant offset between the calculated and true depth. However, very near the cathode the positive carriers will reach the cathode and the cathode signal will equal E_γ in this region, leading to a calculated depth of $d = 1$ for all events where the positive carriers can be fully collected. As the positive carrier drift distance increases, so will the fraction of the detector where these charges are fully collected at the cathode, and the depth calculation method will become invalid. Events generated very near the anodes are unique in that the positive carriers can induce unequal charge on the coplanar anodes, albeit for a very short path length. This will reduce the measured depth offset by increasing the denominator as well as the numerator in equation (2.10).

Loss of charge to recombination or trapping should be proportional to the number of drifting charge carriers for all events at a given depth, assuming uniform material properties and only a depth variation in the electric field. As the depth is varied, this constant of proportionality can also change due to the position-dependence of charge

loss. This means that if the measured gamma-ray depositions are tallied in depth bins that are sufficiently fine, the location of gamma lines from one depth to the next will shift slightly due to this changing charge loss fraction. To correct this undesirable result, a constant gain can be applied to each depth bin that aligns common photopeak centroids. This gain will vary from one channel to the next, but will be valid from measurement to measurement as long as the state of the detector is not changed (i.e., different biasing conditions, a new fill gas mixture, or a different readout electronics configuration). The power of this technique is demonstrated in Figure 2.4, which shows both the spectrum as a function of depth and the effect of depth correction on the overall spectrum in a coplanar grid CdZnTe detector [79].

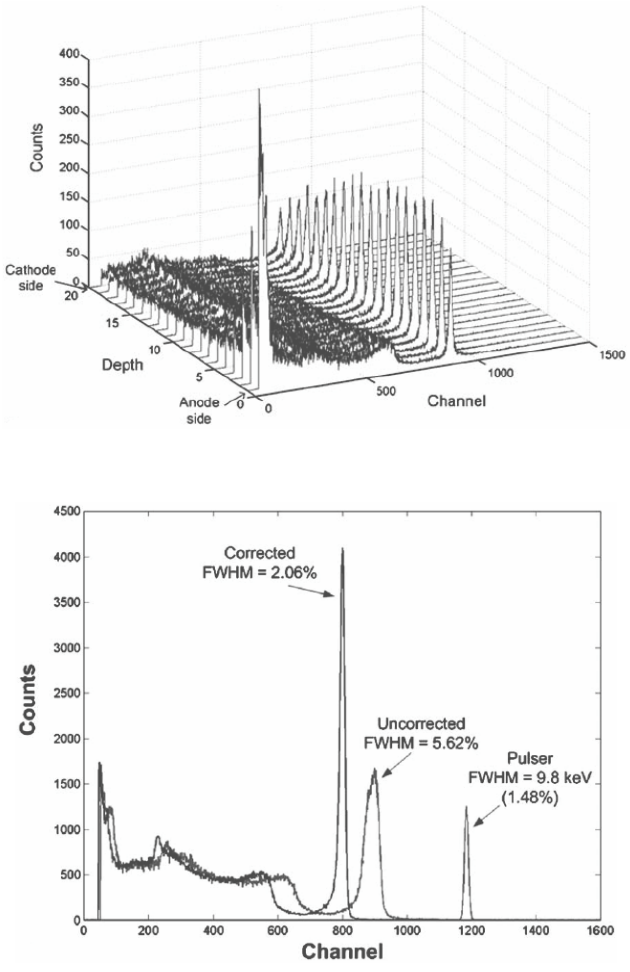

Figure 2.4. A ^{137}Cs depth-separated energy spectrum in coplanar-grid CdZnTe (top). Applying depth correction improves the energy resolution from 5.62% to 2.06% FWHM (bottom).

CHAPTER 3

DETECTOR DESIGN

3.1 Design Concept

The objective of this body of work is to develop a coplanar-anode HPXe chamber that provides competitive energy resolution (3.5 to 4.0% FWHM at 662 keV for large-diameter detectors) while being insusceptible to microphonic degradation of measured energy spectra. Previous coplanar-anode HPXe designs employed: (i) a helical anode in a cylindrical geometry and (ii) a spiral anode in a planar geometry [60, 61]. As discussed in Section 1.4.4, the helical anode structure suffered from incomplete charge collection problems that degraded the measured energy resolution, as electrons became trapped on the anode support column prior to arrival at the collecting anode. The spiral anode structure avoided the charge collection problems, but the planar geometry has two distinct disadvantages: the detector capacitance is generally larger in this geometry than in a cylindrical design, which increases electronic noise; and a relatively small portion of the total gas volume is active, whereas the cylindrical geometry can have an active gas volume of nearly 100%.

Thus, a desirable detector design would use the cylindrical geometry for improved electronic noise and detection efficiency, but an alternative coplanar anode design must be developed that does not rely upon the helical anode and its charge collection problems. An interesting model for this alternative design is the dual-anode cylindrical ionization chamber (DACIC) concept, also presented in Section 1.4.4, which features two symmetric anode wires stretched axially in a cylindrical HPXe ionization chamber [58, 62]. Due to the azimuthal weighting potential asymmetry arising from just two anode

wires coupled with the charge sharing problems stemming from both anodes being held at the same potential, the DACIC device is limited in spectroscopic performance.

Let us consider a geometry not unlike the DACIC device as the basis for the proposed coplanar anode HPXe design. Instead of just two thin wires, multiple anode wires will be used to improve the azimuthal weighting potential symmetry; to create the symmetry, the wires will be oriented axially along the surface of an imaginary cylinder with equal spacing between wires. The wires will be of relatively large diameter, making them less sensitive to microphonic vibration. Finally, the wires will be connected into two independent anodes and held at different operating biases, thus defining collecting and noncollecting anodes, and signal subtraction will be employed for proper coplanar operation.

The existing HPXe cylindrical chambers with the helical anodes will be retrofitted with the new anode design: the pressure vessel dimensions are therefore constrained. The variable design parameters are the number of wires (although the number of anodes is always two, the number of wires per anode can be changed); the diameter of the individual wires; and the radius at which the wires are centered with respect to the detection volume's central axis.

The dimensions of the pressure vessel and all internal components are considered invariant in this analysis, since they have been defined by earlier designs. The pressure vessel and its inserts have an outer diameter of 4.25 inches (108 mm), and a total wall thickness of 0.125 inch (3.18 mm). This means the cathode radius is set at 2 inches (50.8 mm). The pressure vessel is 8 inches long (203.2 mm); the length of the detection volume is 4 inches (101.6 mm). For design purposes, a density of 0.5 g/cm^3 was assumed, as this is the gas density used in previous detectors. The dielectric constant of this gas is approximated as $\varepsilon_r = 1.12$ [80], and the conductivity by $\sigma = 0$.

The three design parameters that can be varied in this analysis are the thickness of the anode wires, their location relative to the center of the detector, and the total number of wires used. Let us first consider the wire diameter. Since the intent of this project is to remove susceptibility to microphonics, a sturdy wire is required; the tradeoff is that the detector capacitance (and thus the associated electronic noise) increases dramatically with increasing wire diameter. Although much analysis could be performed on the optimal

wire thickness, a wire diameter of 1 mm has been chosen without supporting analysis. However, at this point a proof-of-principle design is of interest to determine whether the anode configuration has potential to perform competitively as a spectrometer. Should this be the case, further analysis can be performed to truly optimize the chamber's coupled spectroscopic and vibration properties. Similarly, the wire offset from the detector's central axis is also a free parameter, but in this design it is held constant at 12.7 mm. This offset is used because it is known from helical-anode detector experiments to provide an acceptable electric field throughout the detector's sensitive volume.

Table 3.1. A summary of fixed design parameters.

Parameter	*Design Value*
Detection volume length	101.6 mm
Cathode diameter	101.6 mm
Anode displacement from central axis	12.7 mm
Anode wire diameter	1 mm
Xenon gas density	0.5 g/cm^3

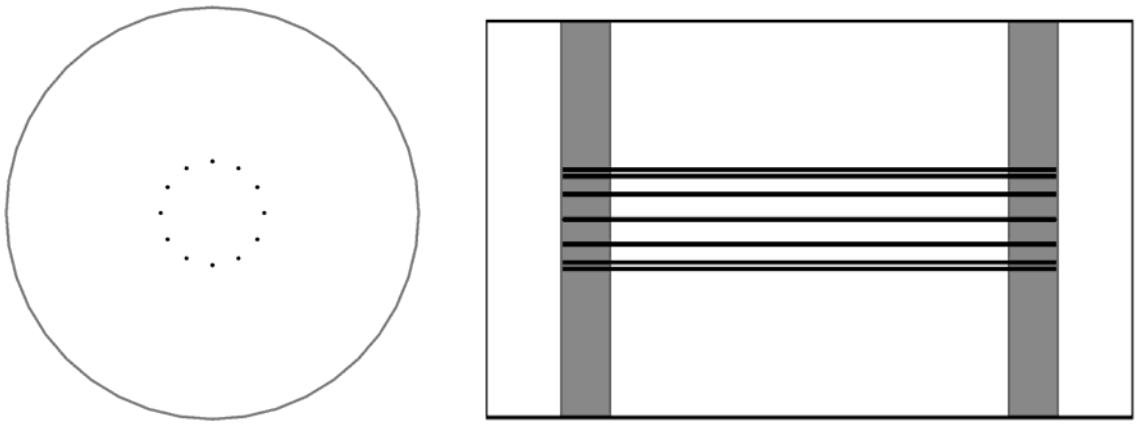

Figure 3.1. Cross-sectional schematics of the proposed detector showing end (left) and side (right) views. Anode wires are black, Macor insulators are gray, and white areas designate the gas volumes.

The anode wires are centered at a radius of 12.7 mm relative to the central axis of the chamber. The wires are spaced at regular intervals along the surface of the imaginary cylinder defined by this radius: for example, a design utilizing 8 wires has a separation of 45° between adjacent wires. The active wire length is 101.6 mm, which is defined by the pressure vessel and its internal components; however, the true wire length necessary for capacitance calculations is probably closer to 140 mm, as the wires pass through holes drilled in 12.7 mm-thick Macor insulating plates on either end of the detection volume. Table 3.1 summarizes the important design parameters. Figure 3.1 shows schematics of the proposed design for a 12-wire anode geometry.

3.2 Electrostatic Potential Theory

It is desirable to determine the operating potential throughout the detector as a function of the applied electrode biases, as well as the weighting potential distribution in the detector. This information can be very useful in designing, operating, and understanding the detector. For example, the weighting potential allows one to determine how much charge will be induced on the anodes for each event, which can be used to calculate expected pulse-height spectra, thus permitting analysis of different detector configurations. The operating potential, once determined, can be used to determine how the charges formed in an event actually move through the chamber, what biases need to be applied to create an electric field sufficient to collect all charges, and what the charge collection time is.

3.2.1 General Potential Theory

Let us first attempt to derive the solution for generic boundary conditions, which can be replaced later with actual values for determining the weighting potential or operating potential distributions. To solve for the general potential as a function of position inside the detector, $\varphi(r,\theta,z)$, one solves Poisson's equation (3.1):

$$\nabla^2\varphi = -\frac{\rho(r,\theta,z)}{\varepsilon} \tag{3.1}$$

In this equation cylindrical coordinates are being used, so r refers to the radius, θ the azimuthal angle, and z the axial position. The geometry is defined such that one of the collecting anode wires is centered at $\theta = 0$ and the origin of the coordinate system lies on the central axis of the detector, with the exact center of the detector corresponding to the plane $z = 0$. The symbol ε is the permittivity of the xenon gas, and ρ the distributed space charge.

There are three boundary conditions in this system, corresponding to the potentials applied at the cathode surface, φ_{cat}; the collecting anode wires, φ_{CA}; and the noncollecting anode wires, φ_{NCA}. Let the solution process begins with the following assumptions:

1. axial variations in $\varphi(r,\theta,z)$ are negligible,
2. the solution to the differential equation is separable in the radial and azimuthal coordinates $\rightarrow \varphi(r,\theta) = R(r)\cdot\Theta(\theta)$,
3. the space charge is negligible at all locations $\rightarrow \rho = 0$, and
4. the anode wires are two dimensional, having zero thickness in the radial direction.

Assumption (4) is necessary due to a limitation in the separation of variables method which requires all boundaries of the solution region to be coordinate surfaces, where one variable remains constant [81]. Using the aforementioned assumptions, the governing differential equation (3.1) can now be transformed from

$$\frac{1}{r}\frac{\partial}{\partial r}\left(r\frac{\partial\varphi}{\partial r}\right)+\frac{1}{r^2}\frac{\partial^2\varphi}{\partial\theta^2}+\underbrace{\frac{\partial^2\varphi}{\partial z^2}}_{=0}=-\underbrace{\frac{\rho(r,\theta,z)}{\varepsilon}}_{=0}$$

to

$$\underbrace{\frac{r}{R}\frac{d}{dr}\left(r\frac{dR}{dr}\right)}_{+\lambda}+\underbrace{\frac{1}{\Theta}\frac{d^2\Theta}{d\theta^2}}_{-\lambda}=0\ , \qquad (3.2)$$

where the parameter λ is the separation constant. The polarity of λ was chosen for convenience.

Let us first turn our attention to the differential equation describing solution behavior in the azimuthal direction,

$$\frac{d^2\Theta}{d\theta^2} + \lambda\Theta = 0 \tag{3.3}$$

To be rigorous, the separation constant cannot immediately be assumed positive; all possible values must be considered. It is fairly simple to show that when λ is negative only the trivial solution is possible. For this case, one arrives at the solution

$$\Theta(\theta) = c_1 e^{\sqrt{-\lambda}\,\theta} + c_2 e^{-\sqrt{-\lambda}\,\theta}$$

Since the solution must be periodic due to the symmetry within the detector, the only way to satisfy the regularity of the solution is for $c_1 = c_2 = 0$. Let us now examine the case $\lambda = 0$. Considering equation (3.3) again, the solution is

$$\Theta(\theta) = c_3 + c_4\theta$$

To satisfy the periodicity requirements, the constant c_4 must be zero. Finally, let us consider the solution of (3.3) when λ is positive. This solution can satisfy the periodicity requirements without forcing constants of integration to zero:

$$\Theta(\theta) = c_5 \cos\left(\sqrt{\lambda}\,\theta\right) + c_6 \sin\left(\sqrt{\lambda}\,\theta\right)$$

At this point the constant λ can be determined. The argument to the cosine and sine terms must be 2π-periodic when the angle separating two adjacent collecting anode

wires is entered. If there are a total of N_w wires (both collecting and noncollecting), then the corresponding angle is $4\pi/N_w$, and the eigenvalues λ are

$$\sqrt{\lambda} = n\frac{N_w}{2} \quad , \quad n = 0, 1, 2, \ldots \tag{3.4}$$

Now let us consider the differential equation describing the potential variations with radius,

$$\frac{r}{R}\frac{d}{dr}\left(r\frac{dR}{dr}\right) = \lambda \tag{3.5}$$

This equation should be solved for the cases in which nontrivial solutions to equation (3.3) were obtained, so that a general solution may be obtained for Poisson's equation. When $\lambda = 0$, the solution to equation (3.5) is easily verified to be

$$R(r) = c_7 \ln(r) + c_8 \ ;$$

in this result, both constants can be nonzero and still satisfy basic solution properties, so they must be determined when the boundary conditions are applied. For λ positive, the general solution to equation (3.5) is given by the dimensionless equation

$$R(r) = c_9\left(\frac{r}{R_{cat}}\right)^{+\sqrt{\lambda}} + c_{10}\left(\frac{r}{R_{cat}}\right)^{-\sqrt{\lambda}}$$

where R_{cat} denotes the cathode radius. The constants c_9 and c_{10} will not be determined until later, when the boundary conditions are applied to the overall solution.

Since the differential equation (3.2) is linear and homogeneous, the principle of superposition is used to combine the results developed for nontrivial cases. The general solution for the electrostatic potential is equation (3.6):

$$\varphi(r,\theta) = A_0 + B_0 \ln\left(\frac{r}{R_{cat}}\right) + \sum_{n=1}^{\infty}\left\{\begin{array}{l}\left[A_n\left(\frac{r}{R_{cat}}\right)^{+\sqrt{\lambda_n}} + B_n\left(\frac{r}{R_{cat}}\right)^{-\sqrt{\lambda_n}}\right]\cos\left(\sqrt{\lambda_n}\theta\right) \\ + \left[C_n\left(\frac{r}{R_{cat}}\right)^{+\sqrt{\lambda_n}} + D_n\left(\frac{r}{R_{cat}}\right)^{-\sqrt{\lambda_n}}\right]\sin\left(\sqrt{\lambda_n}\theta\right)\end{array}\right\} \quad (3.6)$$

Now the boundary conditions will be applied. First it is noted that, due to the symmetry of the geometry and the imposed boundary conditions, the electrostatic potential solution is a symmetric function with a period defined by the number of anode wires in the detector. Also, the coordinate system has been defined such that the potential solution is symmetric about $\theta = 0$, and is therefore an even function. It is a fact that if a function is even, then its Fourier series only contains cosine terms [82]. Thus in equation (3.6), $C_n = D_n = 0$ for all n. The complete solution is now

$$\varphi(r,\theta) = A_0 + B_0 \ln\left(\frac{r}{R_{cat}}\right) + \sum_{n=1}^{\infty}\left[A_n\left(\frac{r}{R_{cat}}\right)^{+\sqrt{\lambda_n}} + B_n\left(\frac{r}{R_{cat}}\right)^{-\sqrt{\lambda_n}}\right]\cos\left(\sqrt{\lambda_n}\theta\right) \quad (3.7)$$

At this point, it is necessary to treat the detector in two parts: the regions with radii (i) greater than and (ii) less than R_{an}, the radius of the imaginary cylinder on which the anode wires are placed. The requirement of two separate solution regions is apparent if one tries to use just one region for the entire detection volume. If first the boundary condition at the cathode surface is applied to equation (3.7) and then the solution is examined as $r \to 0$, the only finite solution is $\varphi(r,\theta) = \varphi_{cat}$, which is not true if the anodes are held at unique potentials.

For the outer region $R_{an} \le r \le R_{cat}$, one should first examine the boundary condition at the cathode surface. It is an easy matter to show that the only general solution to this boundary condition (i.e., for arbitrary values of θ) requires

1. $A_0^{out} = \varphi_{cat}$, and
2. $A_n^{out} + B_n^{out} = 0$.

For the region $0 \le r \le R_{an}$, one applies the appropriate boundary condition at the center of the detector in lieu of that at the cathode surface. This boundary condition places the constraint $B_0^{in} = B_n^{in} = 0$ in equation (3.7); otherwise the corresponding terms would be unbounded near the detector's center, which is unphysical. The general equations describing the potential in the inner and outer regions are

$$\begin{aligned} \varphi^{in}(r,\theta) &= A_0^{in} + \sum_{n=1}^{\infty} A_n^{in} \left(\frac{r}{R_{cat}} \right)^{+\sqrt{\lambda_n}} \cos\left(\sqrt{\lambda_n}\theta \right) \\ \varphi^{out}(r,\theta) &= \varphi_{cat} + B_0^{out} \ln\left(\frac{r}{R_{cat}} \right) + \sum_{n=1}^{\infty} A_n^{out} \left[\left(\frac{r}{R_{cat}} \right)^{+\sqrt{\lambda_n}} - \left(\frac{r}{R_{cat}} \right)^{-\sqrt{\lambda_n}} \right] \cos\left(\sqrt{\lambda_n}\theta \right) \end{aligned} \tag{3.8}$$

The inner and outer solution regions meet at an interface located at $r = R_{an}$. The boundary condition at this interface is now considered, as it will allow us to determine A_0^{in}, A_n^{in}, A_n^{out}, and B_0^{out} explicitly. Since the distribution of the potential along this imaginary surface is unknown at this time, let us generally refer to the interface potential as $\varphi_{\text{int}}(\theta)$. The coefficients A_n and B_0 are determined via the Euler formula [83], which invokes orthogonality arguments to pick out one coefficient at a time:

$$A_0^{in} = \frac{N_w}{4\pi} \int_{-2\pi/N_w}^{2\pi/N_w} \varphi_{\text{int}}(\theta)\, d\theta$$

$$A_n^{in} = \frac{N_w}{2\pi} \left(\frac{R_{cat}}{R_{an}} \right)^{\sqrt{\lambda}} \int_{-2\pi/N_w}^{2\pi/N_w} \varphi_{\text{int}}(\theta) \cos\left(\sqrt{\lambda_n}\theta \right) d\theta$$

$$A_n^{out} = \frac{N_w}{2\pi \left[\left(\frac{R_{an}}{R_{cat}} \right)^{\sqrt{\lambda}} - \left(\frac{R_{an}}{R_{cat}} \right)^{-\sqrt{\lambda}} \right]} \int_{-2\pi/N_w}^{2\pi/N_w} \varphi_{\text{int}}(\theta) \cos\left(\sqrt{\lambda_n}\theta \right) d\theta \tag{3.9}$$

$$B_0^{out} = \frac{N_w}{4\pi \ln\left(\frac{R_{an}}{R_{cat}} \right)} \left(\int_{-2\pi/N_w}^{2\pi/N_w} \varphi_{\text{int}}(\theta)\, d\theta - \frac{4\pi}{N_w} \varphi_{cat} \right)$$

It is evident that the functional form of $\varphi_{\text{int}}(\theta)$ is necessary to solve the Euler formula. This is not known *a priori*, as the anode wires occupy only a fraction of the circumference of the cylinder defined by R_{an}. At this point, it is necessary to use numerical methods to determine the Fourier constants. Let us proceed with the information in hand for further analysis.

3.2.2 Weighting Potential Representation

The weighting potential in cylindrical coplanar-anode radiation detectors was investigated previously by He and Khachaturian [84]; the theoretical framework used by those authors is implemented in this chapter. The technique of coplanar anodes requires the subtraction of induced signals; the Shockley-Ramo theorem [72] can be used to show that the difference between the collecting anode's weighting potential at the point of charge carrier creation and that of the noncollecting anode is a parameter of interest for optimizing signal amplitude uniformity. Let us return to equation (2.8), assigning collecting anode (CA) status to electrode 2 and making electrode 3 the noncollecting anode (NCA), and assume all electrons are ideally collected at the collecting anode:

$$
\begin{aligned}
\Delta Q_{diff} &= \Delta Q_{CA} - \Delta Q_{NCA} \\
&= -e\sum_{j=1}^{N}\left(\varphi_{CA,f}^{j} - \varphi_{CA,i}^{j}\right) + e\sum_{i=1}^{N}\left(\varphi_{NCA,f}^{j} - \varphi_{NCA,i}^{j}\right) \\
&= -e\sum_{j=1}^{N}\left[\left(\underbrace{\varphi_{CA,f}^{j}}_{1} - \underbrace{\varphi_{NCA,f}^{j}}_{0}\right) - \underbrace{\left(\varphi_{CA,i}^{j} - \varphi_{NCA,i}^{j}\right)}_{\varphi_{diff,i}^{j}}\right] \\
&= -e\sum_{j=1}^{N}\left(1 - \varphi_{diff,i}^{j}\right)
\end{aligned}
\tag{3.10}
$$

In this case, the final measured signal is a summation over all N electrons of the anode weighting potential difference at the point of charge creation, $\varphi_{diff,i}^{j}$. Ideally $\varphi_{diff,i}^{j}$ is zero everywhere, which makes the measured signal amplitude a function of only the number of electrons created in the radiation interaction.

Since Laplace's equation (3.1) is linear and homogeneous, it is trivial to show that because the weighting potential distributions of both the collecting and noncollecting anodes obey Laplace's equation, then the difference of the two will obey the same equation:

$$\nabla^2\varphi_{CA} = \nabla^2\varphi_{NCA} = 0 \tag{3.11}$$

$$\nabla^2\varphi_{CA} - \nabla^2\varphi_{NCA} = \nabla^2\left(\varphi_{CA} - \varphi_{NCA}\right) = \nabla^2\varphi_{diff} = 0 \tag{3.12}$$

Table 3.2. Boundary conditions for the various weighting potentials.

Conducting Surface	φ_{CA} *Value*	φ_{NCA} *Value*	φ_{diff} *Value*
Cathode	0	0	0
Collecting Anode	1	0	1
Noncollecting Anode	0	1	-1

Now that the differential equation is being solved directly for the weighting potential difference, a consideration of boundary conditions is necessary. Table 3.2 gives

the boundary conditions for the collecting and noncollecting anode weighting potentials; subtraction yields the boundary conditions for the weighting potential difference φ_{diff} .

3.3 Chamber Optimization

To optimize the number of wires in the anode structure, let us assume that the detector is biased optimally such that all electrons created in an interaction drift to the collecting anode. In this idealized case, the uniformity of the anode weighting potential difference φ_{diff} will be of utmost importance. Let us now return to the problem of approximating the weighting potential via a Fourier series. Electronic noise contributions will be considered later, and the optimal combination of charge induction and electronic noise will determine the optimal geometry.

It is worth stating at this point that in the following sections functional approximations are made to simulated data without rigorous error analysis. This is not expected to have a significant impact upon the optimization study, as the modeling employs many idealizations that are expected to introduce significant uncertainly.

3.3.1 Numerically Determining the Weighting Potential Fourier Coefficients

There are three difficulties in solving equations (3.9) for the Fourier coefficients: the function $\varphi_{\text{int}}(\theta)$ is not known *a priori*; except for a few special cases of $\varphi_{\text{int}}(\theta)$, the integrals cannot be solved without the help of mathematical software; and finally, there are an infinite number of terms in the Fourier series. Fortunately, these complications can be overcome using the Maxwell 3D [85] and Mathematica [86] software packages.

Maxwell 3D is a finite-element software package for solving electrostatic problems. By creating the geometry as accurately as possible and using the proper material properties, the potential distribution can be calculated throughout the geometry. This allows the estimation of $\varphi_{\text{int}}(\theta)$ by plotting the numerical solution along the arc $r = R_{an}$. Mathematica can be used for solving the difficult integrals in (3.9) and for determining how many terms in the Fourier series are needed for a close approximation of the true solution.

Let us investigate the convergence and accuracy of coupling equations (3.8) and (3.9) with numerical simulations modeling the proposed geometry: anode wires of radius $R_w = 0.5\,\text{mm}$ centered at radius $R_{an} = 12.7\,\text{mm}$ relative to the central axis of the chamber, and cathode radius $R_{cat} = 50.8\,\text{mm}$. Consider three different cases: 2, 4, and 12 anode wires. To determine the Fourier coefficients, approximate $\varphi_{\text{int}}^{diff}(\theta)$ with the piecewise-continuous function

$$\varphi_{\text{int}}^{diff}(R_{an},\theta) = \begin{cases} -1 & ; \quad \theta \in \left(-\dfrac{2\pi}{N_w}, -\dfrac{2\pi}{N_w} + \theta_0\right) \\ \alpha \cot\left(-\dfrac{N_w}{2}\theta\right) & ; \quad \theta \in \left(-\dfrac{2\pi}{N_w} + \theta_0, -\theta_0\right) \\ +1 & ; \quad \theta \in \left(-\theta_0, +\theta_0\right) \\ \alpha \cot\left(+\dfrac{N_w}{2}\theta\right) & ; \quad \theta \in \left(+\theta_0, \dfrac{2\pi}{N_w} - \theta_0\right) \\ -1 & ; \quad \theta \in \left(\dfrac{2\pi}{N_w} - \theta_0, \dfrac{2\pi}{N_w}\right) \end{cases} \tag{3.13}$$

In (3.13), the symbol θ_0 is a configuration-dependent constant that represents the angle at which the cotangent term value equals one:

$$\theta_0 = \frac{2}{N_w}\tan^{-1}(\alpha)$$

Figure 3.2 plots simulation data from the Maxwell 3D code against distributions calculated with equation (3.13) for a fixed radius of 12.7 mm, which is the location of the interface between the inner and outer solution regions. The differences between the simulation data and the approximating function are large only in small regions near the edge of the anode wires, and seem to decrease as the number of anode wires increases.

The coefficient α used to calculate the weighting potentials estimated by equation (3.13) was adjusted to the best fit by eye, and is listed for each case in Table 3.3.

Table 3.3. Values of α used to calculate the weighting potential difference in Figure 3.2.

Number of Anode Wires	α
2	0.20
4	0.25
12	0.45

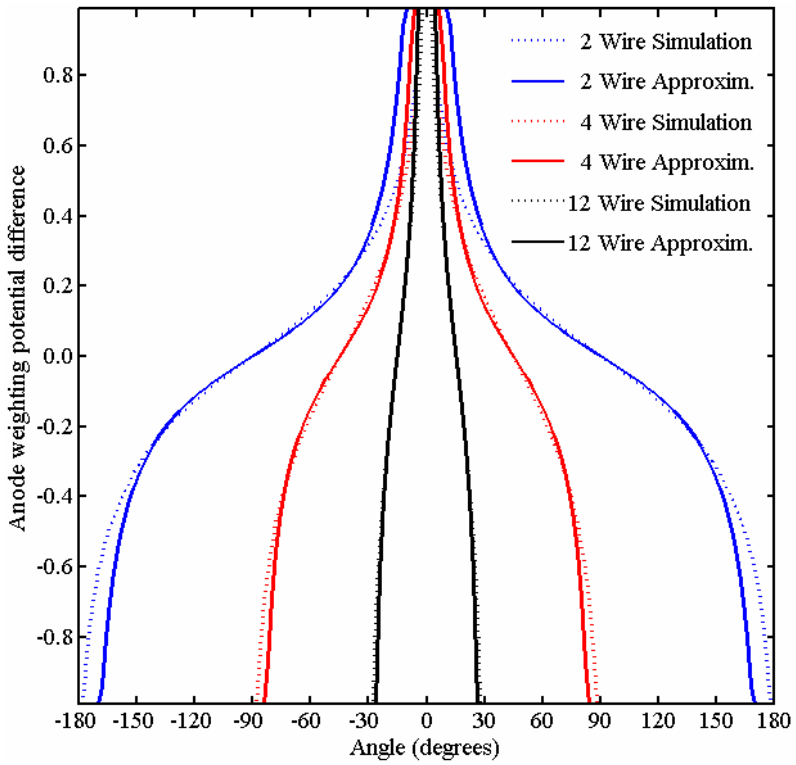

Figure 3.2. Comparison of one period of the simulated weighting potential difference and the approximation along the solution interface for 2, 4, and 12 anode wires.

Now that an approximation for the interface weighting potential difference $\varphi_{\text{int}}^{diff}$ has been established, let us focus on calculating the Fourier series in (3.8). Terms where the summation index n is even have Fourier coefficients of zero, since these indices

result in cosine terms with local maxima at locations where the true function being approximated is zero. Thus, to compute only the nonzero Fourier series terms, a simple modification of λ_n in equations (3.8) can be performed:

$$\sqrt{\lambda_n} = n\frac{N_w}{2}, \quad n = 0, 1, 2\ldots \quad \rightarrow \quad \sqrt{\lambda_n} = (2n+1)\frac{N_w}{2}, \quad n = 0, 1, 2\ldots$$

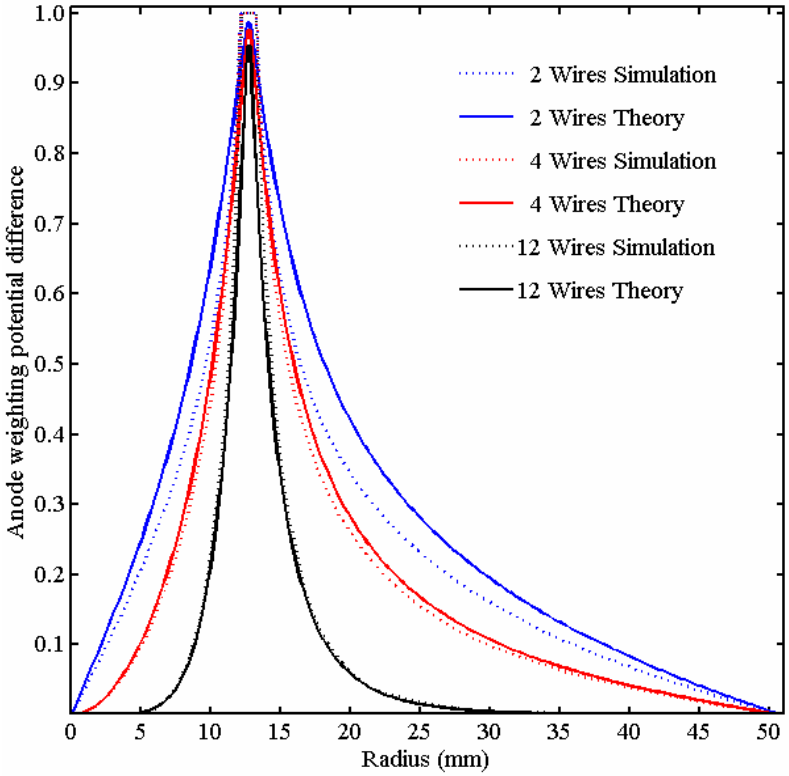

Figure 3.3. Comparison of the Maxwell 3D simulated anode weighting potential difference and the first 25 terms of the Fourier series for 2, 4, and 12 wires.

Now it is appropriate to examine the weighting potential difference calculated with equations (3.8) and compare them to the Maxwell 3D simulation results. Figure 3.3 is a comparison of the first 25 nonzero terms of each Fourier series to the Maxwell-simulated weighting potential difference. The abscissa represents the radial coordinate for each data point; the data presented is along the plane $\theta = 0$, directly through the center of a collecting anode wire. The overestimation of the subtracted weighting potential in the vicinity of the anode wires is likely due to the imperfect fit of the

assumed boundary-condition profiles in Figure 3.2, although the treatment of the wires as 2-dimensional surfaces should also contribute to the deviation. Notice in Figure 3.2 that the distribution of $\varphi_{\text{int}}^{diff}$ calculated for 2 anode wires is not as accurate as that for 12 wires, thus translating into a poorer estimation of the weighting potential in Figure 3.3.

The results are satisfactory when there are more than 2 anode wires, especially when considering that interactions will occur more frequently near the cathode due to the cylindrical geometry, and the equations are quite accurate in this region. Also, the weighting potential distribution for fixed radius is maximized at $\theta = 0$; as the azimuthal angle is shifted toward an adjacent noncollecting anode wire, the difference between the estimated and true weighting potential will generally improve.

It is important to investigate whether summing over 25 Fourier cosine terms will indeed result in a converged answer. To examine this assumption, Figure 3.4 shows the convergence of the solutions when the first 1, 5, 10, and 25 nonzero terms are included. From the figures, it appears that approximately 10 terms is sufficient for a converged solution.

It has now been shown that 10-term expansions of equations (3.8) and (3.9) provide an acceptable approximation to the true distribution along one particular radial segment. The next step is to investigate whether these equations correctly model the behavior with changing azimuthal angle. To test this, Maxwell 3D-simulated data at a fixed radius of 20 mm has been generated over an entire angular period (e.g., from the center of one noncollecting anode to the center of the next noncollecting anode). A radius of 20 mm has been chosen because the weighting potential slowly becomes more sinusoidal in shape as the radius increases, so near the cathode a very smooth cosine shape should exist, which is not a challenging test scenario. Near the anode, though, some non-sinusoidal behavior can be observed due to the proximity of the anode wires, and this is expected to be more difficult to model.

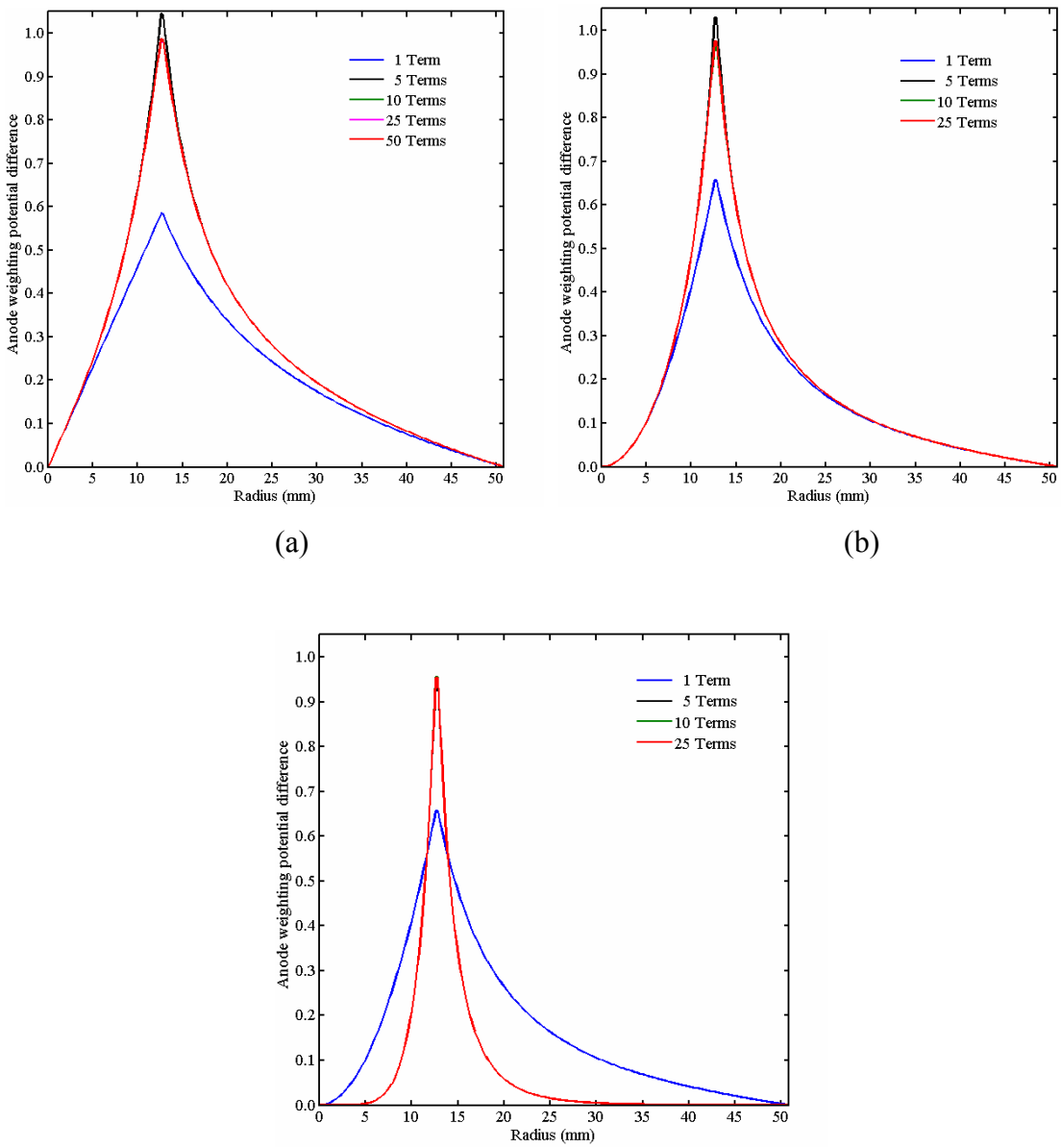

Figure 3.4. Demonstrating the convergence of the Fourier series for (a) 2 anode wires, (b) 4 wires, and (c) 12 wires. The 10 term expansion cannot be seen as it lies directly underneath the 25 term expansion.

A comparison between these simulations and the results from equation (3.8) can be found in Figure 3.5 below. In this figure, the series expansion is scaled by a factor corresponding to the difference in theory and simulation demonstrated in Figure 3.3. The predicted solution behavior is in acceptable agreement with the true distribution. In fact, the differences are only noticeable for 2 anode wires, and this is again because of the

poor approximation of boundary conditions at the anode radius (see Figure 3.2). Figure 3.5 also demonstrates convergence of the Fourier approximation as the number of summed series terms is varied again from 1 to 25 terms. Series convergence is acceptable with very few terms, as changes cannot be noticed beyond 5 terms at this particular radius. Only the convergence of the 2-wire simulation is shown, since convergence is even more rapid when the number of anode wires is increased.

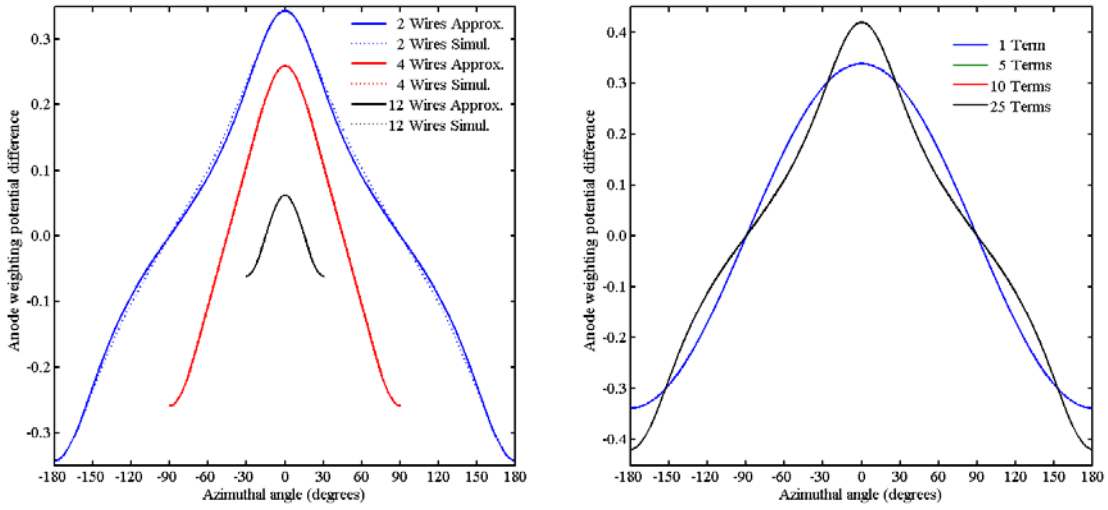

(a) (b)

Figure 3.5. (a) Comparing the simulated and calculated $\varphi_{diff}(20\,\text{mm},\theta)$. The calculated distribution is scaled by the amplitude difference found in Figure 3.3 to isolate the azimuthal changes. (b) Convergence of the Fourier series expansion for 2 anode wires.

It is appropriate at this point to test the validity of the first assumption made for the mathematical treatment of the general potential solution, that the anode wires are sufficiently long to neglect axial variations in the potential. This investigation can easily be made by examining the Maxwell 3D results for various geometries along lines of constant radius and azimuth. The first plot, Figure 3.6, shows the simulated anode weighting potential difference along the fixed line $(r,\theta)=(20\,\text{mm},0)$; the number of simulated anode wires is varied from 2 to 16. This fixed line lies in the plane intersecting a collecting anode and the central axis of the detector, and the line is not far away from the anode wire. In this coordinate system the origin lies at the geometrical center of the detector, so the plot shows the variations from the detector midpoint out to the end of the

cylindrical volume; due to symmetry, the entire length need not be considered. The anode weighting potential difference is very uniform as a function of axial position throughout the detection volume, $0 \le z \le 50.8$ mm, especially when there are at least 4 anode wires.

It is possible that this uniformity is misleading due to the location's proximity to an anode, which fixes the weighting potential to a uniform value of unity at the wire. Therefore, Figure 3.7 shows a similar plot when the number of anode wires is fixed at 8, the azimuthal angle at 10º, and the radius is varied. Again, the uniformity throughout the detection volume is fairly good. Thus, it seems that the assumption of axial uniformity is reasonable.

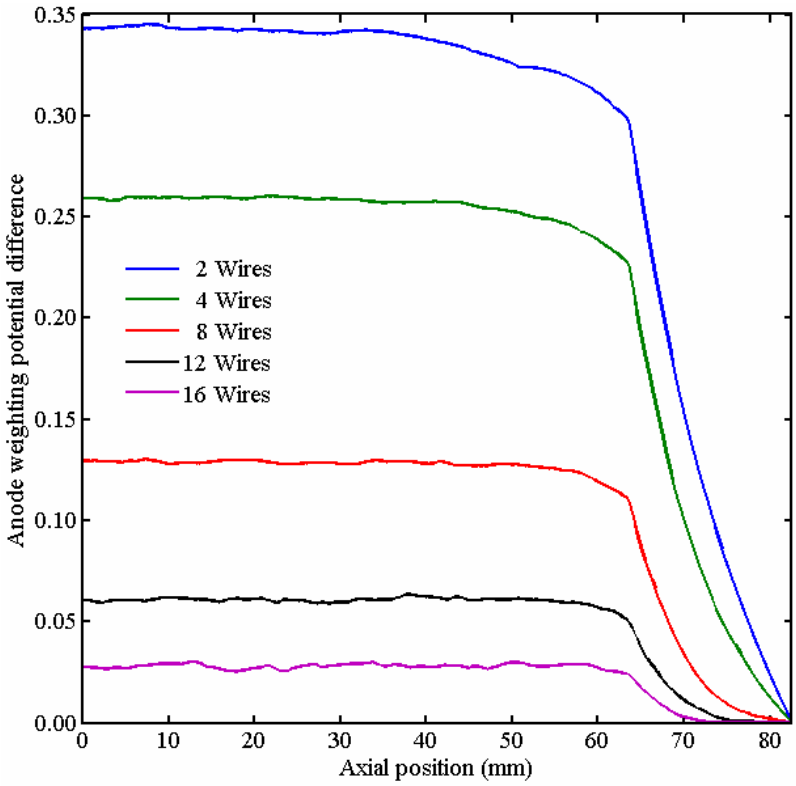

Figure 3.6. Axial variations in the anode weighting potential difference for 2 to 16 anode wires along the line $(r, \theta) = (20 \text{ mm}, 0)$.

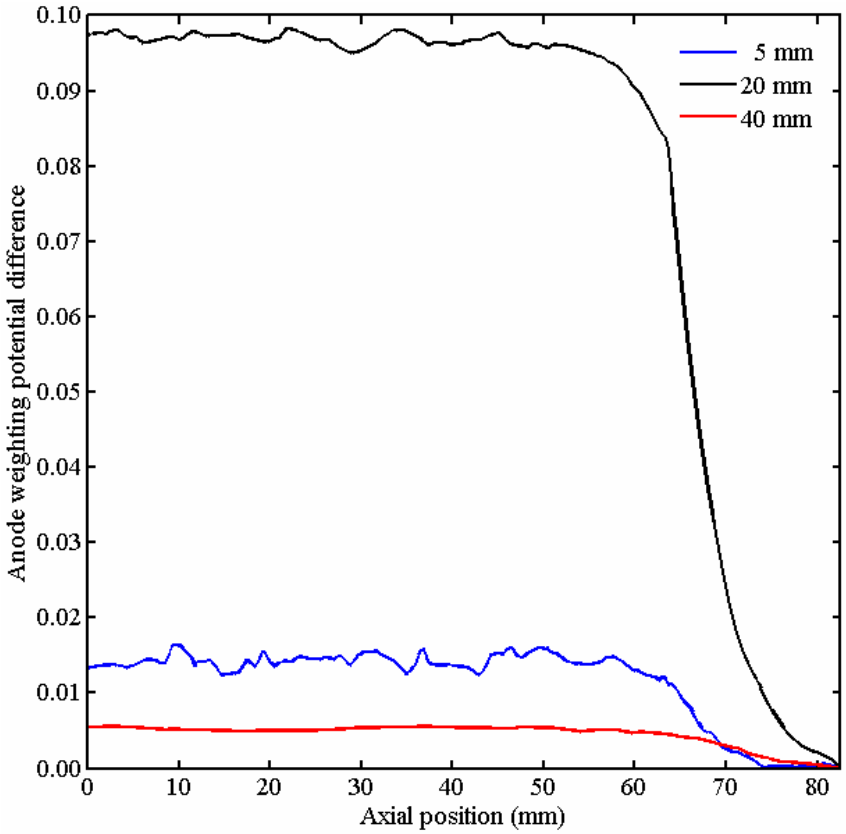

Figure 3.7. Axial variations in the anode weighting potential difference for 8 anode wires along lines with $\theta = 10°$.

3.3.2 Charge Induction Uniformity Dependence Upon the Number of Wires

Now that both an acceptable mathematical formulation and the more accurate numerical simulations of the weighting potential inside the proposed chamber have been developed, the next step in detector optimization is to study the effect of the number of anode wires on the uniformity of charge induction throughout the entire working volume. Referring to equation (3.10), it is apparent that for optimal charge induction in which $\Delta Q_{diff} = Ne$ for interactions at any point in the detection volume, it is necessary for the anode weighting potential difference to satisfy $\varphi_{diff} = 0$ everywhere in the xenon gas.

At this point, let us use the Maxwell 3D electrostatic solver for the analysis due to its improved accuracy. Using equation (3.12) and the boundary conditions supplied in Table 3.2 it is possible to solve for the anode weighting potential difference directly. The

simulations use the geometry and materials described in Section 3.1 with the number of anode wires varying from 2 to 16. Cylinders created in Maxwell 3D are approximated by a user-defined number of rectangular segments; it was found via trial and error that 40 segments is a sufficient number. The results of these simulations along a line intersecting a collecting anode wire on the plane $z = 0$ are shown in Figure 3.8. This particular line was chosen because φ_{diff} will be least ideal in the proximity of an anode wire, so the plot shows the worst case (near the noncollecting anode φ_{diff} has the same magnitude but opposite sign).

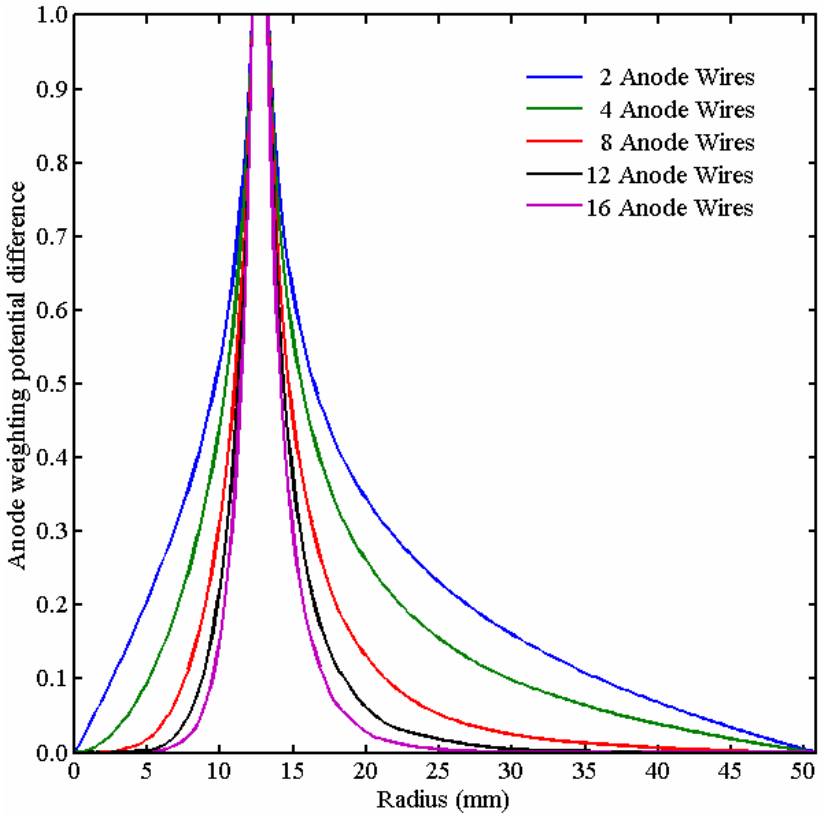

Figure 3.8. The dependence of $\varphi_{diff}\left(r, \theta = 0, z = 0\right)$ on the number of anode wires.

From a single-polarity charge sensing standpoint, it is obvious that increasing the number of wires results in more ideal charge induction. At some point adding more wires will have severely diminished returns, since the improvements in charge induction will occur mainly for interactions in a vanishingly small volume near the anode wires. There

are two practical limitations on the number of wires, one of which is that at some point it will become difficult to construct the detector in such a way that it does not arc when the electrodes are biased. The other limit is reached sooner, and it is related to electronic noise.

3.3.3 Electronic Noise as a Function of the Number of Anode Wires

It has now been established that charge induction uniformity favors an anode structure with more wires. Let us consider the effect of wire number on electronic noise. The preamplifiers that will be used in experiments will be Amptek A250s with 2SK152 JFETs; Figure 3.9, reprinted from the A250 data sheet, provides an estimation of electronic noise as a function of detector capacitance for a shaping time of 2 μs, shown as data series 4 (in blue) [87]. A 2 μs shaping time is likely shorter than what will be used in the experiments due to the slow drift of electrons through HPXe chambers, but since this is the only data available giving electronic noise as a function of detector capacitance, let us use it anyway. To quantify the electronic noise, it is necessary to first calculate the detector capacitance, C_d, which can easily be computed using Maxwell 3D simulations.

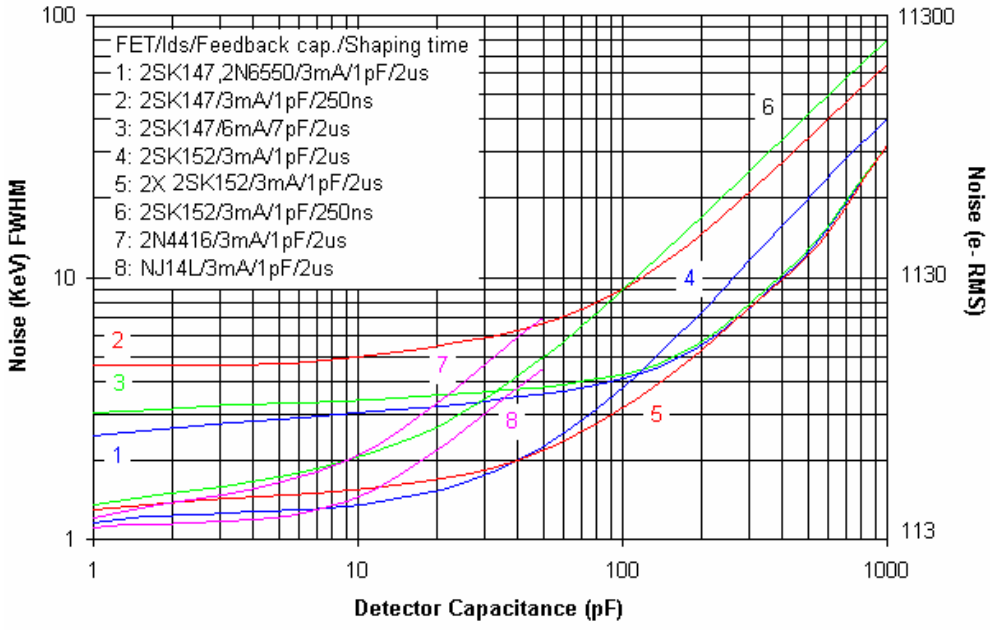

Figure 3.9. The expected A250 noise as a function of detector capacitance and FET.

To determine the detector capacitance, first note the relationships between the charge on an electrode q_c, the capacitance C_d between the signal electrode and its neighboring conductors, the potential difference $\Delta\varphi$ between conducting surfaces, and the displacement field $\boldsymbol{D}$ in the bulk medium:

$$q_c = C_d \Delta\varphi \tag{3.14}$$

$$q_c = \oint_S \boldsymbol{D} \cdot d\boldsymbol{a} \tag{3.15}$$

S is the surface of the signal electrode; in the case of the collecting or noncollecting anode, this is the total surface of all wires comprising the electrode.

Let us set the potential on the signal electrode to $\varphi = 1$, and let $\varphi = 0$ on all other conducting surfaces. Now $\Delta\varphi = 1$ and simple algebra leads to expression (3.16) for the capacitance, which is a formula that can be calculated directly in Maxwell 3D:

$$C_d = \oint_S \boldsymbol{D} \cdot d\boldsymbol{a} \tag{3.16}$$

Using the geometries previously created in Maxwell 3D for weighting potential calculations, the detector capacitance was calculated for anode structures up to 16 wires. Combining this information with the data presented in Figure 3.9, the preamplifier noise can be estimated using the concept of equivalent noise charge (ENC). The ENC is the amount of charge that, if suddenly placed on the signal electrode, would create an output signal equal in magnitude to the standard deviation of the peak broadening caused purely by electronic noise; ENC is often presented in units of electrons [8]. The ENC can be converted to FWHM with knowledge of w, the mean energy to create an ionization. The symbol e^- denotes an electron.

$$FWHM\left(\text{eV}\right) = 2.35 \cdot ENC\left(e^-\right) \cdot w\left(\text{eV}/e^-\right) \tag{3.17}$$

The results obtained using equations (3.16), (3.17), and Figure 3.9 are presented in Table 3.4. The mean energy to create an ionization used is $w = 21.9\,\text{eV}$ [8].

Table 3.4. Amptek A250 electronic noise contribution as a function of anode geometry.

Number of Wires	C_d *, pF*	*ENC, electrons*	*FWHM, keV*
4	3.09	141	7.26
8	6.64	146	7.52
10	8.34	151	7.78
12	10.78	156	8.03
14	13.08	161	8.29
16	16.10	166	8.55

The electronic noise from the preamplifier favors fewer wires in the anode geometry; however, the weighting potential data becomes more ideal when the number of anode wires is increased. Thus a final decision on the optimal geometry is best determined by performing simulations including both effects, which can combine them into one response function. Because the calculated width due to electronic noise broadening changes very little from one case to the next, it is expected that the optimal geometry will have a relatively large number of wires, since weighting potential improvements are fairly significant at low anode wire numbers.

3.3.4 The Optimal Balance of Electronic Noise and Weighting Potential

Geant4 simulations are used to determine the optimal number of anode wires. Geant4 [88], distributed by the CERN laboratory, is a Monte Carlo code that tracks the history initiated by each incident particle; one of the attractive attributes of Geant4 for this application is that tallies are easily constructed by the user to give nearly any information desired over a simulation run, whereas other widely-used codes such as MCNP5, distributed by Los Alamos National Laboratory, are very limited in output. In addition, it is relatively easy to insert code that performs certain calculations at each interaction location using the simulation data; this allows one to easily implement important concepts such as weighting potential and Fano statistics. The code requires the

incident radiation source to be defined, as well as the geometry, materials, physical processes of interest, and output tallies.

The simulations to select the optimal anode structure include the effects of Fano statistics, anode weighting potential difference, and preamplifier electronic noise. The anode weighting potential difference distribution used is the 10-term Fourier series approximation represented by equations (3.8), (3.9), and (3.13); it accounts for radial and azimuthal variations in the measured signal amplitude. The electronic noise is sampled from a normal distribution characterized by the ENC values of Table 3.4. To determine the total electronic noise for the system, the ENC for one A250 is multiplied by $\sqrt{2}$ to simplistically account for the use of two preamplifiers in the experiments. The Fano statistics sample from a normal distribution characterized by mean value E_{dep}/w and standard deviation $\sqrt{F\,E_{dep}/w}$, where E_{dep} and F are the energy deposited in an interaction and the Fano factor, respectively.

Assumptions made for these Geant4 simulations are:

1. axial effects are negligible;
2. it is sufficient to track only energy transfers from the primary gamma ray;
3. the charge cloud created in an interaction is negligibly small;
4. the detector is biased sufficiently to collect all electrons at the collecting anode;
5. positive ions remain motionless for the duration of signal formation;
6. ballistic deficit is negligible even for a 2 μs shaping time;
7. there is no charge recombination;
8. there is no charge diffusion; and
9. the Fourier series approximations introduce negligible error.

Of these assumptions, numbers 1, 3, 4, 5, 7, and 8 are not expected to cause significant deviations from the experiment. Assumption 2 is expected to enhance the photopeak somewhat due to the inclusion of energy carried out of the sensitive volume by x-rays or electrons diffusing into the wall, energy which in reality should be excluded from calculations. This assumption will also result in the omission of x-ray and escape peaks from the simulated spectra, which is acceptable for this particular study. Assumption 6

really is two separate suppositions: that a shaping time of 2 μs is acceptable experimentally, and that no amplitude deficit will be measured for any event. Assumptions 6 and 9 are the most questionable, but will be analyzed in Chapter 6 for validity.

Simulated spectra are generated for a source of ^{137}Cs gamma rays flooding one end of the pressure vessel. The modeled detector geometry includes all steel, Macor insulator, and HPXe spaces; minor volumes such as the anode wires and connectors are not modeled. Since the only physical processes that contribute to the energy spectra in these simulations are Compton scattering and photoelectric absorption of the initial gamma rays, spectral features such as x-ray escape peaks are absent. Figure 3.10 shows the spectral variations as a function of the number of anode wires, along with a close-up of the photopeak region.

The result of this analysis is that 12 anode wires (2 groups of 6 wires each) is expected to be the optimal configuration for best energy resolution: fewer wires will broaden the photopeak due to larger deviations of the weighting potential from the ideal distribution, while using more than 12 wires degrades resolution from the associated increase in electronic noise. The predicted energy resolution of 2.3% FWHM at 662 keV is quite good; it is not only better than other HPXe detectors of similar dimension, but is comparable to small-diameter chambers. The spectral feature around 200 keV is the traditional backscatter peak, which comes from the inclusion of the steel pressure vessel and the Macor shell in the Geant4 simulation geometry. There are a significant number of counts between the Compton edge and the photopeak; these are due to multiple Compton scatters in the working gas. The presence of counts at energies greater than the gamma ray's actual energy, also noted in [89], is an artifact of the signal subtraction step. Essentially it is possible for gamma-ray interactions to occur in locations where the net induced charge on the collecting anode is close to the charge generated in the interaction, while the noncollecting anode's induced charge is negative. The subtraction step yields a net signal appearing to be greater than the gamma ray's actual energy, producing a continuum that extends up to double the gamma ray's energy. If Figure 3.8 had shown φ_{diff} for azimuthal angles near a noncollecting anode wire, negative values of φ_{diff} would

be shown. Inserting these values into equation (3.10) gives artificially-high energy measurements.

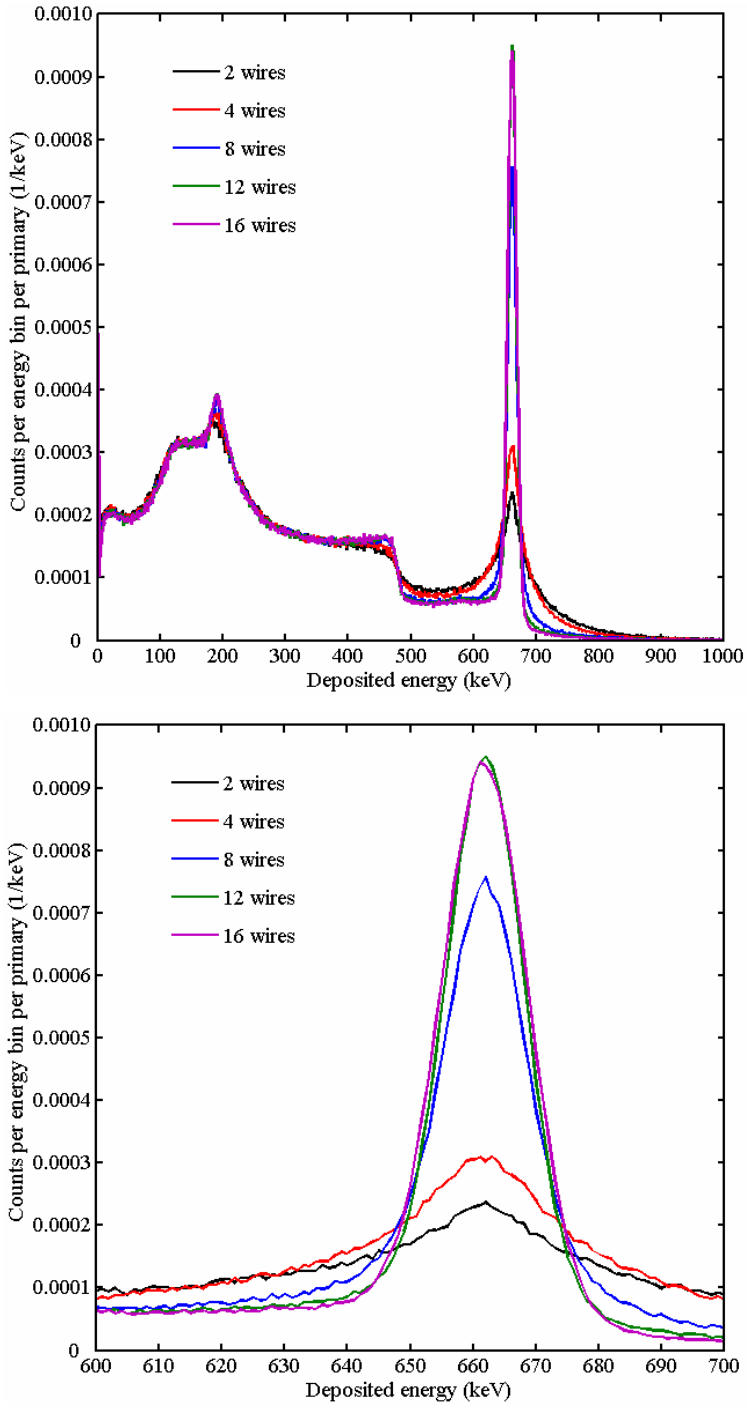

Figure 3.10. Simulated ^{137}Cs energy spectra for different anode wire numbers (top). Zooming in on the peak region shows 12 wires to give the best resolution, 2.3% FWHM (bottom).

3.3.5 The Importance of Signal Subtraction

To demonstrate the significance of signal subtraction in this geometry, let us compare the previous results to simulations of a spectrum formed from the collecting anode's preamplifier signal only. In this case, the weighting potential difference of the two anodes is replaced by just the collecting anode weighting potential, which is much less ideal – see Figure 3.11. The weighting potential analysis was again simulated using Maxwell 3D. It is interesting to compare Figure 3.8 and Figure 3.11 to note that without signal subtraction, the collecting anode's weighting potential distribution for 12 wires is less ideal than even the 2 wire case when signal subtraction is employed. This effect is somewhat offset by the improved electronic noise, since the subtracted signal's noise term is the quadrature sum of the noise from both anodes' preamplifiers.

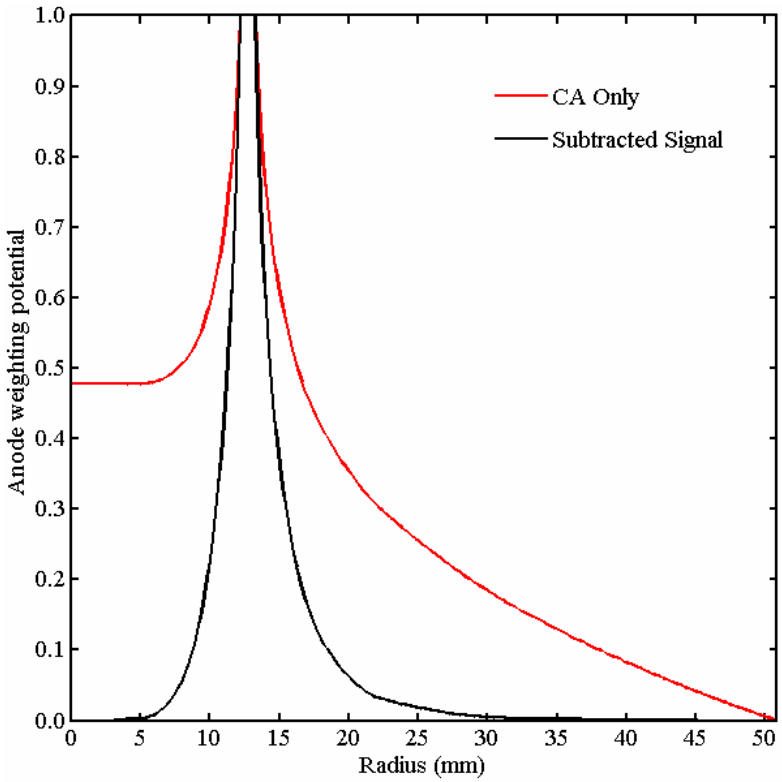

Figure 3.11. The simulated anode weighting potential difference compared to the weighting potential of the collecting anode only.

To quantitatively compare the expected pulse height spectra measured from the collecting anode and the subtraction circuit outputs, Geant4 simulations are repeated for

the 12 wire case with the only differences being (i) the electronic noise term and (ii) the weighting potential for induced charge calculations. Figure 3.12 displays the results of these two simulations for a ^{137}Cs gamma-ray source irradiating the detector uniformly over one end of the pressure vessel. Note that using only the collecting anode signal is expected to give much worse energy spectra – there is no defined photopeak. This coplanar-anode HPXe detector can therefore be expected to provide a viable alternative to gridded HPXe chambers only when signal differencing is employed.

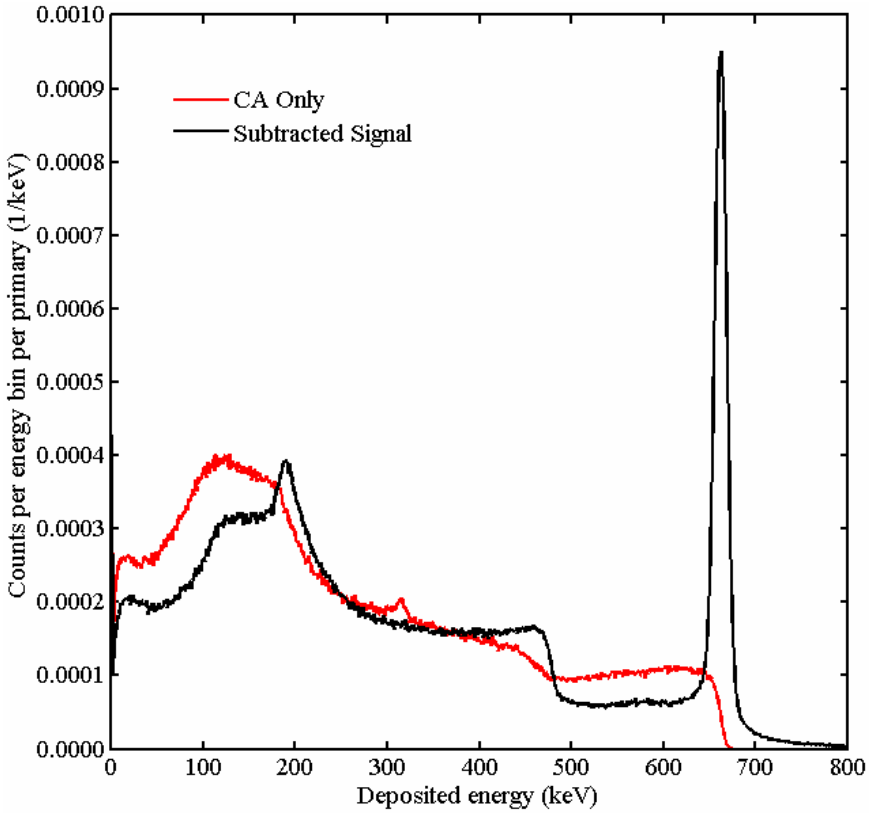

Figure 3.12. A comparison of simulated ^{137}Cs energy spectra for a 12-wire anode when signal subtraction is employed versus when only the collecting anode signal is utilized.

3.3.6 Estimating the Critical Electrode Biasing of the HPXe Chamber

Now that a geometry has been chosen, it is possible to use equations (3.8) and (3.9) in conjunction with the discussion of Section 2.2.3 to determine the critical biases

for full electron collection. For full collection of electrons at the collecting anode, the condition

$$\frac{\partial \varphi}{\partial r}\left(r = R_s, \theta = \frac{2\pi}{N_w} \right) \geq 0 \tag{3.18}$$

must be met, where R_s denotes the outer surface coordinate of the noncollecting anode wire. Let us also assume that a minimum electric field magnitude $E_{\min}$ must be maintained near the cathode for optimal extraction of electrons from the ionization site. It is easy to show from equation (3.8) that the azimuthal component of the electric field is zero at the cathode surface; thus, a second restriction on the operating bias is

$$-\frac{\partial \varphi}{\partial r}\left(r = R_{cat}, \theta \right) \geq E_{\min} \tag{3.19}$$

To solve for the critical conditions, let us determine the collecting anode and cathode operating biases φ_{CA} and φ_{cat} for which the inequalities (3.18) and (3.19) are just satisfied (the noncollecting anode is assumed to be grounded for this calculation). Only the region between the anodes and cathode is of concern: the region inside the anodes is known in advance to suffer from weak fields, but can be neglected due to its small fraction of the total gas space. For equations (3.9) to be solved, it is necessary to develop an expression describing the potential $\varphi_{\text{int}}(\theta)$ along the interface between the inner and outer solution regions. For simplicity, let us assume a simple cosine function oscillating between 0 and φ_{CA} as the azimuthal angle shifts from the noncollecting to the collecting anode:

$$\varphi_{\text{int}}(\theta) = \frac{\varphi_{CA}}{2}\left[1 + \cos\left(\frac{N_w}{2}\theta \right) \right] \tag{3.20}$$

In this simplified case, the Fourier coefficients A_n^{out} of equation (3.9) are greatly simplified, as only the first term in each summation is nonzero:

$$\begin{aligned} A_1^{out} &= \frac{\varphi_{CA}}{2\left[\left(\frac{R_{an}}{R_{cat}}\right)^{N_w/2} - \left(\frac{R_{an}}{R_{cat}}\right)^{-N_w/2}\right]} \\ B_0^{out} &= \frac{1}{\ln\left(\frac{R_{an}}{R_{cat}}\right)}\left(\frac{\varphi_{CA}}{2} - \varphi_{cat}\right) \end{aligned} \tag{3.21}$$

The coefficients in (3.21) can be substituted into equation (3.8) to obtain an approximation for the operating potential distribution throughout the detector, which can then be inserted into equations (3.18) and (3.19), thus producing a system of linear equations which can be solved easily using simple algebra:

$$\begin{aligned} -\frac{1}{\ln\left(R_{an}/R_{cat}\right)}\varphi_{cat} + \frac{1}{2}\left[\frac{1}{\ln\left(R_{an}/R_{cat}\right)} - \frac{N_w}{\left(R_{an}/R_{cat}\right)^{N_w/2} - \left(R_{an}/R_{cat}\right)^{-N_w/2}}\right]\varphi_{CA} &= -E_{\min}R_{cat} \\ -\frac{1}{\ln\left(R_{an}/R_{cat}\right)}\varphi_{cat} + \frac{1}{2}\left[\frac{1}{\ln\left(R_{an}/R_{cat}\right)} - \frac{N_w}{2}\frac{R_s}{R_{cat}}\frac{\left(R_s/R_{cat}\right)^{N_w/2-1} + \left(R_s/R_{cat}\right)^{-N_w/2-1}}{\left(R_{an}/R_{cat}\right)^{N_w/2} - \left(R_{an}/R_{cat}\right)^{-N_w/2}}\right]\varphi_{CA} &= 0 \end{aligned} \tag{3.22}$$

To obtain numerical values for the critical biases, one must substitute the known design values of $R_{an} = 12.7\,\text{mm}$, $R_{cat} = 50.8\,\text{mm}$, and $N_w = 12$. The minimum electric field strength is taken as the value at which the drift velocity of electrons saturates in the HPXe gas, which for the design density of 0.5 g/cm^3 is approximately $E_{\min} = 1250\,\text{V/cm}$ [48]. The final unknown is the location of the noncollecting anode surface, R_s. In the initial assumptions used to obtain equations (3.22), the wire has zero thickness in the radial direction; thus, it seems that $R_s = R_{an}$. This may lead to inaccuracies due to the true wire surface being located at a different position than assumed in the model; in addition, there are other assumptions that may introduce significant error into the

calculation, such as the assumption of a pure cosine distribution for $\varphi_{\text{int}}(\theta)$, which distorts the modeled field in the vicinity of the noncollecting anode wire. Nevertheless, the following approximate critical biases can be used as a guide for initial testing of the HPXe chamber, and can later be assessed for accuracy:

$$\begin{aligned} V_{cat}^{crit} &= -7.75\,\text{kV} \\ V_{CA}^{crit} &= +2.12\,\text{kV} \end{aligned} \tag{3.23}$$

CHAPTER 4

INITIAL EXPERIMENTS

4.1 Detector Preparation and Gas Filling

In Chapter 3 a coplanar-anode HPXe ionization chamber design was developed and optimized. In this section the detector construction will be described and shown, as will the gas purification and filling system used.

4.1.1 Detector Construction

Two detectors have been assembled using the design outlined in Section 3.1 with a 12-wire anode geometry. The pressure vessels are made of stainless steel: the outer wall is 1 mm thick to allow gamma rays to penetrate with minimal absorption and scattering, although the endplates are much thicker, 0.75 inch, for structural integrity. The three vessel components (two endplates and one central wall) are welded to form a strong and leak-proof union. The volume inside the pressure vessel is 6.5 inches in length with diameter 4.25 inches.

The active volume is supported by a smaller Macor cylinder placed inside the pressure vessel. Macor is chosen because it is an excellent insulator—its bulk resistivity is greater than 10^{16} Ω·cm [90]—which is important for minimizing leakage current between the electrodes and also for isolating the high-voltage cathode from the grounded pressure vessel. In addition, Macor does not outgas when it is properly baked [90], meaning it will not contaminate the purified HPXe gas. The cathode is formed by a layer of silver that is metallized on the inner wall of this Macor cylinder. The Macor also provides support for the anode structure, as the BeCu wires are fed through small holes machined in the Macor and fastened on either end. The primary detection volume,

bounded by this Macor structure, has both length and diameter 101.6 mm. The Macor is secured inside the pressure vessel by Macor spacers that hold the internal components in place.

Figure 4.1. A photograph of the anode structure in a test assembly. The connection scheme used to group the wires into two signal electrodes is apparent.

Figure 4.2. A photograph of the detector prior to final assembly.

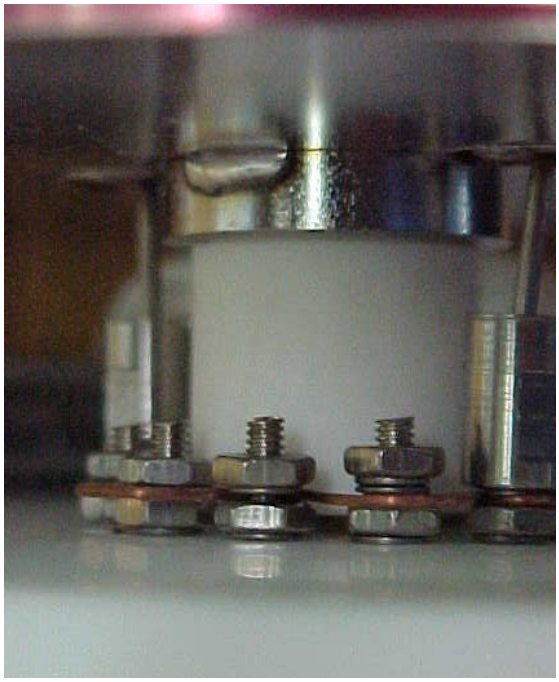

Figure 4.3. A photograph of the Macor spacer (center, white) that separates the pressure vessel (top) from the main Macor internals (bottom).

Figure 4.1 shows the anode wires in a test assembly; this picture illustrates the arrangement of the wires and how connections are made at the end of the detector to cluster the wires into two anodes (collecting and noncollecting groups of six wires each). Figure 4.2 shows the anode wires protruding from a Macor structural shell prior to insertion into the steel pressure vessel. Figure 4.3 portrays one end spacer used to secure the internal components.

4.1.2 Gas Purification and Detector Filling

Extreme care must be taken to properly purify the xenon fill gas prior to filling. The presence of electronegative molecules severely degrades chamber performance; to ensure good performance, impurities such as O_2, CO, CO_2, and organic molecules must be reduced in concentration to at most 0.5 ppm [49, 91]. To obtain this high gas purity, research-grade xenon is introduced into a spark chamber with titanium electrodes. A continuous discharge between these electrodes is established, which creates a cloud of titanium dust. This dust absorbs the electronegative impurities very efficiently; one benefit of this method is that the dust can continue to further purify the gas even if the

power supply to the electrodes is shut off. This purification technique can produce electron lifetimes in the HPXe gas that rise above 1 ms, ensuring that at most only a few percent of electrons are lost prematurely due to attachment.

In addition to gas purification, the interior detector surfaces and the inner walls of the transfer pipes between the spark chamber and the detector must be scrubbed of all impurities that might contaminate the gas. To accomplish this goal, the appropriate components were wrapped in heat tape and held at a temperature of about 125ºC for several days to accelerate outgassing of impurities from the surfaces. The system was placed under a high vacuum (10^{-7} torr) to evacuate the system of all gas and to ultimately remove impurities that diffuse from the piping and detector surfaces. A schematic of a typical purification and filling station is shown in Figure 4.4, reprinted from Bolotnikov and Ramsey [91]. The getter, oxisorb, and sampling cylinder can be used for initial purification of the xenon gas, but in this case the gas was introduced directly into the spark purifier via the test chamber port prior to detector baking.

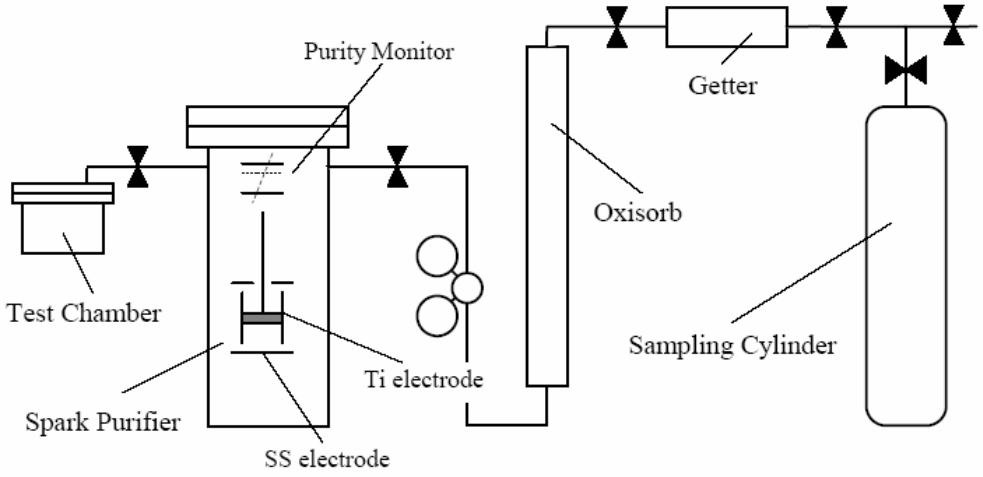

Figure 4.4. A typical HPXe purification and filling station using a spark purifier.

Once the baking and purification processes were complete, the heat tape was removed, the valve lineup changed, and the detector filled with HPXe gas. The final gas density in the detectors was approximately 0.28 g/cm^3 in detector HPXe1 and 0.25 g/cm^3 in detector HPXe2, as determined by the measured change in detector mass and the known volume of the gas space. These densities are well below the design value of 0.5

g/cm^3, but due to problems with the filling procedure these were the final detector states. To estimate the corresponding critical electrode biases, the values calculated in Section 3.3.6 only need to be scaled by the experimental-to-design density ratio, since the critical electric field for drift velocity saturation scales linearly with density.

4.2 Experiments

The initial experiments with these detectors tested some fundamental properties of the detectors, such as detector capacitance, electronic noise, and linearity, and explored the limits on the applied biases. These parameters are important for both characterizing the detector and also understanding its performance.

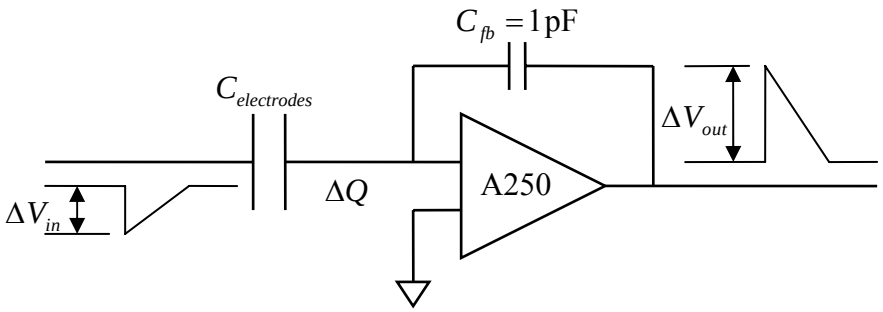

Figure 4.5. A diagram of the capacitance measurement concept.

4.2.1 Capacitance Measurements

The capacitance between the two anodes and also between an anode and the cathode were measured experimentally. (Due to symmetry, it was unnecessary to measure the cathode-noncollecting anode capacitance.) A schematic of the measurement technique is shown in Figure 4.5. The procedure used was to input a known test pulse with amplitude ΔV_{in} directly onto either the cathode or the noncollecting anode, and then to measure ΔV_{out} from the collecting anode preamplifier while this electrode is grounded. The relationship between ΔV_{in} and ΔV_{out} is very simple:

$$\Delta Q = C_{electrodes}\Delta V_{in} = \underbrace{C_{fb}}_{=1\text{pF}}\Delta V_{out}$$
$$C_{electrodes}\left(\text{pF}\right) = \frac{\Delta V_{out}}{\Delta V_{in}} \tag{4.1}$$

Thus it is straightforward to calculate the capacitance between two electrodes.

The test pulse injected on the opposing electrode is given time constants similar to a true gamma-ray signal. The measured capacitances are found in Table 4.1; these values are representative of both the HPXe1 and HPXe2 detectors. The total detector capacitance is the combination of the measured values in parallel, or 21.9 ± 2.0 pF per preamplifier. This experimental result agrees with the detector capacitance predicted with Maxwell 3D simulations—22.8 pF.

Table 4.1. Measured capacitance values for the HPXe detectors.

Electrode Pair	*Cathode-Anode*	*Anode-Anode*	*Vessel-Anode*	*Total Anode*
C (pF)	1.6 ± 0.2	11.7 ± 1.6	8.6 ± 1.2	21.9 ± 2.0

4.2.2 Electronic Noise Measurements

Electronic noise is important to quantify because it places a lower limit on a detector's energy resolution. It is also possible to compare the actual electronic noise of a system, which is normally dominated by the preamplifier, against the manufacturer's data to establish whether or not the equipment is performing as expected. To make this type of comparison, the electronic noise measurement must be calibrated on an absolute scale.

The measurement begins with a separate Amptek A250 preamplifier connected to each anode of the HPXe chamber. A test pulse of known amplitude ΔV_{in} is injected into one of the preamplifiers, the output of the preamplifier stage is filtered and amplified using a shaping amplifier, and this shaped amplitude is measured using a multichannel analyzer (MCA). Because the test pulse voltage signal ΔV_{in} is placed across a capacitor $C_{test} = \left(2.0 \pm 0.1\right)\text{pF}$ in the A250 test board, it creates a charge at the operational amplifier's inverting terminal of magnitude

$$\Delta Q_{test} = C_{test} \Delta V_{in} \tag{4.2}$$

By using multiple known test pulse amplitudes, the MCA can be calibrated in units of charge. Assuming the test pulse amplitude has negligible variation, the electronic noise of the system in units of equivalent noise charge (ENC) is simply the standard deviation of the measured pulse height distribution, or assuming a normal distribution of pulse heights,

$$ENC\left(e^{-}\right) = \frac{FWHM\left(C\right)}{2.35} \frac{1e^{-}}{1.602 \times 10^{-19} C} \tag{4.3}$$

This calibration can be performed using multiple shaping time constants to determine the optimal time constant for minimizing the noise contribution. The electronic noise contribution of the preamplifier is expected to pass through a minimum at some shaping time corresponding to a balance between series noise—such as thermal noise in the FET and feedback resistor that is dominant at short shaping times—and parallel noise, an example being the detector leakage current shot noise that becomes problematic at long shaping times [8]. It is important to note that the optimal shaping time constant does not necessarily correspond to the best measured energy resolution: if the charge transit time through the detector is not short compared to the shaping time, ballistic deficit concerns will increase the ideal shaping time constant.

Using the measurement procedure described above, the electronic noise of the system was quantified at various shaping times. For these experiments the detector was not biased; the results may change somewhat under operating conditions if, for example, leakage current between the electrodes becomes significant. The output of the subtraction circuit was analyzed since this is the primary signal of interest; the measured system noise is expected to be larger than the output of just a single preamplifier because the difference signal incorporates noise from both preamplifiers as well as any fluctuations introduced by the subtraction circuit. Two different shaping amplifiers were used to test a larger sample of shaping time constants. The ORTEC 672 shaping amplifier proved to be lower noise than the Canberra 243, which can be verified easily by

comparing the results from these two amplifiers at a shaping time of 2 μs. All ENC results are displayed in Figure 4.6, with the corresponding limit on energy resolution for HPXe shown in the bottom panel. The optimal electronic noise is achieved with a shaping time of 6 μs, placing a lower limit on energy resolution of 2.7% FWHM at 662 keV.

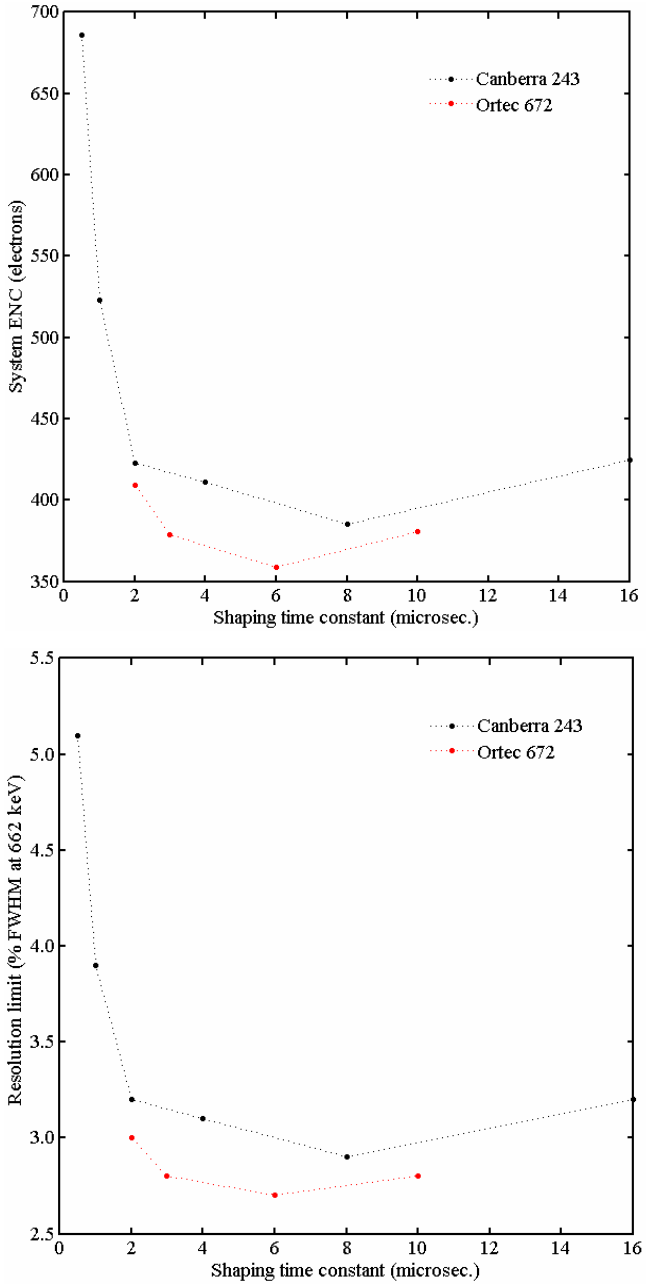

Figure 4.6. Measured ENC (top) and the corresponding energy resolution limit (bottom) as a function of shaping time for the HPXe detection system.

4.2.3 Preamplifier Waveforms

As the detector operating biases were increased during the experiments, the preamplifier waveforms were monitored on an oscilloscope. As the cathode bias was changed from 0 to -4500 V, the measured rise time of the subtraction circuit output shortened noticeably, from around 50 μs to approximately 5 μs, as presented in Table 4.2. It is important to remember that although the actual charge transit time is much longer than these values, the implementation of coplanar anodes and signal subtraction creates an idealized signal that registers no response from charge carrier motion through most of the detector, followed by a sharp rise when the electrons have approached the anode structure. This difference can clearly be seen in Figure 4.7, which shows the measured collecting and noncollecting anode preamplifier waveforms along with the subtraction circuit output. The cathode bias is -4000 V for this particular measurement; the collecting anode is held at +1300 V. The individual anodes show a total charge transit time of near 40 μs, while the 5 μs subtracted output rise time allows a shaping time of 16 μs to be used.

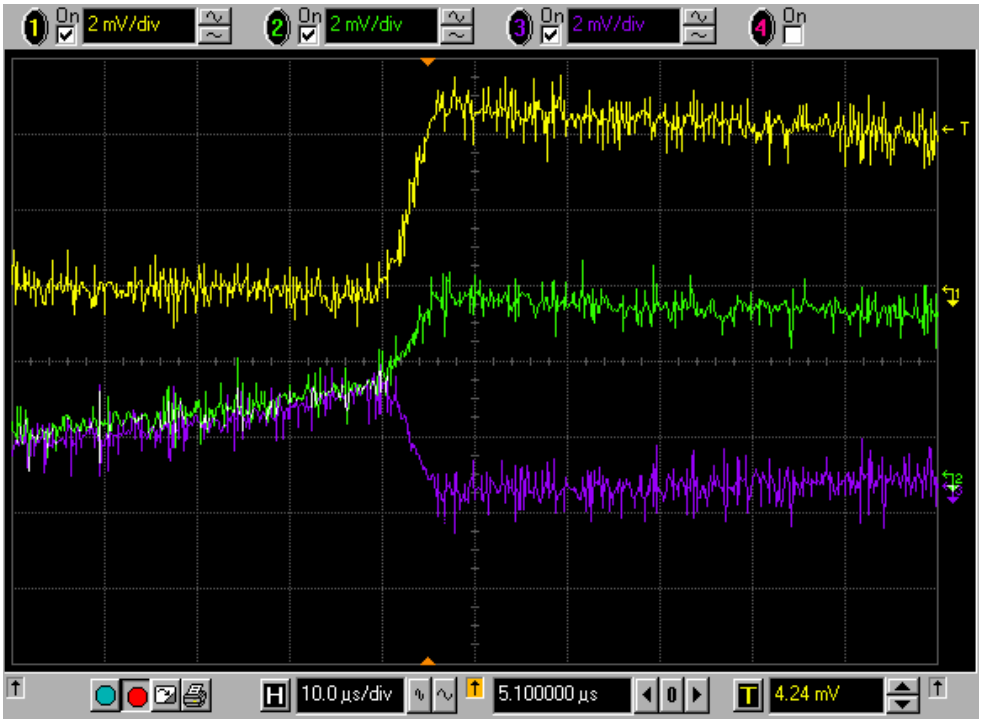

Figure 4.7. Measured collecting (green) and noncollecting (blue) anode waveforms, shown with the subtraction circuit output (yellow). The horizontal axis is 100 μs long, and the vertical axis is 16 mV in amplitude.

Table 4.2. Subtracted signal rise time vs. cathode bias while the anodes are grounded.

Cathode Bias	*Subtraction Circuit Signal Rise Time*
-1000 V	≥50 μs
-2000 V	25 μs
-3000 V	10 μs
-4000 V	~5 μs

4.2.4 Cathode Biasing Spectra

The purpose of the first set of measurements using a ^{137}Cs gamma-ray source was to determine the necessary applied cathode bias to approach complete electron collection and minimize ballistic deficit for all events. This was achieved by recording pulse-height spectra at 500-volt intervals and looking for the point at which spectral changes ceased. The collecting and noncollecting anodes are both grounded for this series of experiments.

The experimental setup for this set of experiments is very simple, and is presented in the block diagram of Figure 4.8. This figure shows one of the advantages of using coplanar grids: other than the use of two preamplifiers and a simple subtraction circuit, the experimental setup is quite conventional for gamma-ray spectroscopy, relying only upon standard equipment.

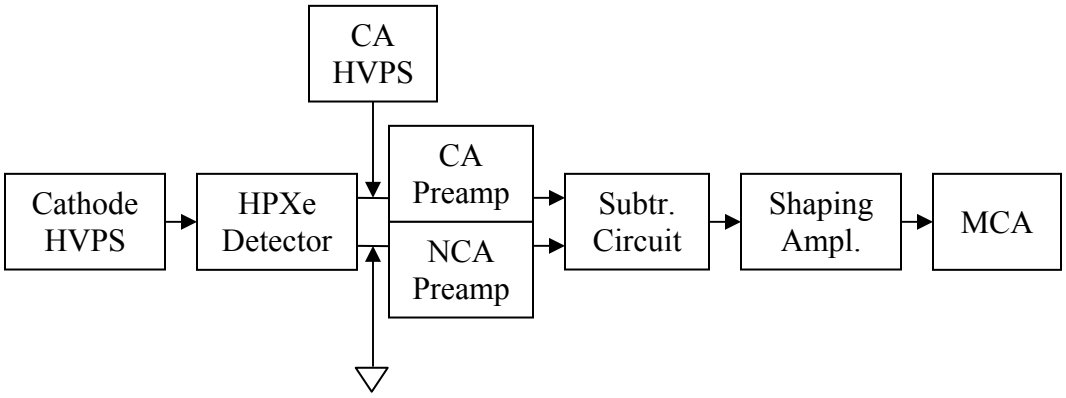

Figure 4.8. A block drawing of the equipment setup for gamma-ray experiments.

Figure 4.9 shows a subset of the data acquired from this experiment. The energy spectra presented are unusual—there are counts in negative channel bins. This is because the output of the subtraction circuit can be either positive or negative, depending upon the amplitude and polarity of both the collecting and noncollecting anode signals. Since both anodes are grounded, electrons will not drift preferentially toward one anode or the other; furthermore, the wire symmetry makes electrons equally likely to be collected on either anode. Thus, over a large number of interactions, the expected energy spectrum will be symmetric about the vertical axis. To obtain this spectrum using a conventional MCA, first a spectrum was collected with the shaping amplifier set to positive output polarity, then a separate spectrum was collected using inverted polarity. The two halves of the spectrum were then stitched together manually. The region around the vertical axis appears to have no counts because of the lower-level discriminator (LLD) setting on the multichannel analyzer.

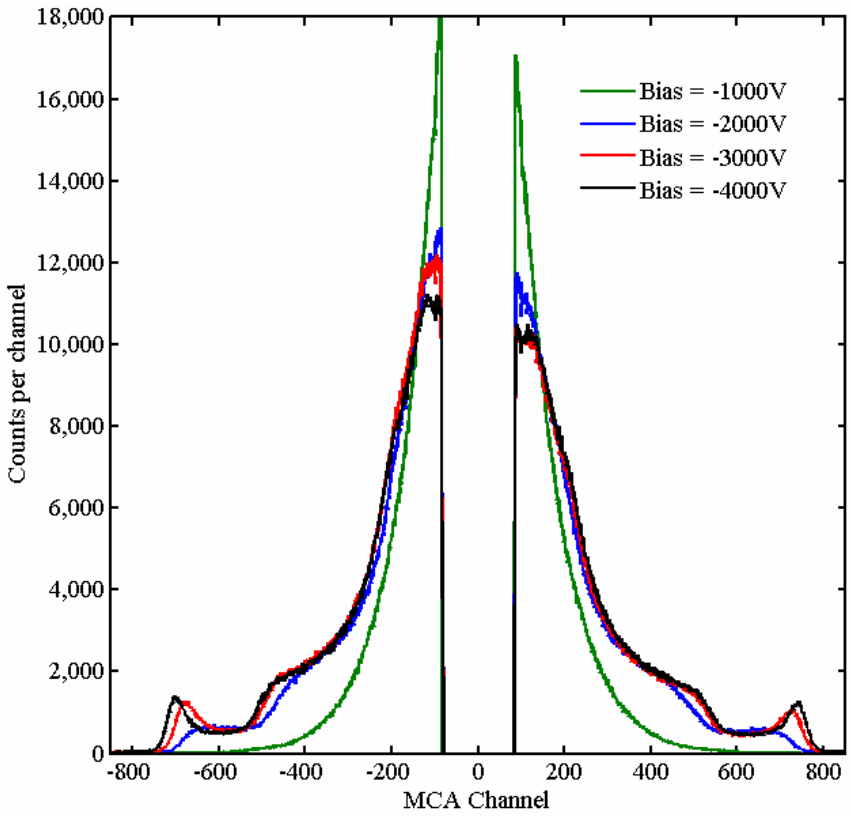

Figure 4.9. ^{137}Cs gamma-ray spectra as a function of the applied cathode bias when both anodes are grounded.

In Figure 4.9 the spectra are not quite symmetric about the vertical axis as expected. This implies that the subtraction circuit may not be tuned perfectly, and as a result the gain of the noncollecting anode signal is about 5% less than that of the collecting anode. This also accounts for there being more counts per channel in the negative portion of the spectrum—the gain difference compresses the same number of counted events into fewer bins. The data for cathode biases beyond -4000 volts showed no visible changes in the spectrum, implying both that nearly all of the electrons are being collected and also that the electron drift velocity has saturated near 1 mm/μs through most, if not all, of the detection volume.

4.2.5 Anode Biasing Spectra

Now that an appropriate cathode bias of -4000 V has been established, the next step is to start utilizing the anodes properly by increasing the applied bias on the collecting anode (the noncollecting anode is grounded throughout all experiments). The goal is to shape the electric field locally around the anodes such that all electrons drift to the collecting anode wires. As the collecting anode bias is increased, electron collection will occur more frequently on the collecting anode than on the noncollecting anode wires, and thus the negative subtracted signals are expected to diminish in amplitude and frequency as the positive signal amplitudes and frequency increase.

Figure 4.10 presents a subset of the experimental data. As expected, increasing the collecting anode bias gradually shifts the negative-polarity pulses toward positive energies. The photopeak FWHM does not seem to improve when the collecting anode bias is raised above 400 V, even though electron collection at the collecting anode is far from complete at that point: this implies that other sources of peak broadening dominate the measured FWHM. Electronic noise contributes significantly to photopeak broadening, as quantified with a test signal. The test peak has a width of 32.3 keV, thus placing a 4.9% FWHM lower bound on the energy resolution. The measured photopeak resolution is 6.8% FWHM at 662 keV when employing collimators to direct the incident radiation upon the midplane of the detector, calculated using the peak fitting routine in the ORTEC® MAESTRO-32 MCA software [92].

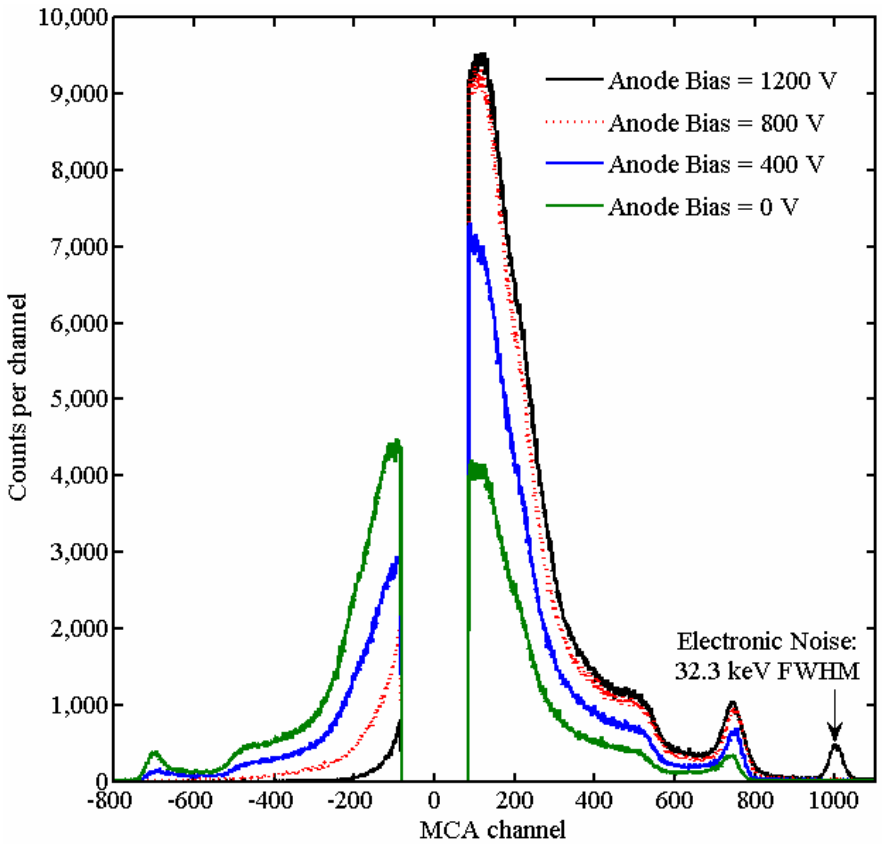

Figure 4.10. ^{137}Cs spectra as a function of collecting anode bias with the noncollecting anode grounded and the cathode held at -4000 V.

One easy way of experimentally estimating the critical bias for complete electron collection at the collecting anode is to also pass the noncollecting anode's preamplifier signal to a shaping amplifier and register the number of counts above a fixed discrimination level (preferably set just above the noise level). As the collecting anode bias is increased, electrons will be collected less frequently on the noncollecting anode wires; as a result the measured signals from this electrode will tend to become more negative as the collecting anode bias increases. Let us consider the induced signal on the noncollecting anode ΔQ_{NCA} using the Shockley-Ramo theorem. The total drifting charge q is the sum of the total charges collected on the collecting and noncollecting anodes, q_{CA} and q_{NCA} respectively, absent charge recombination. Then, assuming the weighting potentials of the collecting and noncollecting anodes at the ionization site, φ_0^{CA} and φ_0^{NCA},

are very nearly equal—as expected for a good coplanar anode design—then they can be replaced simply by φ_0, and the signal under consideration is

$$\begin{aligned}\Delta Q_{NCA} &= -q_{CA}\left(0-\varphi_0^{CA}\right)-q_{NCA}\left(1-\varphi_0^{NCA}\right)\\ &= -q\left(1-\varphi_0-\frac{q_{CA}}{q}\right)\end{aligned} \tag{4.4}$$

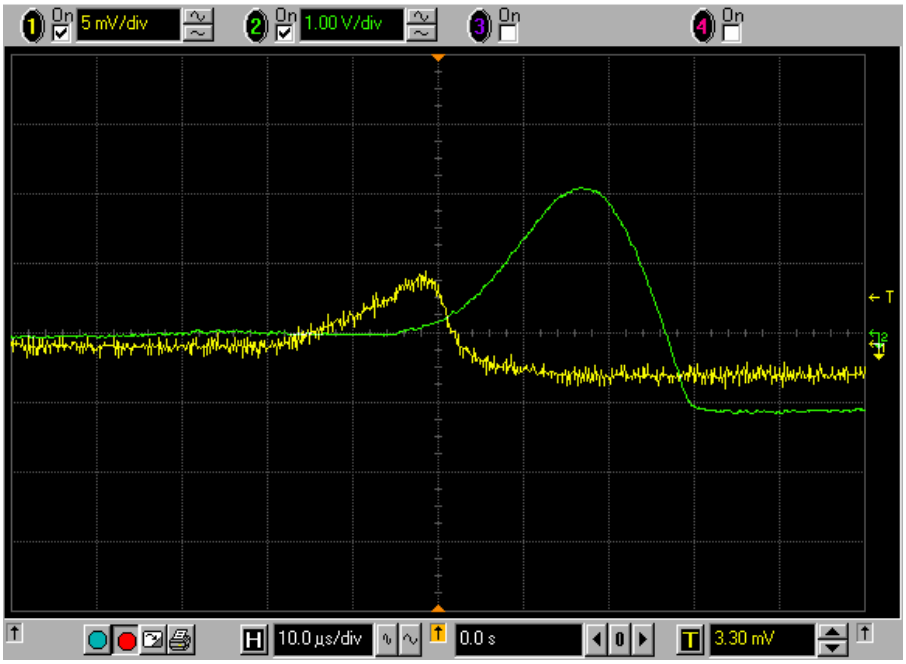

Figure 4.11. A preamplifier waveform from the noncollecting anode (yellow) and the shaped signal (green). The shaping time used is 16 µs.

Optimal charge collection can be estimated as the point at which the positive noncollecting anode counts disappear. This is demonstrated by setting $q_{CA} = q$ in equation (4.4) while noting that $\varphi_0 \geq 0$ and q is negative. Strictly this statement is not quite true when pertaining to the filtered signal that is measured in an experiment, because even if all electrons are properly collected, the noncollecting anode signal transient can create a shaped signal with a significant positive lobe. This is demonstrated by the waveforms shown in Figure 4.11: even though the overall change in preamplifier output voltage (yellow) is negative, the signal remains positive for about 22 µs, and with

a 16 μs shaping time constant this generates a shaping amplifier output amplitude of +2V (green), well above the detection threshold.

Positive noncollecting anode count data were obtained with the cathode biased at -4500 V and a ^{137}Cs source present; this data is presented in Figure 4.12. The lower-level discriminator setting corresponds to about 50 keV; decreasing the discriminator setting beyond this point introduced large system dead time fraction (greater than about 15%). The uncertainty bars are not presented in the figure because they are too small to be distinguished from the data points. It is evident that at 1400 V the detector is still not optimally biased, but beyond this point discharging began and data was not collected in the interest of protecting the equipment. The background count rate was measured, and from this it is apparent that a large fraction of the measured counts are true source events.

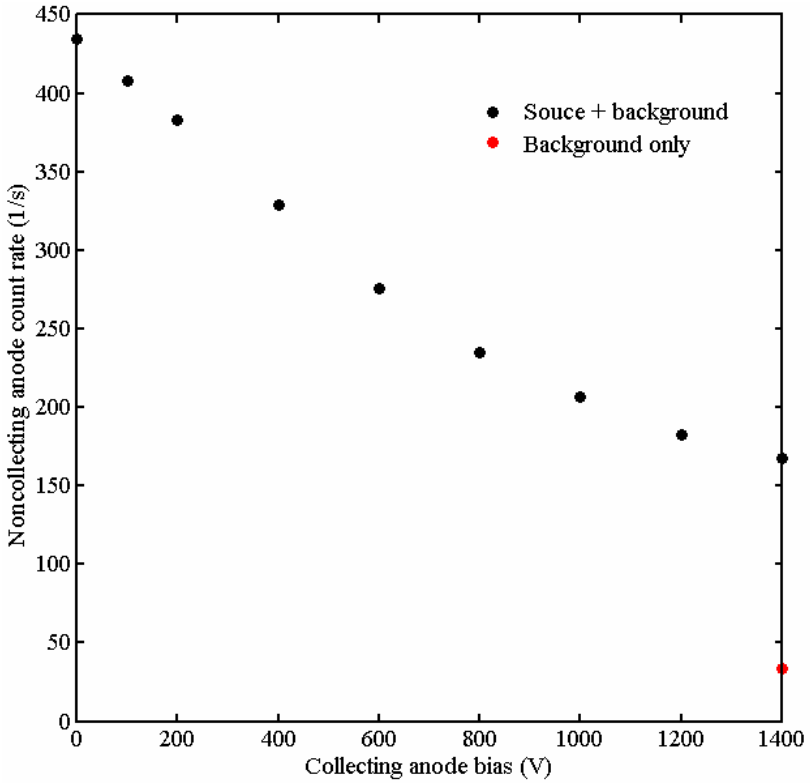

Figure 4.12. The number of positive noncollecting anode counts as a function of the collecting anode bias; the source is ^{137}Cs, and the cathode is held at -4000 V.

Monitoring the preamplifier waveforms on the oscilloscope provides a second method of determining the critical biasing condition of the detector. If electrons are

drifting to the noncollecting anode, then some events will be observed to exhibit a net positive change in the noncollecting anode's preamplifier signal.

4.2.6 Effects of Background Radiation and Source Collimation

To determine the degree of response uniformity along the axial coordinate, the ^{137}Cs point source was collimated using lead bricks to irradiate ¼-inch axial slices of the detector. The collimated beam was focused upon three different locations: the center of the detector and the gas spaces at either end of the HPXe chamber. These results were compared to the uncollimated case in which the entire chamber was exposed to the gamma-ray source.

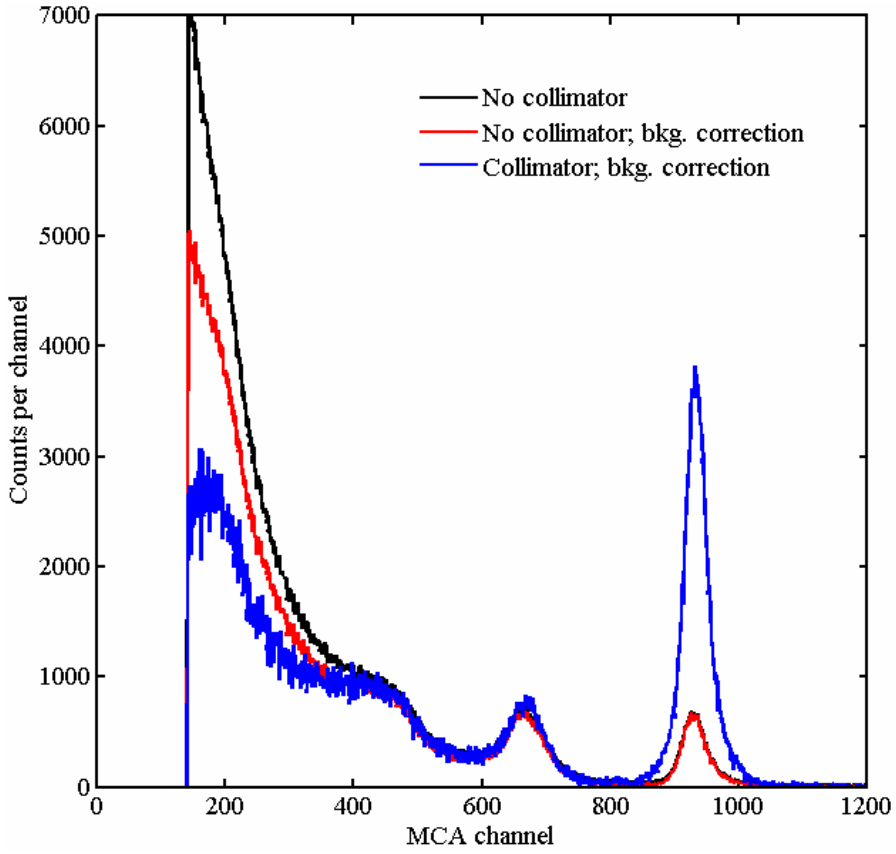

Figure 4.13. The effects of background correction (red) and source collimation (blue) on the raw ^{137}Cs spectrum (black). A test pulse is centered near channel 925.

In addition, the effect of background radiation on the measurements was quantified by collecting a spectrum under equivalent biasing and shaping conditions

without the ^{137}Cs point source present. Figure 4.13 demonstrates the effects of first applying a background correction to the measured spectrum, then collimating the source at the center of the detector. For this particular series of measurements, the applied biases were -4500 V on the cathode and +1400 V on the collecting anode; the shaping time is 16 μs, and the MCA live time is 1800 s. The net effect of these two "corrections" is to greatly reduce the count pileup near 200 keV; about half of the total difference comes from background events, the other half is apparently due to nonuniform response along the chamber's axis.

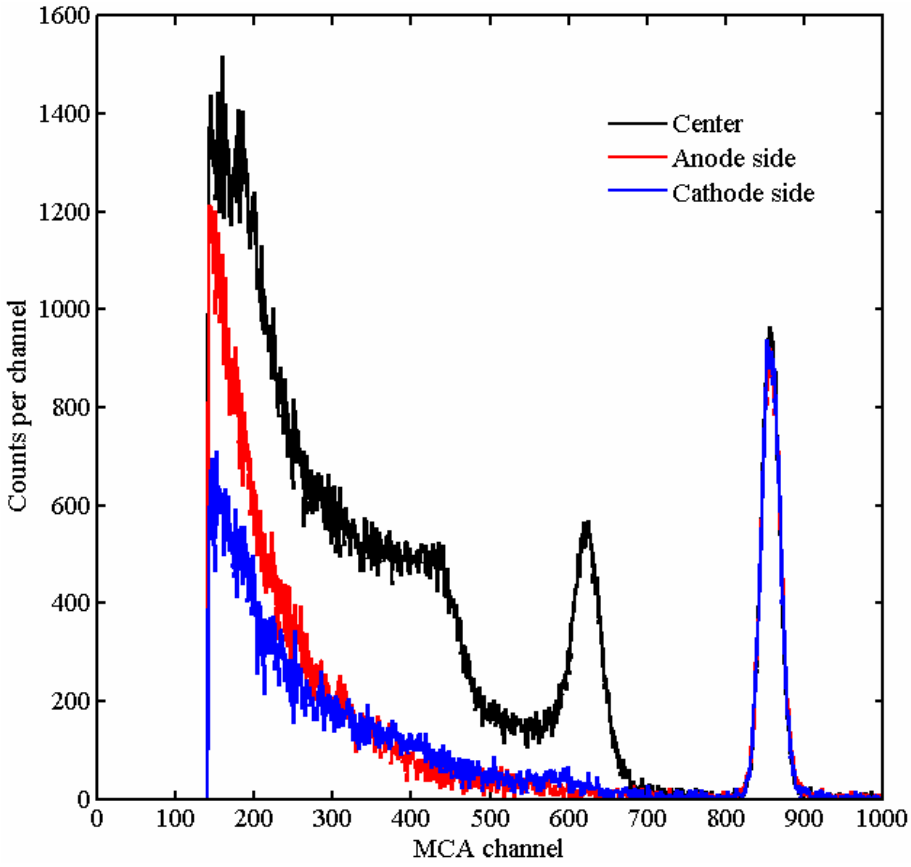

Figure 4.14. The detector response with the source collimated upon the detector center (black) and the opposing end gas spaces where the anode (red) and cathode (blue) lead wires are located.

Figure 4.14 demonstrates the effect of beam location on the detector response. For this set of experiments the shaping time has been reduced to 12 μs; background has been subtracted from all of the spectra presented. It is demonstrated that the end regions

do not contribute to the photopeak at all: these volumes are evidently responsible for much of the drastic count rate increase measured in the Compton continuum near 200 keV. The reason for this is likely due to the low fields and nonuniform weighting potential in these end gas spaces. The cathode does not extend into these spaces, so their boundaries are mostly formed by the pressure vessel, which is held at ground potential. The slight differences in the spectra can be explained by the difference in field strength on the two ends resulting from the anode lead wires penetrating one end versus the cathode lead wire in the other end. The cathode bias wire creates a stronger field, which results in the pulse distribution being shifted to higher energies.

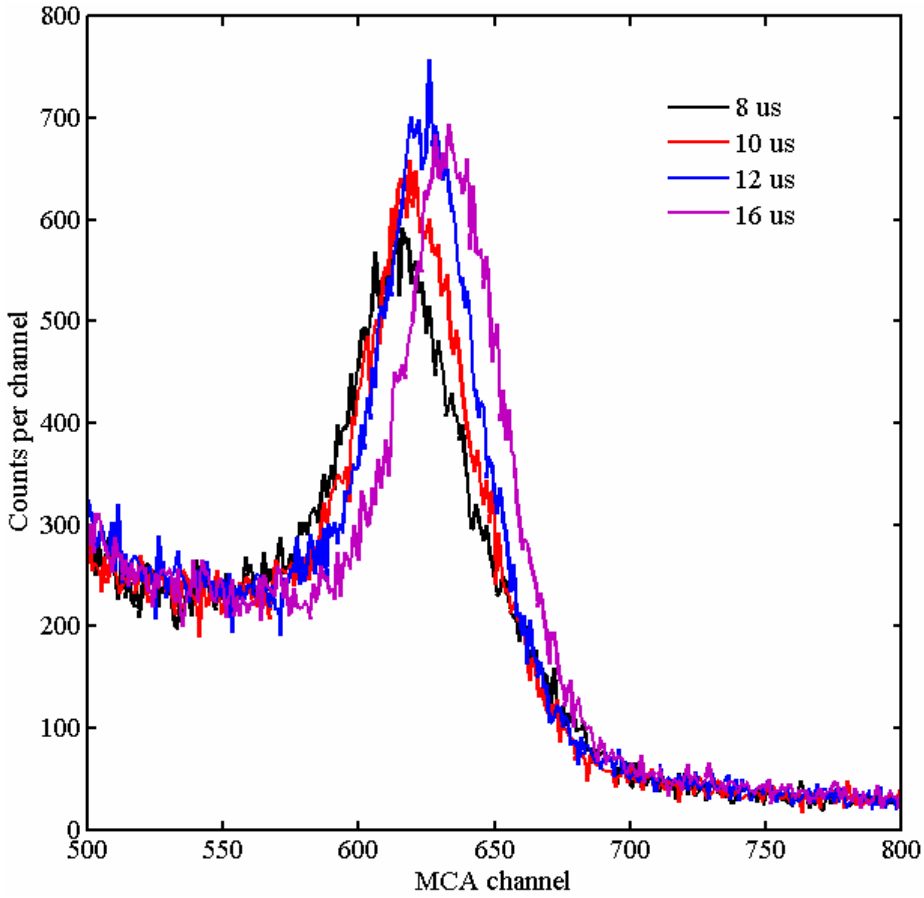

Figure 4.15. The change in the photopeak region for a selection of Gaussian filters using shaping times from 8 to 16 μs.

4.2.7 Optimal Shaping Filter

The optimal shaping time will minimize the width of the photopeak in the measured spectrum. This is not necessarily the same time constant as that which minimizes electronic noise, since peak broadening due to ballistic deficit may be important for shaping times that are not long compared to the preamplifier signal rise time. Employing source collimation upon the central detector plane but not background correction, ^{137}Cs energy spectra were recorded for several shaping time constants: 8, 10, 12, and 16 μs. The applied biases were again -4500 V on the cathode and +1400 V on the collecting anode, and the MCA live time is unchanged at 1800 s. The experimental results are shown in Figure 4.15: clearly the 8 μs data prove that this time constant is too small, but the other three choices give fairly close results. The 12 μs shaping time provides slightly better energy resolution than the other time constants.

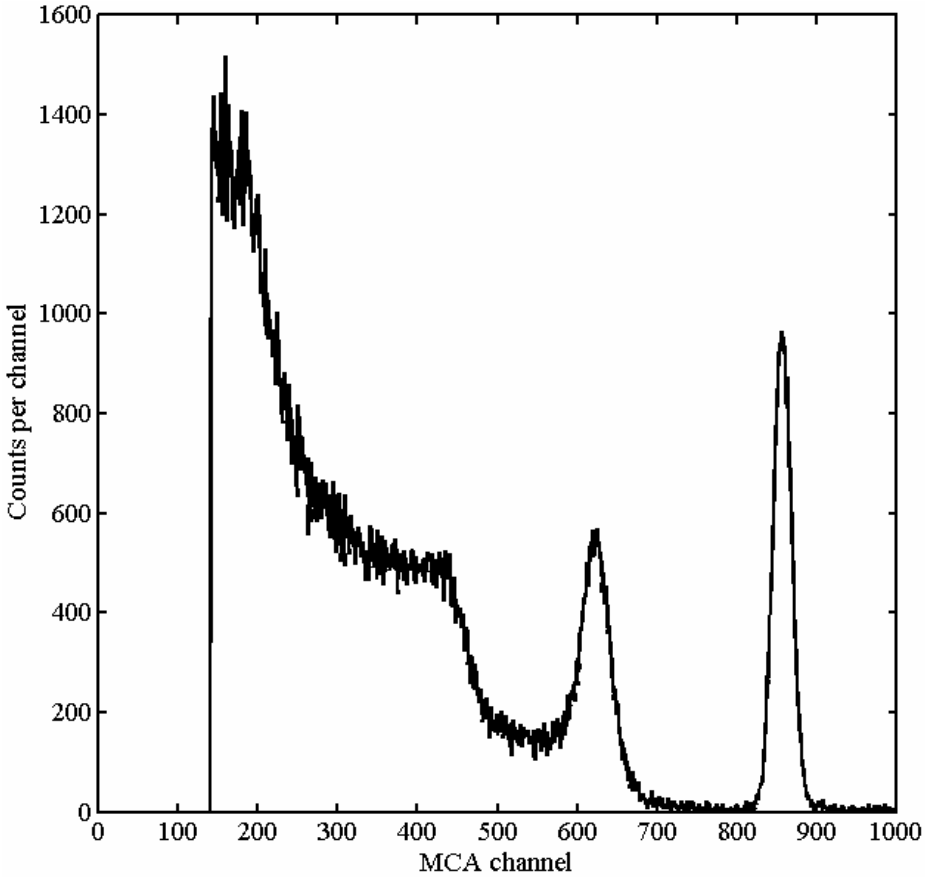

Figure 4.16. The optimized ^{137}Cs energy spectrum exhibits a 6.0% FWHM energy resolution and greatly reduced counts in the lower part of the Compton continuum.

In addition, the shaping amplifier allowed either Gaussian or triangular filtering. The triangular filter was found to be superior in similar testing, providing a measured resolution of 6.0% vs. 6.4% FWHM at 662 keV using the MCA peak analysis software and an identical region of interest. The final energy spectrum, which uses the optimal filter plus collimation upon the central detector plane and a background correction, is shown in Figure 4.16.

4.2.8 System Linearity

A final important test of the system is to determine its linearity in response to a wide range of gamma-ray energies. Previous HPXe systems have been shown to have excellent linearity [24, 27, 43, 50], thus a linear response is expected to be measured with this detector.

For this experiment, the system settings were: -4500 V cathode bias and +1400 V collecting anode bias, a triangular shaping filter with a 12 μs time constant, collimation upon the central plane of the detector, and the MCA live time was increased to 7200 s. Background was measured and subtracted to enhance the lower-energy peaks. The sources used are listed in Table 4.3, along with the corresponding gamma-ray energies and intensities [93], plus the measured photopeak centroids. The measured spectrum is presented in Figure 4.17. The ^{60}Co 1173.2 keV peak cannot be easily discerned from the nearby Compton edge of the 1332.5 keV line, which lies at 1118.1 keV. The recorded channel number as a function of gamma energy is displayed in Figure 4.18, plotted along with the calculated linear least-squares fit line. The length of each half error bar (either the half above or below the data point) corresponds to one standard deviation of measured peak width, calculated from the measured FWHM and assuming a Gaussian distribution of counts in the photopeak. It is evident from this figure that the linearity of the HPXe detection system is quite acceptable.

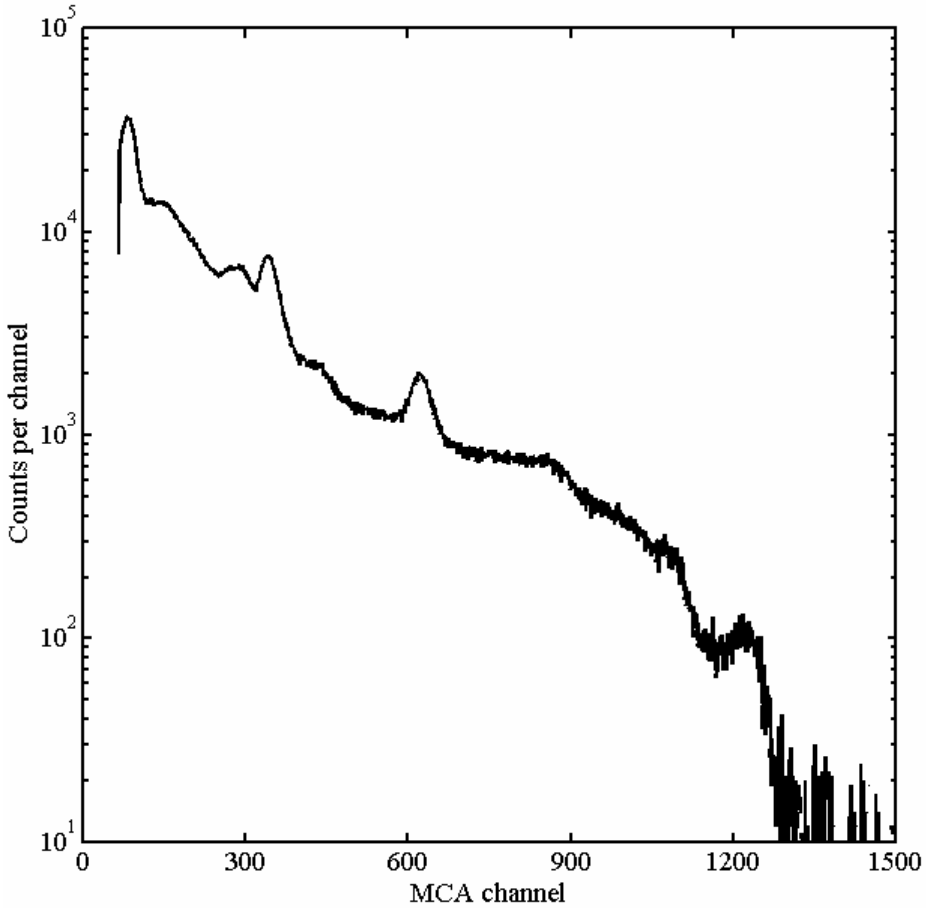

Figure 4.17. A spectrum collected with ^{133}Ba, ^{137}Cs, and ^{60}Co gamma-ray sources.

Table 4.3. Sources used in the linearity measurement along with photopeak properties.

Source	*Energy (keV) / Intensity (%)*	*Measured Centroid (channels)*	*Measured FWHM (channels)*
^{133}Ba	81.0 keV (34.1%)	85.18	20.50
^{133}Ba	302.9 keV (18.3%)	285.66	36.61
^{133}Ba	356.0 keV (62.1%)	343.38	29.68
^{137}Cs	661.7 keV (85.1%)	622.60	36.97
^{60}Co	1173.2 keV (99.9%)	-	-
^{60}Co	1332.5 keV (100.0%)	1219.38	48.25

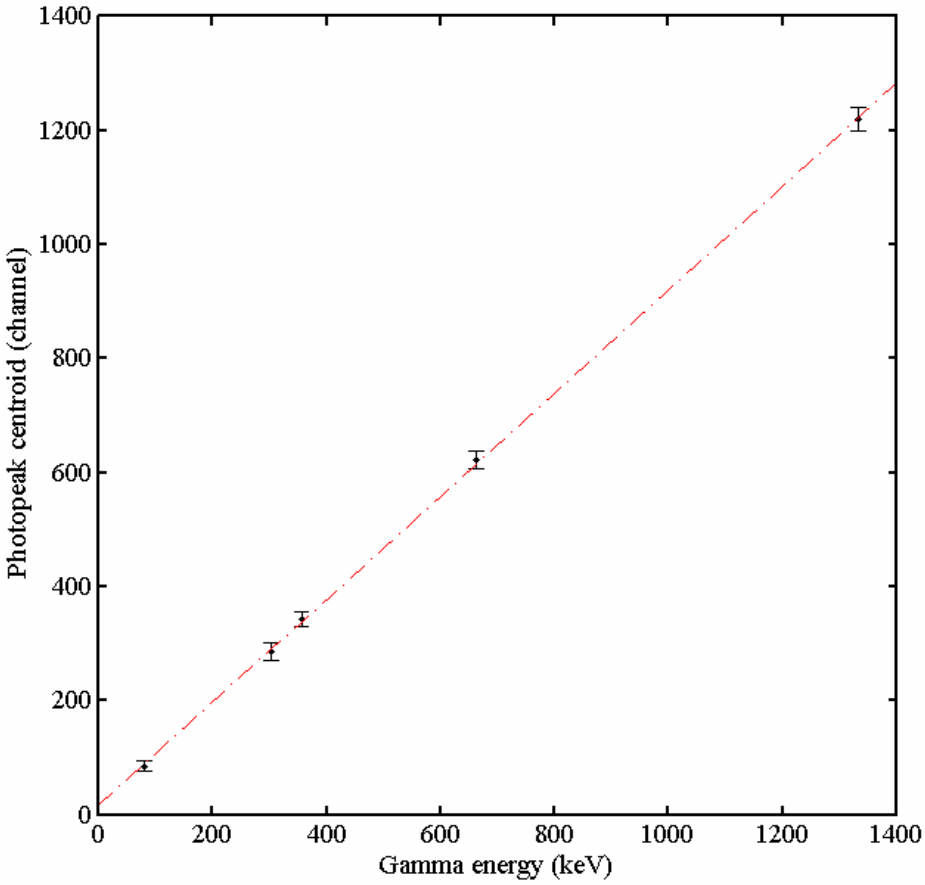

Figure 4.18. The measured photopeak centroid plotted against the true gamma-ray energy (black). Total error bar lengths correspond to two measured standard deviations. The linear least-squares solution is also displayed (red).

Table 4.4. The departure of measured peak centroids from the least-squares solution.

Gamma-Ray Energy (keV)	*Absolute Deviation (channels)*	*Relative Deviation (% of FWHM)*	*Relative Deviation (% of centroid)*
81.0	-4.04	-19.7	-5.51
302.9	-4.60	-12.6	-1.68
356.0	5.01	16.9	1.55
661.7	7.27	19.7	1.21
1332.5	-3.70	-7.7	-0.31

The deviation of each measured photopeak centroid from the least-squares solution is listed in Table 4.4. The maximum absolute deviation is 7.27 channels for the

^{137}Cs point source, which corresponds to 8.02 keV departure from the expectation value. The deviations are relatively small compared to the measured FWHM of each peak, with the maximum being 19.7% of the measured FWHM. The deviations are also a small percentage of the true gamma energies, with all cases except the lowest energy being less than a 1.7% shift from the expected peak location.

4.2.9 Discussion of Preliminary Results

In these first experiments of the coplanar-anode HPXe chamber, the preamplifier noise contribution was quantified as a function of amplifier shaping time. It was found that the best noise performance occurs at a shaping time of 6 μs, which is too short to avoid ballistic deficit when the working gas is pure xenon. A shaping time constant of either 12 or 16 μs was used for all experiments, appropriate for the measured pulse rise times of about 5 μs.

The detector was biased in incremental steps to determine the minimum cathode and collecting anode voltages to ensure full and proper collecting of electrons. A cathode bias of -4000 V was found appropriate for collection of events throughout the entire detection volume; the minimum collecting anode bias for proper coplanar operation could not be achieved, as discharging occurred before this operational point was reached.

The spectrum recorded with ^{133}Ba, ^{137}Cs, and ^{60}Co exhibited good linearity over a range of gamma-ray energies from 81.0 keV to 1332.5 keV. All major gamma lines could be measured except the 1173.2 keV line from ^{60}Co, which was obscured by the presence of the nearby Compton edge at 1118.1 keV corresponding to the 1332.5 keV gamma ray. The maximum deviation of a measured photopeak centroid from the least squares solution is 8.02 keV, and all deviations fall well within the measured photopeak FWHM.

In Figure 4.10 the collected spectra all exhibit a rather extreme change in the Compton continuum count rate between channels 200 and 400. This effect is also present in many published HPXe results; for example, refer to [35]. There are two common theories used to explain this feature: one oft-cited possibility is related to the slow drift of electrons in xenon gas, expected to be about 1 mm/μs in the high-field region near the anodes and about 0.5 mm/μs near the cathode using published drift velocity data [94];

this agrees with experimentally-observed electron transit times of nearly 50 μs over the 38 mm cathode-anode spacing. In the case of gamma rays that undergo multiple interactions inside the detector, the possibly-significant drift time difference of the electrons compared to the shaping time constant used may cause a significant number of the events to be counted as two small-amplitude pulses instead of being integrated into one large-amplitude pulse: this would shift some events from high channels, possibly including some from the photopeak, to low channels in the Compton continuum.

A second common explanation for the significant change in the Compton edge count rate is Compton scattering within the pressure vessel, which can have a very significant mass relative to that of the fill gas [27]. For example, in the coplanar-anode HPXe detectors the mass of the vessel and internal structures is 4.960 kg (HPXe1) and 4.670 kg (HPXe2), whereas the mass of the added gas is 330 g for detector HPXe1 and 295 g for HPXe2. If this theory is true, the spectral feature is simply the traditional backscatter peak observed in gamma-ray spectra, albeit with extreme prominence. This question will be studied in more detail in Chapter 6, but it seems that the former explanation can be discounted based upon the results of the collimation studies.

Another noteworthy property of the measured spectra is the poor energy resolution. In the Geant4 simulations of Chapter 3 several assumptions were made that simplified the simulations: foremost was the assumption of zero ballistic deficit even for very short shaping times, proven false from experimental observations. As discussed previously, the parallel noise contribution to electronic noise increases as shaping time lengthens; this can be observed in the data of Figure 4.6. Reducing the shaping time to the ideal of 6 μs could reduce the preamplifier noise contribution to peak broadening and bring the measurements closer to the simulated predictions. One way of achieving this reduction without introducing ballistic deficit problems would be to use small hydrogen admixtures to the xenon gas, which have the effect of increasing the electron drift velocity by a factor of up to 5 or more at moderate electric field intensities [48]. These energy resolution matters will be studied in greater detail in Chapters 6 and 7.

CHAPTER 5

RADIAL POSITION SENSING

5.1 Motivation for Position Sensing

The interaction position of a gamma ray within a detector is valuable information, if it can be measured. The interaction location can be used to apply pulse height corrections that counteract charge recombination and weighting potential changes as a function of position; to diagnose the detector's operating conditions, such as ensuring sufficient biasing and verifying HPXe gas purity; and to select interactions of interest within the detector. As described in Section 1.5, a handful of efforts to determine interaction coordinates in HPXe detectors have been reported in publications. These methods have focused on either using scintillation light emitted in the ionization cloud as a time stamp, or on using segmented perimeter electrodes—not necessarily the cathode—and using signal ratios from each electrode to triangulate the interaction location. While these methods work in theory, they can be challenging to employ in practice. Scintillation light collection can be difficult due to problems mating a photomultiplier tube to a high-pressure chamber, and the amount of light emitted by a gamma-ray interaction in HPXe is quite minimal. The detector capacitance for the electrode strips can be large, reducing the signal-to-noise ratio; also, it becomes necessary to process many signals concurrently, adding a great deal of complexity to data acquisition and processing.

The incorporation of coplanar anodes into HPXe ionization chambers permits a simpler position sensing method. The two anode signals can be used to give not only the position-independent signal amplitude, but also the approximate radial coordinate of the gamma-ray interaction. The method used to determine the radial position of the gamma-

ray interaction is analogous to the depth sensing technique in coplanar-anode CdZnTe detectors described in Section 2.2.4. The following sections will first introduce the theoretical framework for calculating the interaction radius as a function of anode signal amplitudes, describe detailed simulations to predict the experimental performance, then present experimental data and demonstrate the ability of radial position sensing to improve spectroscopic performance.

5.2 Coplanar Anode Position Sensing Theory

To determine the radial position of the interaction within the cylindrical detection volume, let us examine the sum of the collecting and noncollecting anode weighting potential distributions within the detector, $\varphi_{sum}(r,\theta,z)$. To proceed with an analytical solution, the following assumptions are used:

1. axial variations in $\varphi_{sum}(r,\theta,z)$ are negligible,
2. azimuthal variations in $\varphi_{sum}(r,\theta,z)$ are negligible,
3. the complex anode structure is replaced with a single cylindrical surface defined by the radius at which the actual anode wires are located.

The axial variations in the weighting potential can be considered negligible within the active volume of the HPXe detector because most of the change occurs outside the active HPXe volume, as demonstrated in Chapter 3. Assumption 2 is justified because the weighting potential boundary conditions are now $\varphi_{sum}=1$ on all anode surfaces and $\varphi_{sum}=0$ at the cathode, so the weighting potential should only have significant azimuthal variations very near the anode wires. Assumption 3 follows from the prior supposition, and is necessary to fully define the boundary of the region of interest. The governing equation is now simplified to

$$\frac{1}{r}\frac{\partial}{\partial r}\left(r\frac{\partial\varphi}{\partial r}\right)+\underbrace{\frac{1}{r^2}\frac{\partial^2\varphi}{\partial\theta^2}}_{=0}+\underbrace{\frac{\partial^2\varphi}{\partial z^2}}_{=0}=0 \tag{5.1}$$

Equation (5.1) can be solved to produce (5.2), which defines the summed anode weighting potential distribution:

$$\varphi_{sum}(r) = \frac{\ln\left(\frac{R_{cat}}{r}\right)}{\ln\left(\frac{R_{cat}}{R_{an}}\right)} \tag{5.2}$$

In this equation, R_{cat} and R_{an} denote the radii at which the cathode surface and the anode wires lie, respectively.

$\varphi_{sum}(r)$ is a function that increases monotonically between the cathode and anodes, allowing for a correlation between the anode signal and the interaction radius. However, the weighting potential is not directly measured: the net induced charge on the anodes is the known quantity, and a relationship in terms of the induced charges must be developed. The Shockley-Ramo theorem, discussed in Section 2.1, can be used to correlate the summed anode weighting potential to the sum of the induced charges on the anodes, $\Delta Q_{sum}(r)$, where the parameter q is the amount of drifting charge created in the gamma-ray interaction, and r_0 denotes the initial radius of the charge cloud in the detector:

$$\Delta Q_{sum}(r) = -q\left[\varphi_{sum}(r) - \varphi_{sum}(r_0)\right] \tag{5.3}$$

The electron charge created in the detector is approximated by $q \simeq -\Delta Q_{diff}$, which is the difference of the net collecting and noncollecting anode induced charges, and is fairly uniform throughout the detector due to proper implementation of coplanar anode design. Thus, the summed anode weighting potential can be determined as a function of the final measured amplitudes $\Delta Q_{sum}(r)$ and ΔQ_{diff} by rearranging (5.3) and assuming the electrons are fully collected at one of the anodes:

$$\varphi_{sum}\left(r_0\right) = \underbrace{\varphi_{sum}\left(R_{an}\right)}_{=1} - \frac{\Delta Q_{sum}}{\Delta Q_{diff}} \tag{5.4}$$

Equations (5.2) and (5.4) can now be equated to derive the radial coordinate of the interaction, r_0, in terms of the sum and difference of the measured anode signals, ΔQ_{sum} and ΔQ_{diff}:

$$\frac{r_0}{R_{cat}} = \left(\frac{R_{cat}}{R_{an}}\right)^{\left(\Delta Q_{sum}/\Delta Q_{diff}\right)-1} \tag{5.5}$$

As with traditional depth sensing in coplanar-anode CdZnTe detectors, this position-sensing technique relies upon a measured signal that is the product of the number of charge carriers and a function that is monotonically decreasing with radius: $\Delta Q_{sum} = -q \cdot f\left(r\right)$. The position dependence is isolated by dividing this signal by the measured anode signal difference, which is approximately equal to the number of charge carriers. Near the cathode wall, it is true that $\Delta Q_{sum} \simeq \Delta Q_{diff}$, and equation (5.5) gives the result $r_0 = R_{cat}$ (as it should). For events occurring near the anode wires, $\Delta Q_{sum} \simeq 0$, leading to $r_0 = R_{an}$, as expected. As we will see later, the only problematic region in the chamber is in the center of the anode wire structure, for in this volume $\Delta Q_{sum} \simeq 0$ and equation (5.5) predicts $r_0 = R_{an}$, introducing an error between the calculated and true interaction locations. However, the number of events occurring in this region is rather small, and due to the low electric field most events do not register properly due to severe charge recombination and ballistic deficit.

Unlike traditional depth sensing, the anode sum provides the position information, not the cathode. In theory the cathode signal could be used to obtain equivalent radial information in the HPXe detector. In practice, the use of the cathode signal is limited by the overwhelming electronic noise, a result of the large cathode-vessel capacitance—predicted to be 601 pF by the Maxwell 3D simulations.

It is important to also quantify the position resolution of the detector. To start, let us assume the anode sum and difference signal noise terms are uncorrelated, for then the error propagation formula can be used:

$$\sigma_{r_0}{}^2 = \left(\frac{\partial r_0}{\partial \Delta Q_{sum}} \right)^2 \sigma_{sum}{}^2 + \left(\frac{\partial r_0}{\partial \Delta Q_{diff}} \right)^2 \sigma_{diff}{}^2 \tag{5.6}$$

In (5.6), σ_{sum}, σ_{diff}, and σ_{r_0} are the standard deviations in the distribution of the measured ΔQ_{sum}, ΔQ_{diff}, and r_0, respectively. Using equation (5.5) it is straightforward to derive the following relationship for σ_{r_0}:

$$\frac{\sigma_{r_0}}{r_0} = \frac{\ln\left(R_{cat} \big/ R_{an} \right)}{\Delta Q_{diff}} \sqrt{\sigma_{sum}{}^2 + \left(\frac{\Delta Q_{sum}}{\Delta Q_{diff}} \right)^2 \sigma_{diff}{}^2} \tag{5.7}$$

Let us assume σ_{sum} and σ_{diff} are approximately equal. If the noise measured on each anode is independent of the other anode this is a valid assumption, since the error propagation formula applied to the sum and difference of the two raw anode signals will then yield the same uncertainty result for both σ_{sum} and σ_{diff}. Let us also convert from standard deviation to FWHM. The position resolution can now be expressed as a function of the measured energy resolution,

$$\frac{FWHM_{r_0}}{r_0} = \ln\left(\frac{R_{cat}}{R_{an}} \right) \sqrt{1 + \left(\frac{\Delta Q_{sum}}{\Delta Q_{diff}} \right)^2} \, \frac{FWHM_{diff}}{\Delta Q_{diff}} \tag{5.8}$$

Examining (5.8), the position resolution is expected to vary as a function of radius. Events occurring near the anodes will induce a summed signal $\Delta Q_{sum} \simeq 0$, so the position resolution will simply be the energy resolution multiplied by the geometrical constant. On the other hand, events near the cathode will be identified by $\Delta Q_{sum} \simeq \Delta Q_{diff}$,

so the position resolution will broaden by a factor of $\sqrt{2}$ relative to near-anode events. Assuming the measured energy resolution in the HPXe chambers is about 6% FWHM at 662 keV, and knowing $R_{cat} = 4R_{an}$, the position resolution is about 8% for events near the anodes and nearly 12% for events occurring near the cathode. This exercise shows the importance of improving the measured energy resolution as much as possible. Additionally, it is evident that the absolute position uncertainty, $FWHM_{r_0}$, is not only a function of deposited energy but also interaction location; as the interaction radius moves outward toward the cathode, $FWHM_{r_0}$ becomes larger not just due to the ratio of signals increasing, but also due to the interaction radius r_0 increasing. Thus, it is conservative to set the radial bin width according to the position uncertainty near the cathode, as the uncertainty at smaller radii will be noticeably less than this value.

5.3 Simulations

It is important to simulate the detector response as accurately as possible to predict the performance of the HPXe chambers. These simulations are more sophisticated than those used during the design phase to optimize the anode structure, relying upon several different modules to create an accurate representation of the experiment. The detector simulations incorporate Monte Carlo methods with electrostatic simulations and knowledge of fundamental HPXe gas properties to create the best possible model of the detector response. These physical processes are included in the simulations:

- stochastic particle transport;
- energy deposition via Compton, photoelectric, and pair production processes;
- Fano statistics;
- electron cloud distribution;
- charge recombination along delta-ray tracks;
- electron transport along the established field lines;
- summed and subtracted preamplifier signal generation as a function of time;
- Gaussian filtering of the preamplifier signals;
- superposition of responses for multiple-site events;

- sampling from a realistic (experimentally measured) system noise term; and
- calculation of signal amplitudes and the corresponding event energy and radius.

These processes were divided among three different computer codes: Maxwell 3D to solve the electrostatic fields; a Matlab [95] program developed to simulate the measured shaped signal as a function of starting position within the detector, given the HPXe density and biasing conditions; and Geant4 to perform particle transport and calculate the measured spectra given the energy deposition sequence for each gamma ray's history.

It is worth noting that this computational effort seems to be the most detailed study of HPXe ionization chamber performance, based upon information in the open literature. Smith, McKigney, and Beyerle attempted similar modeling using Geant4 to generate ionization densities and locations, they then simulated transport of the electrons in each event to an unshielded anode in a cylindrical configuration [55]. This particular model did not include charge recombination, assumed the electric field was a function of radius only, did not implement a shaping filter, and assumed zero electronic noise. The results were not particularly accurate, reflecting the simplified modeling.

5.3.1 Maxwell 3D Electrostatic Simulations

The Maxwell 3D electrostatic solver has been used to simulate the operating electric field and weighting potential distributions within the detection volume. The modeled geometry is as accurate as possible, incorporating the pressure vessel, all Macor insulating components, the anode wires, and the cathode surface. The results of these electrostatic simulations have been written to output files, listing the electric field and weighting potential at each node on a grid of spacing (0.2 mm, 0.2 mm, 10.0 mm). The grid spacing in the axial direction can be courser because of the more gradual changes in the weighting potential and electric field along the axial direction. The spacing in the x- and y-directions has been chosen to provide sufficient accuracy. By using the actual Maxwell 3D simulation results, the exercise of finding an accurate Fourier series representation of the fields is rendered unnecessary; in addition, conditions in the end volumes where axial changes are non-negligible can be considered in this method.

5.3.2 Matlab Waveform Generation Code

The Maxwell 3D results have been used, along with electron-ion recombination, the electron drift velocity, and electron cloud dimensions to simulate preamplifier waveforms in a custom Matlab code. These preamplifier signals are shaped using a Gaussian filter, and the final shaped waveform is saved to a file. The idea behind this program is that simulated waveforms can be generated for each initial interaction point on a pre-defined grid; the signals are generated using user-defined time steps. After completion, the output file contains the simulated waveform at every time step for each starting location, which can be used by Geant4 to more accurately predict the measured signals for each gamma-ray event. A grid of starting points with grid spacing (0.5 cm, 0.5 cm, 10.0 cm) is fine enough to properly estimate measured pulse heights without creating unnecessarily-large data files. A sufficient time step to ensure smooth trajectories near the anode wires is 100 ns.

Electron-ion recombination information is from Bolotnikov and Ramsey [96], who measured the fraction of charge extracted from an ionization cloud for different combinations of gamma-ray energies, HPXe densities, and electric field magnitudes. Equation (5.9) fits the published data for ^{137}Cs photoelectric absorptions in HPXe gas of density 0.3 g/cm^3; the electric field magnitude E has units [kV/cm]:

$$\frac{Q}{Q_0} = \frac{1}{4.65\left(0.228 - 0.016\log E\right)} \tag{5.9}$$

The electron cloud is assumed to be a sphere of diameter 3.65 mm, which is the mean diameter calculated using Geant4 simulations for a 662-keV photoelectron in 0.3 g/cm^3 HPXe gas [97]. In these simulations, monoenergetic photoelectrons are directed randomly into the Xe gas: as they create ionizations, the position of each interaction is compared to previous coordinate maxima and minima, and these extrema are updated if necessary. The electrons are tracked until their mean free path reaches a user-defined value of 1 μm. The impact of this cut value was studied by decreasing it to 0.1 then 0.01 μm, but the resulting cloud distribution did not change. The results of this cloud diameter calculation are presented in Figure 5.1.

The true electron cloud dimension will generally be smaller when less energy is deposited in an interaction, but for the simulations only a single cloud diameter is used. This assumption should slightly worsen the results in comparison to the experiment, as electron arrival at the collecting anode will appear more dispersed in time, leading to greater pulse height deficit. Generally a minimum of 500 electrons are dispersed randomly throughout the cloud to transport through the detector for signal generation purposes. This number was found to reduce the error arising from fluctuations in the final induced charge to well below 1%.

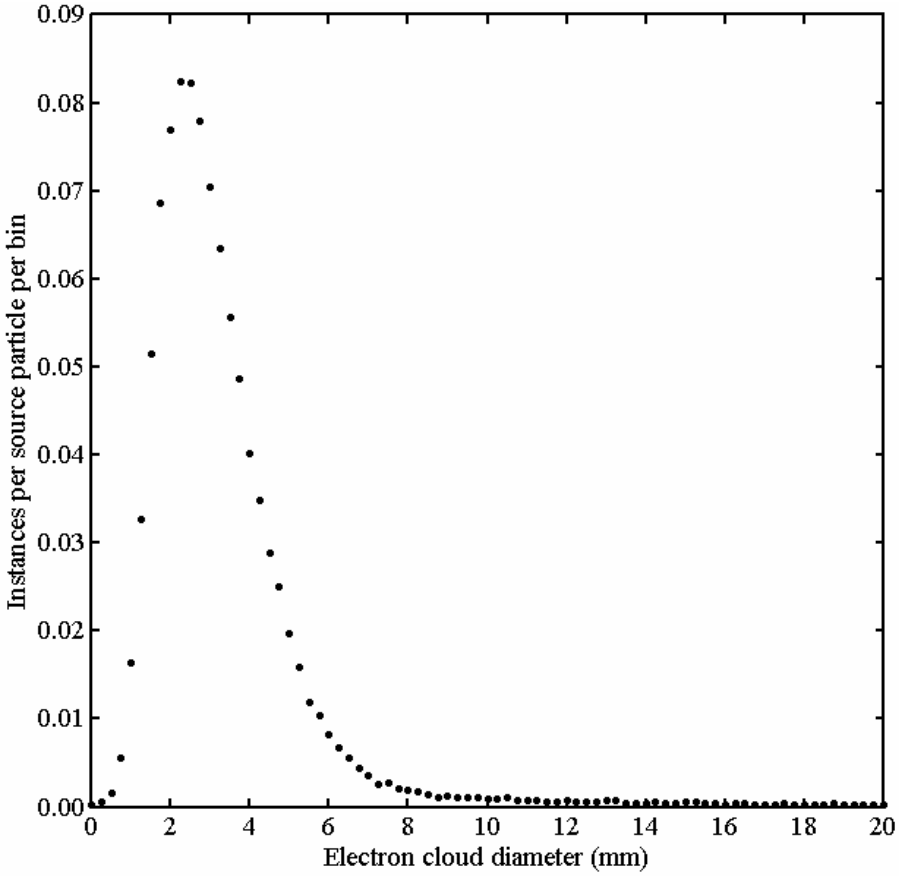

Figure 5.1. Geant4 simulated distribution of the charge cloud diameter in the HPXe detector for 662-keV depositions.

Based on the electron drift speed data published for HPXe at density 0.6 g/cm^3 by Ulin et al. [48], the following simple relationship is used in the simulations to determine the drift speed at each time step:

$$v_e = \begin{cases} E\left[\frac{kV}{cm}\right]\frac{mm}{\mu s}; & E < 1.0\frac{kV}{cm} \\ 1.0\frac{mm}{\mu s}; & E \geq 1.0\frac{kV}{cm} \end{cases} \tag{5.10}$$

When consulting published drift speed data, it is important to realize that the drift speed is a function of E/N, where N is the atom density of the gas [98]. Thus, since the coplanar-anode HPXe chamber has gas density 0.3 g/cm^3, a particular drift speed is realized at half the published field strength in the current chamber.

When an event is generated within the detector, preamplifier sum and difference waveforms are calculated at each time step over the duration of the pulse length, with the position of each electron being updated at each point in time given the local electron drift velocity. The final preamplifier signals are calculated by multiplying the signal at each point in time by the fraction of electrons escaping recombination, then dividing by the total number of electrons in the cloud. The final preamplifier pulse is thus normalized to a value of 1.

To simulate the presence of a Gaussian shaping amplifier, a $CR-(RC)^4$ filter is implemented; this filter has been chosen because it closely approximates a true Gaussian distribution [8]. The impulse response function $h(t)$ used to achieve this filter is given by the following equation, where n is the number of RC integration stages in the filter and $\tau_s = RC$ is the shaping time:

$$h(t) = \frac{1}{n^n \tau_s}\left(\frac{t}{\tau_s}\right)^n \mathrm{e}^{\,n-\frac{t}{\tau_s}}\left(\frac{n\tau_s}{t}-1\right) \tag{5.11}$$

The convolution of this filter with a preamplifier waveform $w(t)$ produces a Gaussian-shaped pulse. First the Fourier transform is used to calculate the frequency response of both the signal and the filter, which is easy because the Fourier transform and its inverse are built-in functions in Matlab. Denoting the Fourier transform of the shaping filter and preamplifier waveform as

$$H(\omega) \equiv \mathcal{F}\{h(t)\} = \int_{-\infty}^{\infty} h(t) e^{-i\omega t}\, dt$$
$$W(\omega) \equiv \mathcal{F}\{w(t)\} = \int_{-\infty}^{\infty} w(t) e^{-i\omega t}\, dt \tag{5.12}$$

the definition of convolution and the properties of the Fourier transform [82] are used to calculate the shaped filter output, $S(t)$.

$$\begin{aligned} S(t) &\equiv \int_{-\infty}^{\infty} w(\tau) h(t-\tau)\, d\tau \\ &= \mathcal{F}^{-1}\{W(\omega) H(\omega)\} \end{aligned} \tag{5.13}$$

The shaped waveform is written to a data file as a function of time; all of the waveforms generated for each of the preamplifier sum and difference signals are contained in these data files, along with the corresponding interaction location.

5.3.3 Geant4 Monte Carlo Simulations

The waveform simulations are combined with Geant4 Monte Carlo simulations to provide the most detailed model of detector response achievable. In these simulations, the physical geometry is represented as accurately as possible, and gamma rays are emitted from a ^{137}Cs point source located on a plane bisecting the detector, 25.4 cm from the vessel wall. In the code, energy depositions within the sensitive volume of the detector trigger a sequence of calculations that first records the location and energy deposited for the interaction. To introduce Fano statistics, the number of charge carriers produced in the interaction, N, is sampled from a normal distribution characterized by mean and standard deviation

$$\begin{aligned} \bar{N} &= \frac{E_{dep}}{w} \\ \sigma_N &= \sqrt{F\bar{N}} \end{aligned} \tag{5.14}$$

where E_{dep} is the energy deposited in the interaction by the gamma ray, w is the mean energy required to create an ionization, and F is the Fano factor. For these simulations, $w = 21.9\,\text{eV}$ and $F = 0.17$ [35].

The interaction location is mapped to the closest node for which a response was generated in the Matlab waveform program. This can involve reflections and translations through the detector geometry, possible due to the symmetry of the design. After each gamma ray history is complete, the shaped added and subtracted waveforms for each interaction location are scaled by the number of electrons generated in the corresponding interaction, and then summation over all interaction locations is executed to create a single shaped response for both the added and subtracted signals. Superposition is possible due to the linearity of the filter and the Fourier transforms. From these waveforms, the maximum amplitude of the added and subtracted waveforms can be determined; these values are necessary to form the energy spectrum and to calculate the event radius.

Finally, electronic noise is added to the system by separately sampling from a normal distribution to determine the collecting and noncollecting anode noise terms. (This is only valid if there is no correlation in the experimental noise terms.) The normal distributions are characterized by a mean of 0 and a standard deviation that is shaping-time dependent, estimated from the measured equivalent noise charge data of Section 4.2.2. The noise-perturbed signal amplitudes are used to generate the measured deposited energy and the calculated radius via equation (5.5). Energy and radially-separated energy spectra are generated by placing each event into 1-keV wide energy bins and dividing the continuum of radial values into 10 bins, which corresponds to the position uncertainty calculated using equation (5.8).

5.3.4 Simulation Results

The purpose of the first set of simulations is to determine an appropriate shaping time for a given set of detector biases: -4000 V on the cathode, +1400 V on the collecting anode, and the noncollecting anode at ground potential. This detector biasing scheme is typical for experiments, and therefore very relevant. To begin, make the following assumptions to simplify this set of computations:

- the electron cloud has zero diameter;
- there is no axial variation in the operating or weighting fields;
- all interactions are via photoelectric interactions;
- all events create exactly N_0 electrons (i.e., $F = 0$); and
- there is no electronic noise.

Given these assumptions, shaping times of 6, 10, 16, 20, and 32 μs have been modeled. The first three shaping times are all experimentally realizable on the current laboratory equipment; the final time constants are useful to determine the spectrum shape without ballistic deficit concerns. Events were generated throughout the interaction plane on a uniformly-spaced grid, and the simulated signals recorded to form a differential pulse-height spectrum.

Figure 5.2 shows the photopeak region of the simulated spectra, assuming the incoming gamma rays have energy 662 keV; in this plot, the data series are separated for clarity by vertical shifts. It is evident from this figure that the cases with 6 and 10 μs shaping time constants suffer severe degradation in the photopeak due to ballistic deficit. The 20 and 32 μs time constants seem to be sufficient for avoiding ballistic deficit broadening. The minor peak near channel 580 in each data series is an artifact of the weighting potential discretization; several events near the center of the detector are assigned similar initial weighting potentials.

Figure 5.3 is a scatter plot which displays the interaction radius calculated with equation (5.5) against the true interaction radius for each event. As the shaping time constant is increased from 6 to 32 μs, there are two beneficial effects: first, the calculated radius becomes a better representation of the true radius for near-cathode events; second, the distribution in calculated radii for a particular true interaction radius becomes narrower. The combination of these two effects allows a more accurate measurement of the interaction radius. The reason for this effect is, once again, ballistic deficit at short shaping times, since the rise time of the summed signal for a near-cathode event can be near 40 μs. When short time constants are used, the summed signal's shaped amplitude is decreased and the exact path of the electron cloud becomes more important, giving rise to the wider distribution of calculated radii for a fixed interaction radius. Even for the

longest shaping time, the measured radius does not reach 1.0 for a near-cathode event—this is not a problem, since as long as the calculated radius increases monotonically with the true radius, a correlation can be made.

In Figure 5.3 there is a plateau at a calculated radius of about 0.04. Due to the nature of the summed anode signal's weighting potential, events occurring anywhere within the anode structure will always have nearly uniform summed anode responses. In addition, near the anodes, which are centered at radius 12.7 mm, there is a fairly large variation in calculated radii due to the dramatic change in the anode weighting potential difference, which varies from -1 to +1 between the noncollecting and collecting anode wires, respectively.

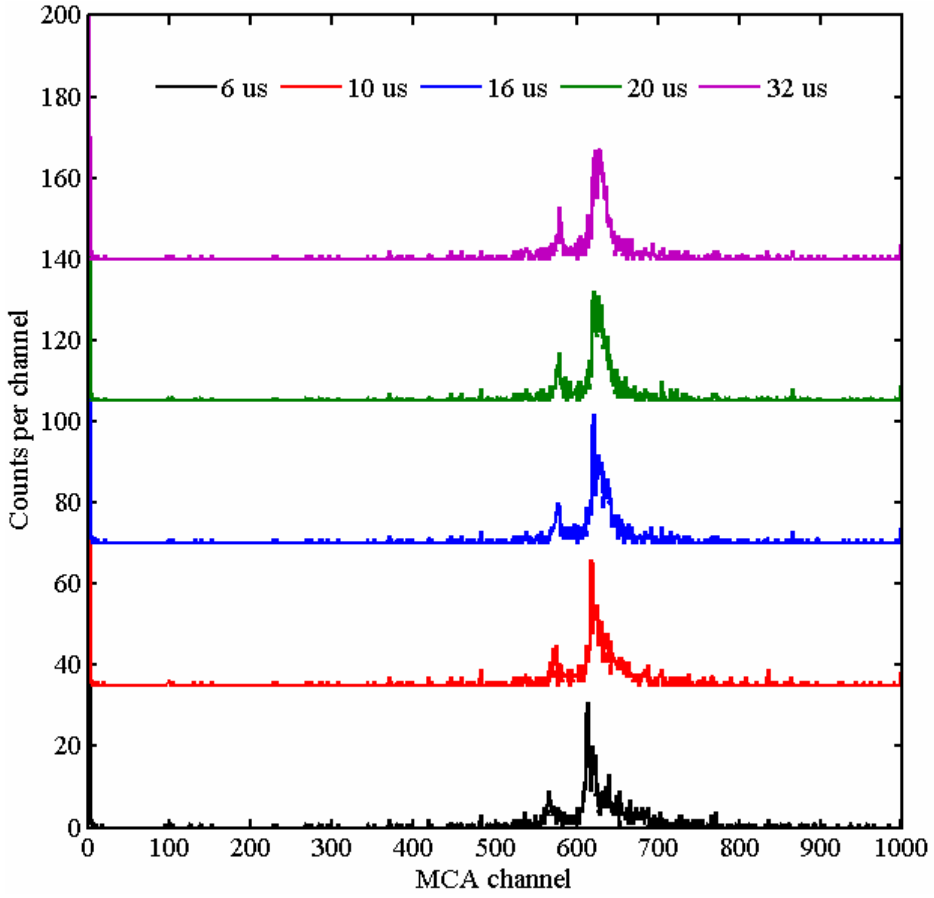

Figure 5.2. Simulated effect of shaping time choice on the photopeak region. Vertical offsets are used to separate the data.

From the figures, it seems that a minimum shaping time of 20 μs should be used to improve both energy and position resolution. In practice, the energy resolution will also be affected to some degree by the inclusion of all of the assumptions listed at the beginning of the section; electronic noise will certainly play a major role, favoring shorter shaping times than 20 μs. (For example, in Chapter 4 the best energy resolution was measured using a 12 μs time constant.) The best course of action may be to choose two shaping time constants: the preamplifier difference signal will be shaped with a filter that minimizes photopeak width, while the preamplifier sum signal is shaped with a longer shaping time that minimizes ballistic deficit.

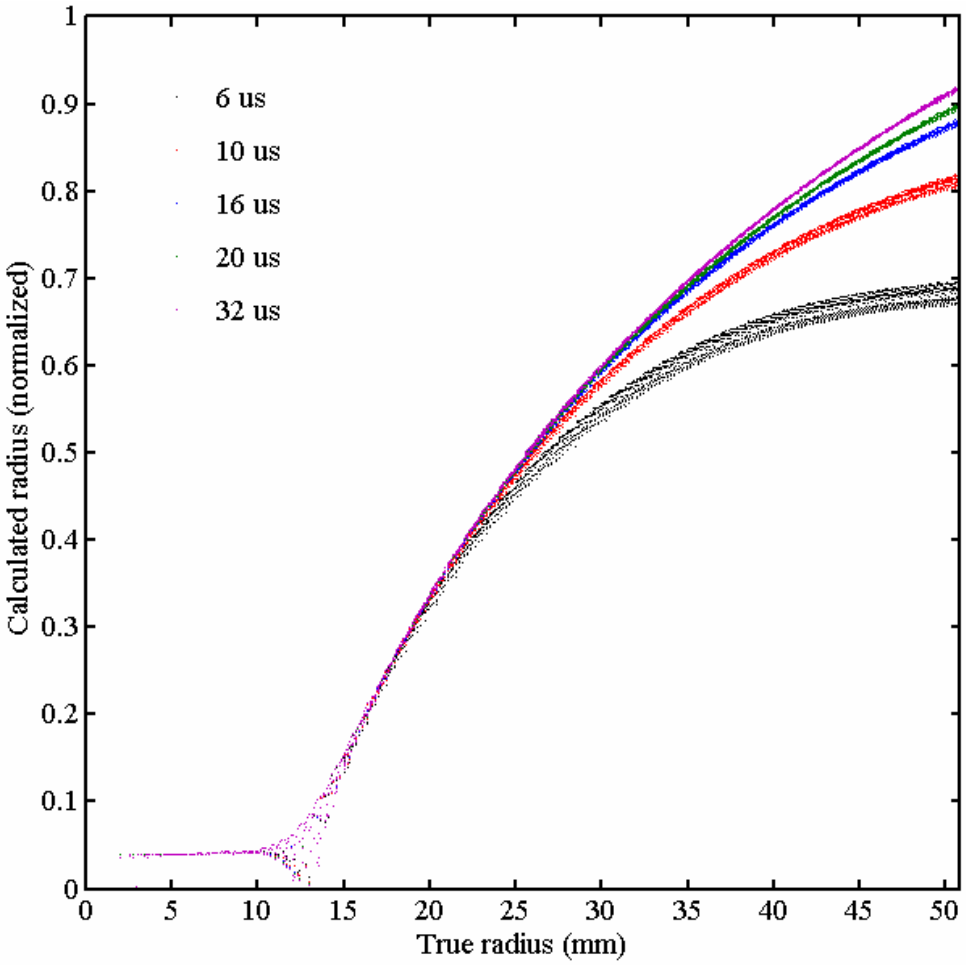

Figure 5.3. The calculated interaction radius plotted against the true interaction radius for several shaping time constants. (Longer shaping times correspond to greater calculated radii.)

Let us continue with shaping time constants of 20 μs for the anode sum and difference signals. It is time to consider a simulation that uses realistic approximations at all physical parameters of significance. The assumptions made at the beginning of this section have been replaced with the following:

- the electron cloud has diameter 3.65 mm;
- axial variation in the operating and weighting fields is accounted for by putting each interaction into one of five axial slices to calculate the detector response (3 slices in the central region centered at z = 0, 25, and 50 mm; 2 slices in the end region centered at z = 68 and 78 mm);
- interactions can be photoelectric absorptions, Compton scatters, or pair production as dictated by Geant4's cross-section library;
- a Fano factor $F = 0.17$ is used to simulate statistical broadening; and
- electronic noise is extrapolated from experimental data to an approximate value of $ENC = 450\,\text{electrons}$ for the total system noise.

The simulation results are presented below. To obtain good statistics, the Geant4 run considered $20\text{x}10^6$ 662-keV photons emitted from a point source located 25.4 cm from the outer wall of the vessel and centered axially. The energy spectrum is plotted in Figure 5.5, and is labeled the raw spectrum. The measured energy resolution of this spectrum is 4.6% FWHM.

It is possible to use the radial sensing technique to plot the simulated energy spectrum as a function of radius, as done in Figure 5.4 with 10 radial bins spanning the physically-meaningful range of calculated radii, one for negative calculated radii, and one for calculated radii that are too large to be correct. There are several important features in this spectrum:

1. There is basically no response at calculated radial bins 0, 1, and 2. These radii physically lie inside the anode structure, and events in this volume are shifted to larger radii (see Figure 5.3).

2. As the radius increases, the photopeak exhibits improved energy resolution, with dramatic changes occurring in radii 3-5 (near the anode wires). This is attributed to weighting potential nonuniformity in the immediate area.
3. As the radius increases, the integral number of counts measured also increases, as expected in a cylindrical geometry. The maximum number of counts appears in radial bin 8; consulting Figure 5.3, this can be explained because bin 8 is the largest bin for which the full range of calculated radii can be achieved.
4. Radial bin 11 contains mainly low-energy events, but no classic gamma-ray spectral features. This is because the radius lies physically outside the chamber; it corresponds to events with the anode signal sum larger than the difference, which happens mainly when electrons are improperly collected at the noncollecting anode, thereby reducing the anode difference signal but not the sum.
5. Although it is difficult to see in this plot, the photopeak centroid channel varies slightly as a function of radial bin. This is due to variations in ionization cloud charge recombination at large radii; at small radii, the nonzero weighting potential is a significant contributor.

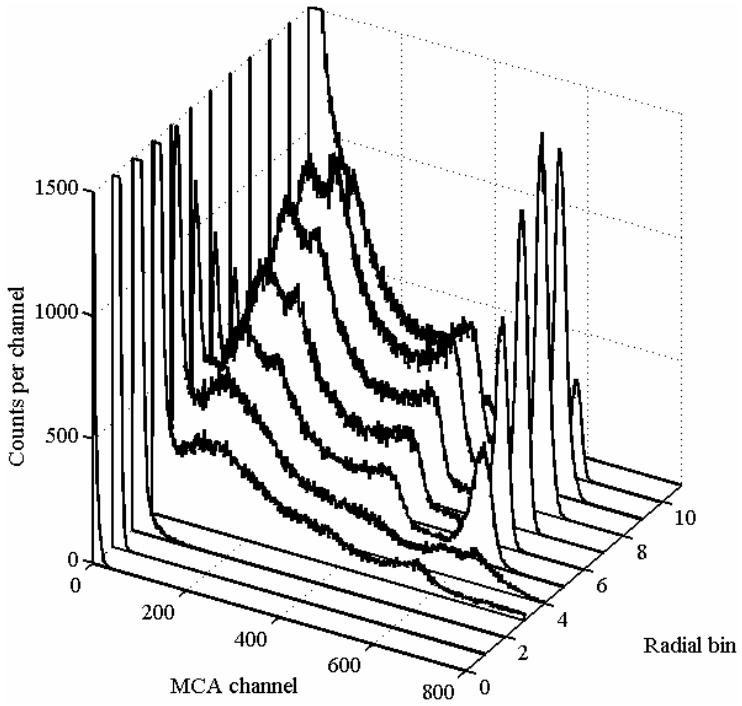

Figure 5.4. The radially-separated energy spectrum for the ^{137}Cs simulation. Radial bin 0 theoretically corresponds to the center of the chamber, and radius 10 is at the cathode.

Some of these observations can be used to improve the quality of the measurements. For example, events recorded in radii that are physically meaningless can be neglected because they are a result of improper charge collection. In addition, events in radii 3 and 4 can be neglected because the energy resolution is very poor in these regions of the detector. For the remaining radii, a radial bin-dependent gain can be applied to align all photopeak centroids in the same channel (arbitrarily chosen as channel 662). The results of these corrections to the raw data are demonstrated in Figure 5.5. In the figure, it is evident that the ratio of photopeak to Compton continuum counts is noticeably improved, and the measured energy resolution improves from 4.6% to 4.4% FWHM at 662 keV. These enhancements are useful for standard spectroscopic measurements.

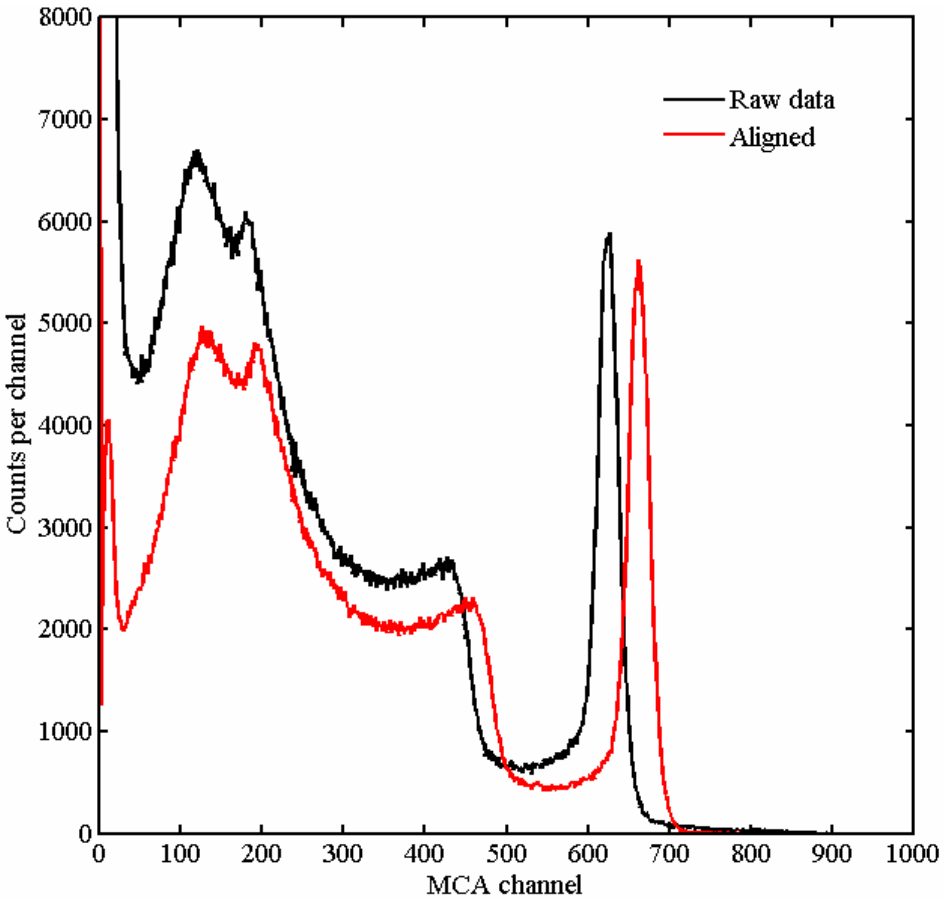

Figure 5.5. The effect of radial corrections on the simulated ^{137}Cs energy spectrum. The energy resolution of the photopeak is improved from 4.6% to 4.4% FWHM.

5.4 Experiments

To perform radial position sensing, both the sum and difference of the collecting and noncollecting anodes are required. These signals are generated using simple addition and subtraction circuits included in the preamplifier shielding box; the output of each circuit is filtered using a shaping amplifier, and these shaped pulses are sent to a peak-hold circuit, where the maximum amplitudes of both signals are held for a fixed period of time after the circuit is triggered. The peak-hold circuit generates a trigger that signals the data collection system to sample the peaks before they are discharged. The data collection is performed via a LabVIEW [99] program recording data from a PCI-6110 data acquisition card. A schematic of this system is shown in Figure 5.6.

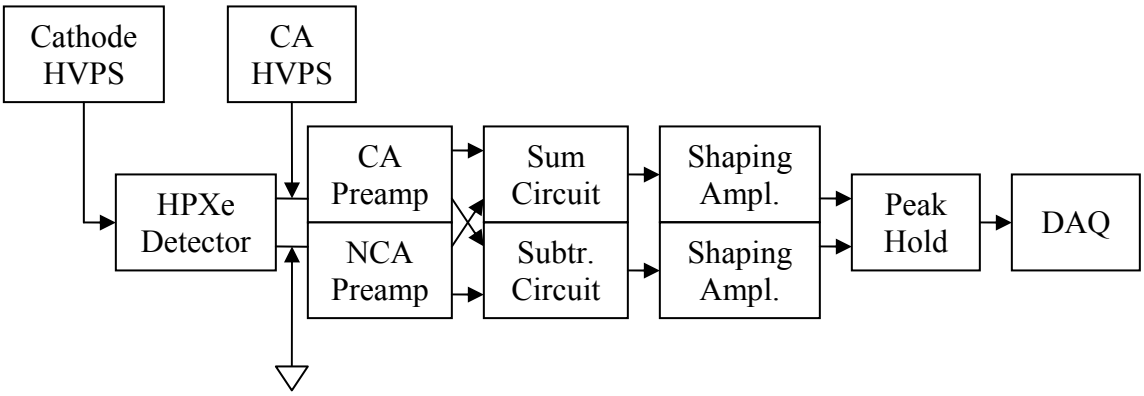

Figure 5.6. A connection diagram of the detection system used for radial position sensing measurements.

The data acquisition system digitizes the incoming signals with 12-bit accuracy, thereby partitioning the incoming signals spanning a range of ±10 V into 4096 channels [100]. The shaped anode sum and difference amplitudes are written to a data file, each row representing a recorded event. The data post-processing is accomplished using Matlab.

Using the HPXe optimization study presented in Chapter 4 as a reference, data was collected using the following system parameters: the cathode and collecting anode were biased at -4500 V and +1400 V, respectively; a ^{137}Cs source was collimated to direct source photons to the central plane of the detector; the subtracted signal was filtered using triangular shaping with a 12 μs shaping time constant; and a counting time

of 1800 s was used, with background counted alone for an equivalent time. The summed signal was shaped with a Gaussian filter using the longest available shaping time—16 μs—in order to minimize ballistic deficit.

The data is presented as a function of radius in Figure 5.7 and Figure 5.8. In these plots, the radius refers not to the theoretical radius calculated using equation (5.5), but instead to the ratio of the measured signal amplitudes of the anode sum and difference signals, ξ:

$$\xi = \frac{\Delta Q_{sum}}{\Delta Q_{diff}}$$
$$FWHM_{\xi} = \sqrt{1+\left(\frac{\Delta Q_{sum}}{\Delta Q_{diff}}\right)^2}\ \frac{FWHM_{diff}}{\Delta Q_{diff}} \tag{5.15}$$

This expression is sometimes more convenient to work with because the FWHM in the distribution of ξ measured for a particular energy is slowly varying with respect to radius, whereas in equation (5.8) the position resolution is slowly varying, meaning the absolute width of the bins can change quite a lot between the anode and the cathode. Assuming the energy resolution is around 6%, $FWHM_{\xi} \in [0.060, 0.085]$. The induced charge ratio is physically expected to span the range $\xi \in [0,1]$, so 10 bins spanning this range is an appropriate number given the limitations on resolution. Figure 5.7 shows the data including source counts along with background and a test pulse; in Figure 5.8 the background has been stripped out. When comparing these two plots it is evident that background events occur mainly at low energies, and are fairly evenly distributed throughout the entire chamber.

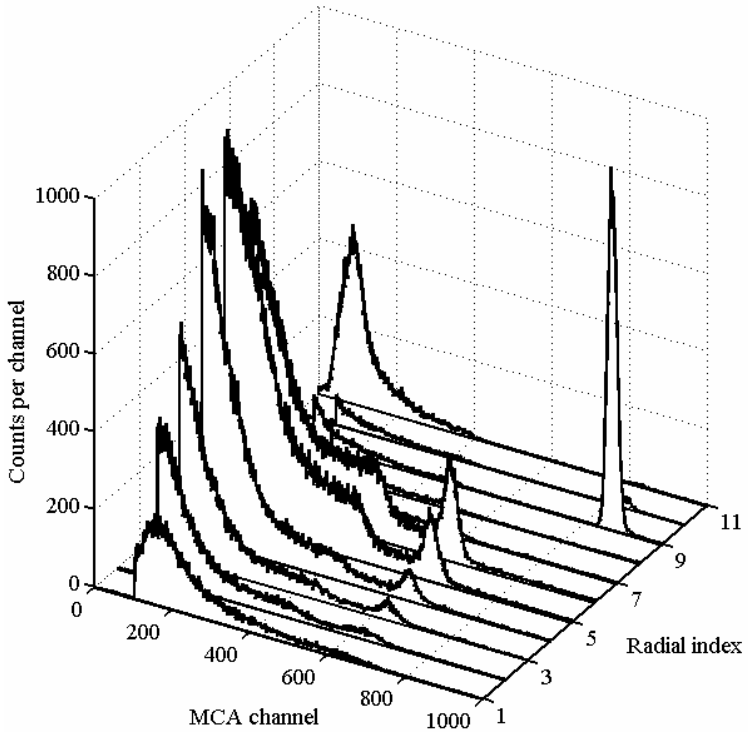

Figure 5.7. A radially-separated experimental ^{137}Cs energy spectrum. The radial index is simply the anode sum-difference ratio in this plot. Increasing indices correspond to increasing physical radii. A test pulse is present in radial index 9 near channel 850.

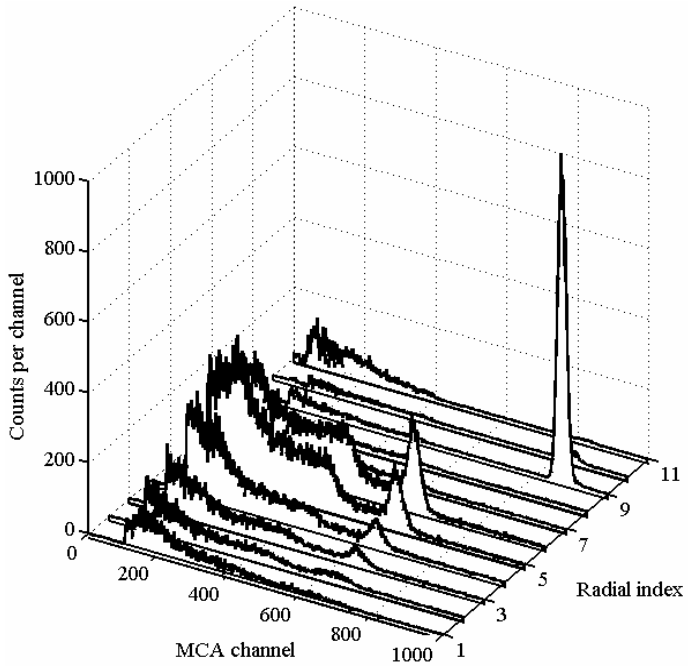

Figure 5.8. An experimental ^{137}Cs radially-separated spectrum with background stripped out, but otherwise identical to Figure 5.7.

Examining Figure 5.8, effects are observed that are similar to the simulation results presented in Figure 5.4, with a few notable exceptions: there are not empty small radial bins, which is due to the difference in the radius calculation method; many of the large radial bins are nearly empty, a ballistic deficit effect caused by relatively short shaping time constants compared to the summed signal rise times; and the final difference is the inclusion of a test signal which shows as a peak near channel 850 in radial bin 9. The experimental data does exhibit very broad or nonexistent photopeaks at small radii, just as the simulations predicted: this effect is due to poor weighting potential uniformity near the anodes. As the radius increases, so does the integral number of counts, which is consistent with the cylindrical geometry. Radial bin 11 contains only low-energy counts, also predicted by the simulations, resulting from improper charge collection. In addition, it is true that the photopeak centroid shifts slightly as a function of radial index, due to changes in the weighting potential distribution and charge recombination.

Let us consider using the radial information to improve the energy spectrum, as was done with the simulations. First, let us discard data from radii that do not contain discernable photopeaks, as these channels only degrade the spectrum. This leaves only radii 3 through 6 as desirable data. Now, apply a gain to each radial bin that aligns each centroid at channel 662, an operation which reverses the drift in photopeak centroid as a function of radius. After re-processing the data to filter out the unwanted events and apply an appropriate gain to the remaining data, the overall energy spectrum is noticeably improved. The new spectrum is presented in Figure 5.9 along with the original data for comparison. The measured energy resolution improved from 5.9% to 5.5% FWHM at 662 keV, which is a statistically-significant improvement considering the uncertainty in each resolution measurement is calculated to be about 0.03% [8]. In addition, it is obvious that the photopeak-to-total count ratio is greatly increased. The measured noise limit is 4.2% FWHM, which when subtracted in quadrature gives an intrinsic detector resolution of 3.6% FWHM. This value is much greater than the resolution limit predicted by Fano statistics, and will be analyzed in Chapter 6 for sources of degradation and possible improvements.

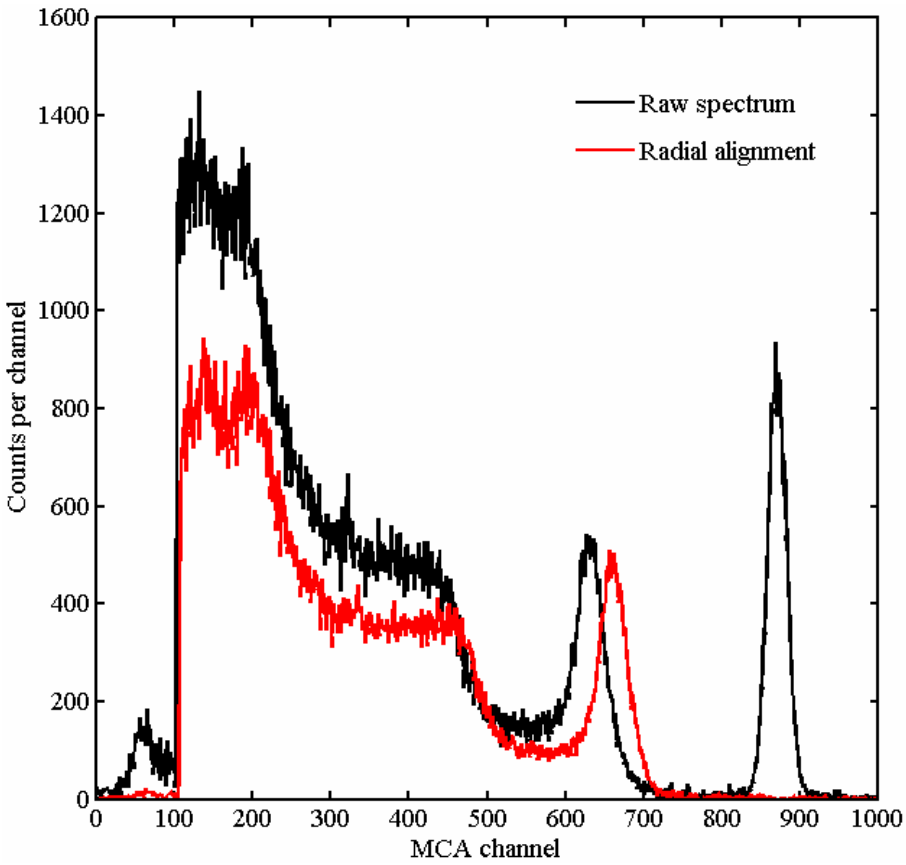

Figure 5.9. The effect of radial corrections on the experimental ^{137}Cs data. The photopeak resolution improved from 5.9% to 5.5% FWHM as a result of the corrections.

CHAPTER 6

CONSIDERATIONS FOR IMPROVING PERFORMANCE

6.1 Energy Resolution Enhancement

Previous chapters have demonstrated performance of the coplanar-anode HPXe detectors as good as 5.5% FWHM for a collimated ^{137}Cs source. This represents a significant advancement compared to previous coplanar-anode HPXe designs, which achieved just 9% FWHM at 662 keV [60]. Nevertheless, to become a viable alternative to gridded HPXe chambers the energy resolution must improve to between 3.5 and 4% FWHM, which represents common performance for a large-diameter gridded chamber. The purpose of this chapter is to investigate physical processes important in signal formation, quantifying the contribution of each process to the overall measured peak width. This study will suggest how improvements can be made, and at the same time limits on performance improvement may become apparent.

6.1.1 Simulation Methods for Physical Process Contributions

One of the nice features of the Maxwell 3D/Matlab/Geant4 simulation package described in Chapter 5 is that it lends itself to quantifying the effect of each physical process upon the measured photopeak width. Since physical processes are introduced one-by-one, the desired results are obtained by creating tallies of the measured pulse amplitudes after each physical process is added to the model. By creating several energy spectra in this manner, it is possible to quantify the effect of each physical process by comparing the photopeak FWHM before and after each step of physics implementation. Starting from the true energy deposition spectrum, the physical processes that are quantified are

- Fano charge carrier statistics,
- weighting potential distribution at the interaction location,
- charge recombination at the ionization site,
- nonzero electron cloud radius,
- improper electron collection due to insufficient anode biasing,
- pulse shaping,
- electronic noise, and
- axial field nonuniformities.

The effects of pulse shaping are split into two parts: a geometrical portion and a contribution due to timing. The geometrical factor considers the slightly different shaped amplitudes resulting from interactions in different sections of the detection volume. These differences arise mainly from the variations in the subtraction circuit pulse shape. The timing factor acknowledges that due to the potentially long drift time of electrons in this system, a multiple-interaction event can suffer from pulse-height deficit. This deficit arises because the response of the shaping filter peaks at different times for the different charge clouds created in the detector, and the time offset means the measured pulse amplitude is slightly less than the sum of the responses when each cloud is considered individually. Figure 6.1 demonstrates this effect using simulated data and a $CR-(RC)^4$ shaping filter with a 12-μs time constant. The response to single-site events creating a single electron at (18 mm, 0, 0) and (48 mm, 9.5 mm, 0) are shown in black and blue, respectively. The response for a two-site event creating a single electron at each of these two locations is shown in red. In this case, 2 units of charge are created; the amplitudes of the filter response to each drifting electron are 0.9948 and 0.8812, the deviations from unity caused mostly by weighting potential. Thus, the ideal measured amplitude would be 1.8760 units of charge, but in fact the time delay causes the true two-site event to have a measured amplitude of 1.5046 units of charge, a deviation of 19.8%.

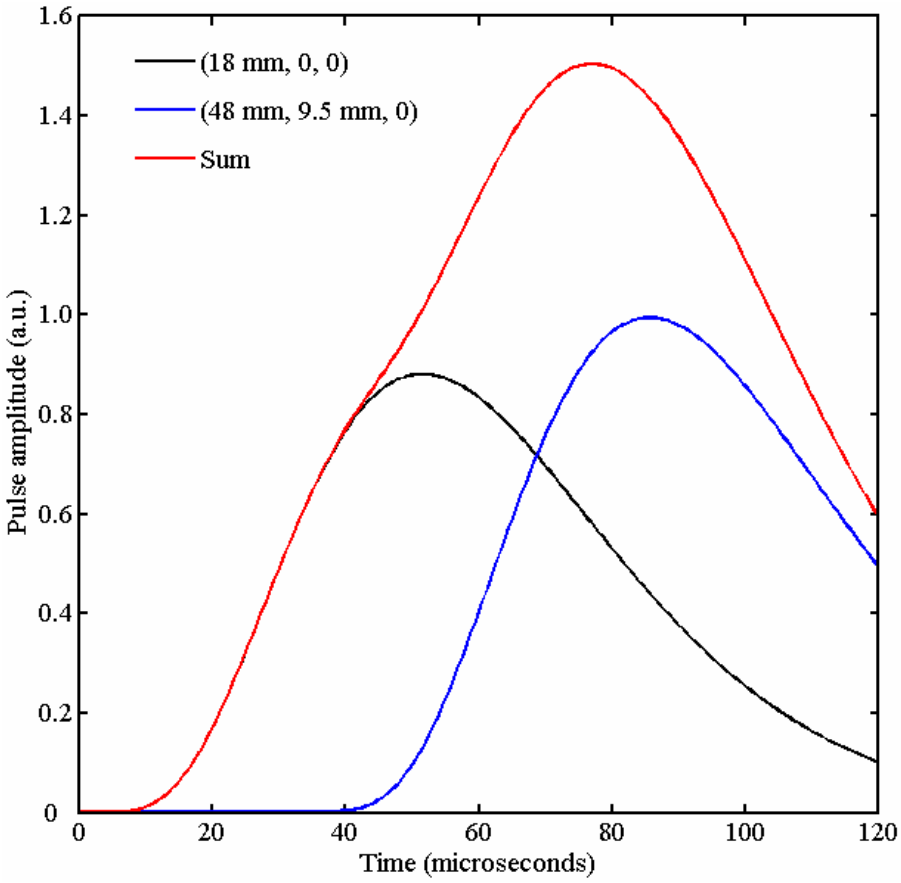

Figure 6.1. The response of the shaping filter to events at (18 mm, 0, 0) and (48 mm, 15 mm, 0) are shown in black and blue, respectively. The response to a two-site event is shown in red and suffers from pulse height deficit.

Some inaccuracies in the results are expected due to limitations of the current simulation package. For example, the electron cloud is not treated stochastically, but instead a single fixed cloud distribution is used at each interaction location. This approximation will reduce the observed variance in the simulation results. In addition, discretization of the continuous weighting potential and electric field distributions may introduce some inaccuracies, although if the discretization is fine enough this error term may be negligible. Finally, processes such as ion drift and charge diffusion are not modeled currently, while the model used for charge recombination statistics is only assumed to be correct. Positive ions are expected to have a negligible effect on the measured signals—after all, coplanar anodes are supposed to remove sensitivity to ion motion—but electron diffusion is an important term that can affect charge collection

times and the fraction of the generated electrons terminating their paths at the noncollecting anode. Recombination statistics are considered to be Poisson in nature, which assumes that individual recombination events are independent of one another and each have small probability of occurring. Although the simulation package will not be revised, it is important to recognize the limitations of the model.

6.1.2 Spectral Contributions in Pure Xe with a 20 μs Shaping Time

Let us first consider the case with ideal shaping times in pure Xe gas, as determined by the simulation results in Figures 5.2 and 5.3. In this instance, the ideal shaping times are defined to be those which minimize ballistic deficit problems, and the simulations showed 20 μs shaping time constants to be sufficient for both the anode sum and difference signals. The parameters of interest in this simulation are listed in Table 6.1.

Table 6.1. A list of important parameters in the energy resolution study.

Parameter	*Value*
Gas density	0.3 g/cm^3
Cathode/collecting anode bias	-4000 V / +1400 V
Electrons per cloud	600
Electron cloud diameter	3.65 mm
Simulation mesh spacing	(0.5 mm, 0.5 mm, 25.0 mm)
Shaping time constants	20 μs
Shaping filter	$CR-(RC)^4$
Waveform time step	100 ns
Simulated source	^{137}Cs point source
Number of Geant4 primary particles	20x10^6
Mean ionization energy	21.9 eV
Fano factor	0.17
ENC (extrapolated from measured data)	450 electrons

The results of these simulations follow. Let us begin with three spectra that cannot be changed with bias or shaping time: the true energy deposition spectrum, and then this spectrum broadened first by Fano carrier statistics and then by the weighting potential distribution at the gamma-ray interaction locations. Furthermore, the results will be idealized at this stage by considering only two-dimensional fields—$\varphi_{wp}(r,\theta)$ and $\boldsymbol{E}(r,\theta)$—with no variation in the axial direction. These spectra are shown in Figure 6.2, with the left panel showing the entire spectrum and the right zooming in on the photopeak region. It is evident that the two physical processes broadening the true deposition account for very little photopeak broadening.

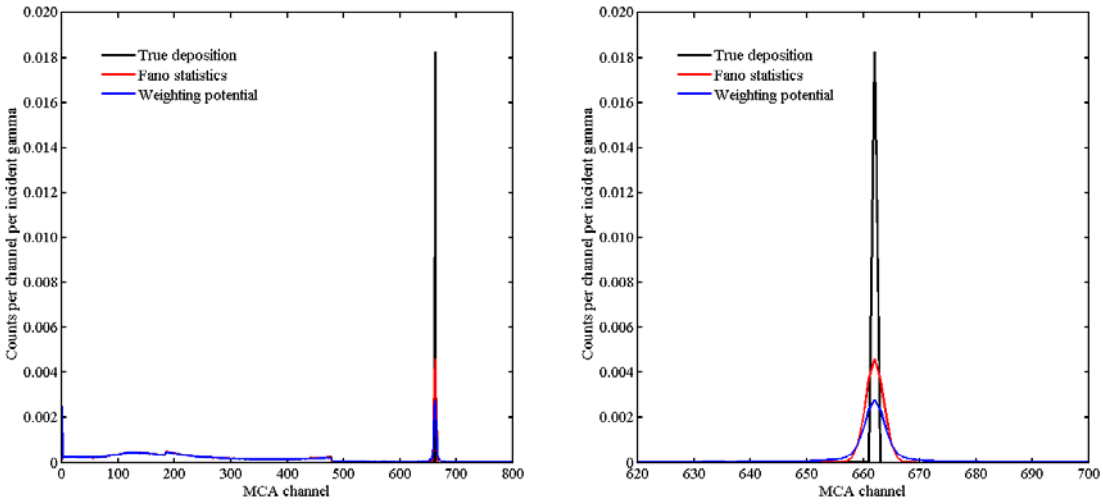

Figure 6.2. A comparison of the true deposited energy spectrum to the spectrum broadened by Fano carrier statistics, then by the weighting potential distribution at the interaction location.

Let us now consider the effects of charge recombination, electron cloud dimension, and the effects of nonideal anode biasing upon electron collection. For ease of comparison to previous results, the final tally from Figure 6.2 is carried over to Figure 6.3. It is evident that charge recombination is an important physical process, not only because of photopeak broadening but also because it reduces the measured pulse amplitude. In fact, while some of the broadening effect is statistical in nature, a part is due to the magnitude of charge recombination as a function of radial coordinate, since this effect depends upon the local field strength. This particular broadening term should

be mostly compensated by photopeak alignment when radial position sensing is used, and can be reduced without photopeak alignment by increasing the strength of the electric field throughout the chamber.

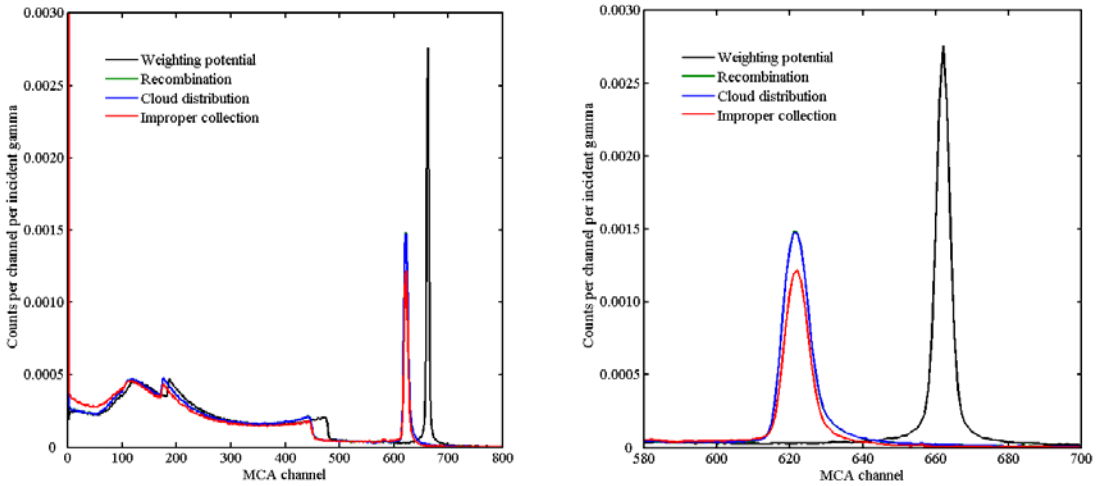

Figure 6.3. A comparison of the energy spectrum broadened by Fano statistics and the weighting potential distribution to the spectra when charge recombination, electron cloud distribution, and improper collection due to nonideal anode biasing are considered.

The distribution of electrons in a cloud at the ionization site shows negligible effect upon the spectrum in Figure 6.3; as mentioned before, this simulation may underestimate the effect of the cloud size due to the fixed cloud structure simulated. The effect in this particular simulation is to average the weighting potential over the cloud volume, so in regions where the weighting potential distribution exhibits little curvature the simulation of an electron cloud is expected to have no effect.

Finally, improper collection of electrons at the noncollecting anode is seen to reduce the number of photopeak counts, although there is not an apparent effect on the photopeak width. The count reduction effect is observed experimentally, and changes with collecting anode bias: see Figure 4.10 for one example. The collecting anode bias was known in advance to be insufficient after studying Maxwell 3D simulations of the operating electric field distribution for a cathode bias of -4000 V. Figure 6.4 shows the electric field lines near the anodes along the central axial plane. In panel (a) there are field lines that originate at the noncollecting anode wires, which are surrounded by blue and green coloring, when the collecting anode bias is V_{CA} = +1400 V. This implies that

electrons can be collected at these wires, since electron drift opposes the direction of field lines.

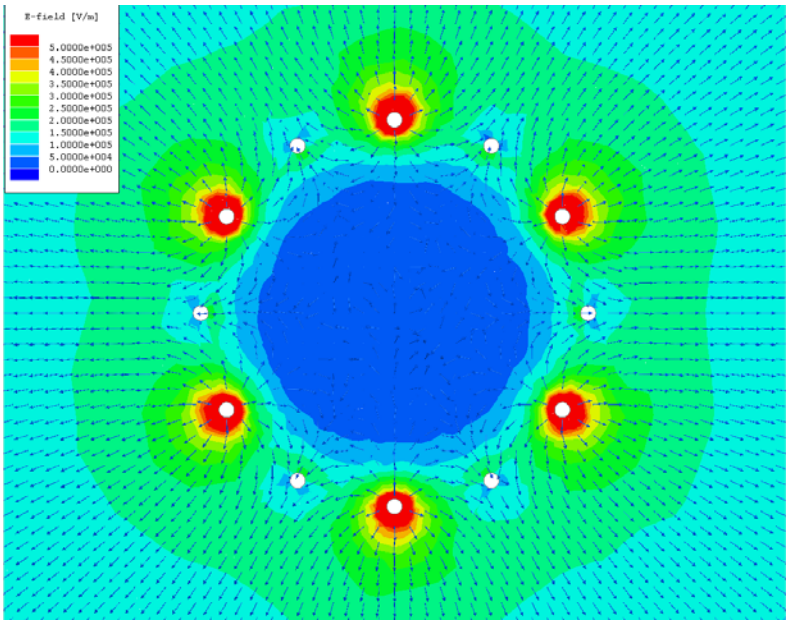

(a)

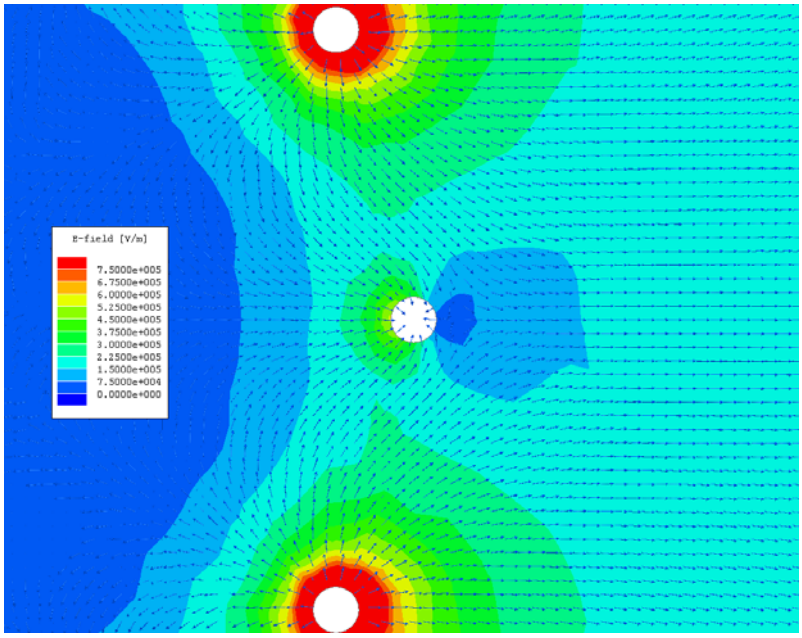

(b)

Figure 6.4. Examining the electric field lines along the central plane near the anodes when V_{cat} = -4000 V; collecting anode wires are surrounded by red. (a) V_{CA} = +1400 V is not sufficient to keep electrons from terminating on the noncollecting anode wires. (b) V_{CA} = +2000 V ensures ideal collection of electrons.

In panel (b) of Figure 6.4, the collecting anode bias is raised to +2000 V. Now there are no field lines that originate at the noncollecting anode, and an electric potential saddle point can be seen in the dark blue region just right of the noncollecting wire. This indicates that no electrons will pass through that region (as discussed in Section 2.2.3), but will instead be redirected toward the collecting anodes at the top and bottom of the figure.

Returning to Figure 6.3, improper anode biasing actually acts to slightly reduce the photopeak width. As will be seen later, events occurring directly outward from a noncollecting anode tend to induce a slightly larger signal than those starting closer to a collecting anode wire, so reducing the electron collection does not affect the low-energy side of the pulse-height distribution, but it does drop the events at the high-energy side to lower channels, and thus as long as only a small fraction of electrons are improperly collected, the effect will be to decrease the photopeak width. Events that have a great deal of overlap with a noncollecting anode wire are completely removed from the photopeak, which accounts for the reduced number of observed counts in the figure. Referencing Equation (2.8), the quantitative effect of improper charge collection is that every electron terminating at the noncollecting anode carries a weight of -1 instead of +1, so each improperly-collected electron actually reduces the measured amplitude by a weight of 2. Thus, events with substantial electron collection at a supposed noncollecting wire end up far outside the photopeak, and may appear in a negative MCA channel.

The next effect to be studied is that of the Gaussian filtering. Figure 6.5 displays two spectra of shaped anode difference signals: one adds the shaped maximum of each individual response for every interaction in multi-site events to obtain the shaped amplitude, and this spectrum is labeled “geometry” because it represents the change in the response of the shaping filter to events throughout the geometry. The other spectrum accounts for time-of-arrival differences in multi-site events, which reduce the overall amplitude because the individual maxima do not overlap (see Figure 6.1); this spectrum is labeled “timing.” For comparison to Figure 6.3, these two spectra are plotted along with the spectrum of anode difference amplitudes when improper electron collection is considered. In Figure 6.5 it is evident that the geometrical response of the shaping filter

only broadens the photopeak by a small amount, while timing adds in a small, but noticeable, low-energy tail on the photopeak in addition to further broadening.

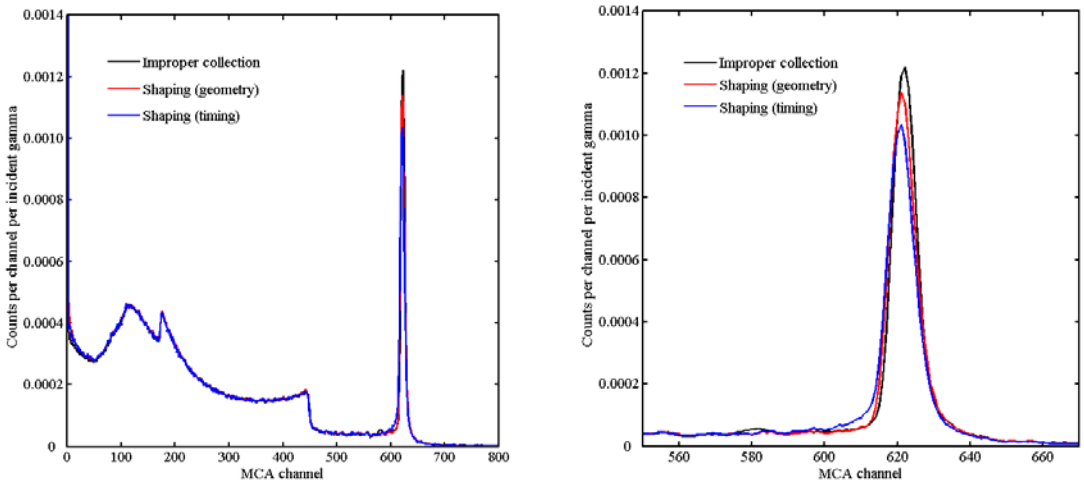

Figure 6.5. Examining the effects of shaping upon the energy spectrum. The shaping process is divided into two portions: a geometrical part and a time-of-arrival part.

In the final set of plots, the spectrum of events after shaping is first broadened with electronic noise; the effects of axial field nonuniformity are added next by using better approximations to the local field values, not simply projecting the distribution at the central plane throughout the entire chamber. Finally, radial position sensing is implemented to align photopeaks as a function of calculated radial location. It is obvious from this figure that electronic noise is a major contributor to the overall peak broadening. Axial field nonuniformity is also an important contributor, not only because it broadens the photopeak even further, but because it also results in a large loss in photopeak counts. This is due to the end gas spaces on either end of the chamber, where the relatively weak electric fields result in stronger recombination and also large ballistic deficit due to the long signal rise time compared to the shaping time constant.

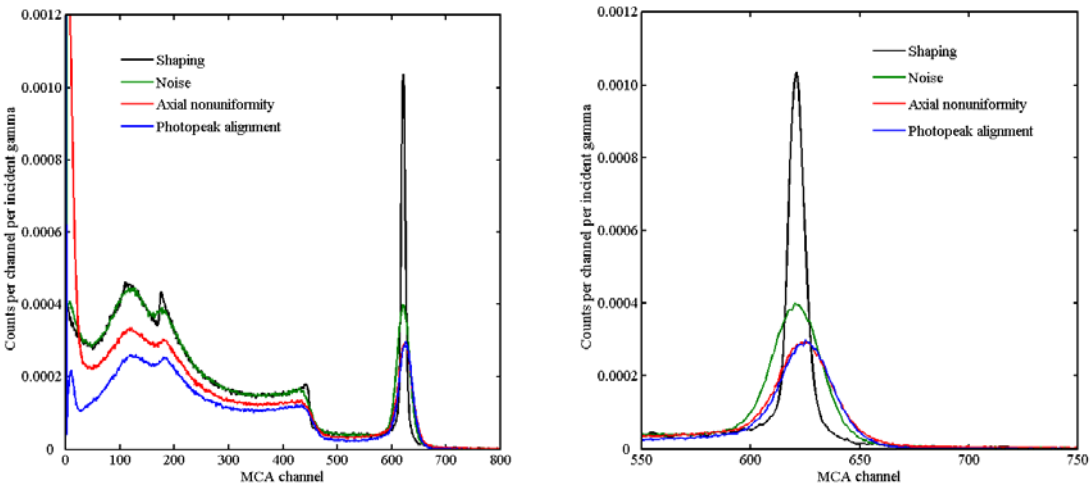

Figure 6.6. Comparing the shaped spectrum without noise, labeled "Shaping," to that when noise, axial field nonuniformity, and photopeak alignment are considered. The figure on the right enhances the photopeak region to better display differences.

There is another subtle effect produced by the axial field nonuniformity, which is an upward shift in the photopeak centroid by several channels. To investigate this, the previous set of simulations was repeated, but instead of projecting the field distributions from the central plane throughout the entire HPXe detector volume, this time the distribution used came from a plane offset from the center by 48 mm, which is near the end of the central detection volume. The results are shown in Figure 6.7. In the figure it can be seen that the weighting potential distributions from the two planes are nearly identical. The effects of charge recombination are radically different, though, with the plane offset by 48 mm exhibiting a much broader distribution of charge loss due to recombination, although the centroid of this distribution is observed to be between 15 and 20 channels higher than the more uniform distribution from the central plane. Apparently, the electric field near the edge of the central volume is measurably stronger in magnitude and also less uniform throughout the plane. This difference in recombination explains the axial effects observed in Figure 6.6, and will be observed experimentally in Chapter 7.

Returning to Figure 6.6, it is possible to see the beneficial effects of the photopeak alignment process upon the measured peak FWHM in the right panel. In the left panel, the reduced Compton continuum can be clearly observed.

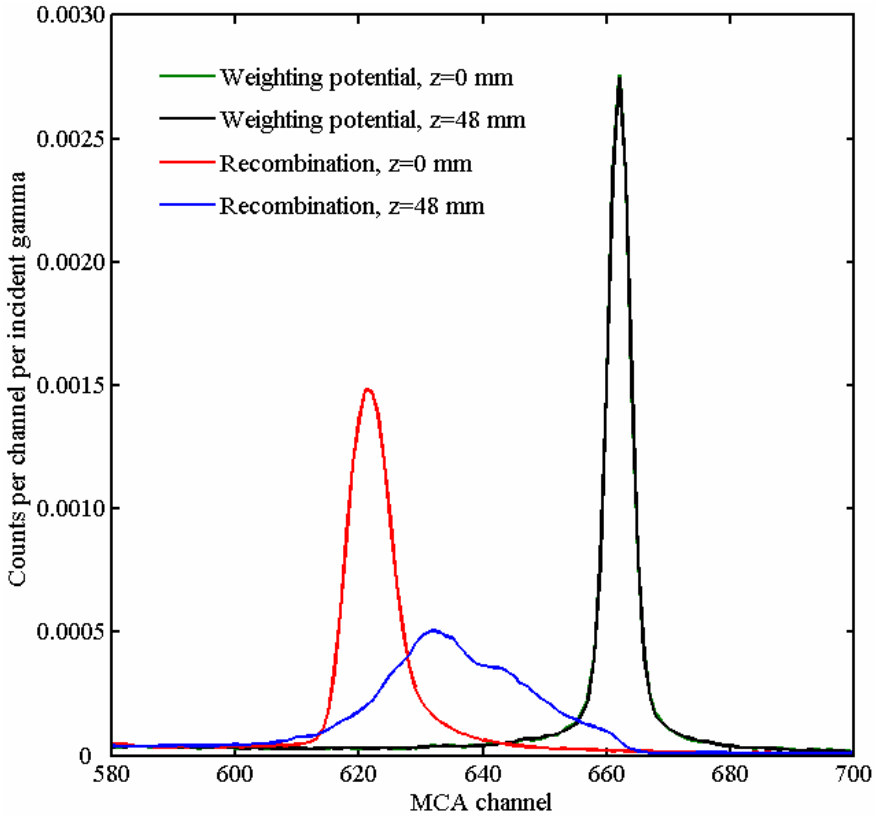

Figure 6.7. A comparison of the simulation results when the field distribution projected throughout the entire volume corresponds to the planes z = 0 or z = 48 mm. The weighting potential distributions from these two planes are nearly identical.

The physical processes impacting the measured energy resolution in a spectrum have so far been discussed only in a qualitative manner. To quantify the effects that have been observed in the preceding figures, let us assume that each process, when acting upon an input distributed evenly in space and as a delta function in energy, produces a normally-distributed spectrum with an associated FWHM. Since these processes are Gaussian, the FWHM of each one sums in quadrature to produce the FWHM measured in the final spectrum. By simply measuring the FWHM of each spectrum tallied, the FWHM of each process can be calculated easily with the aforementioned assumptions. FWHM measurements were performed by importing the data into EG&G ORTEC's MAESTRO software, which has built-in peak fitting algorithms; the final results are shown as a histogram in Figure 6.8 in ascending order of the process' FWHM. The total measured FWHM is also shown in red for reference.

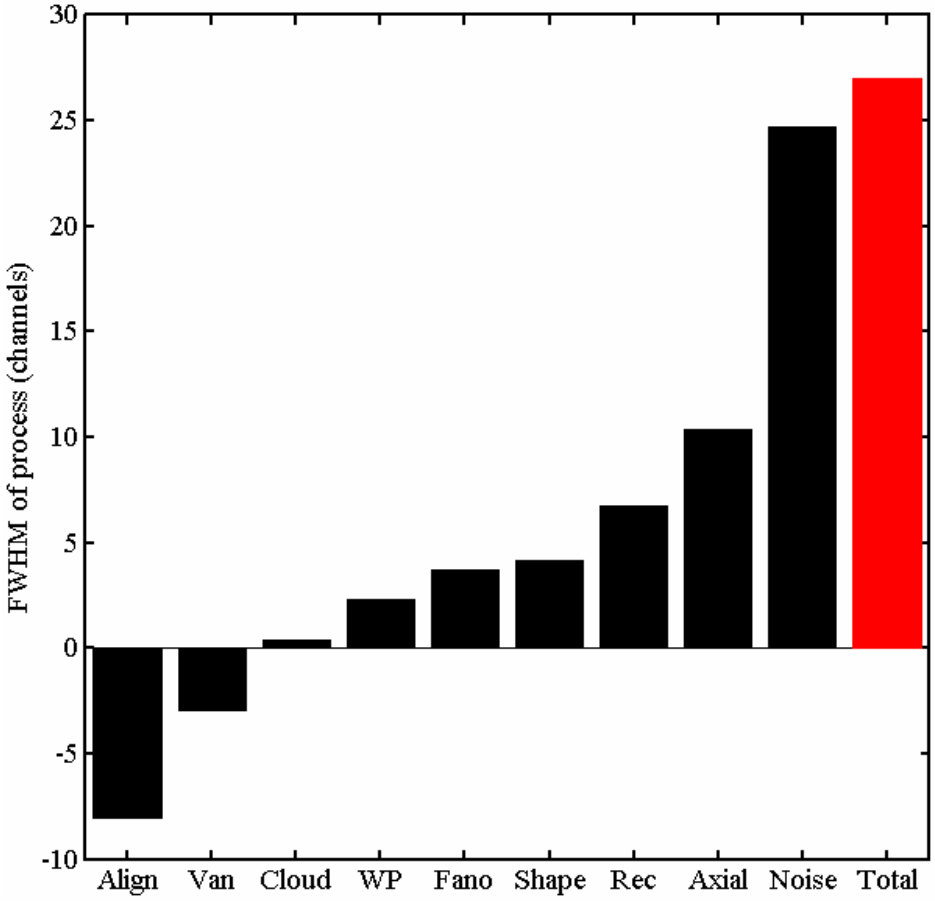

Figure 6.8. A comparison of the FWHM attributed to each physical process studied in the simulations. V_{an} refers to improper anode bias and the resulting incomplete charge collection; the effects of the shaping filter have not been split into separate components.

In the figure it is obvious that electronic noise is by far the largest contributor to the measured photopeak FWHM. Other contributors to the measured FWHM that would ideally need to be reduced to produce an excellent spectrometer are the axial field variations and the charge recombination, which is actually slightly more important than the histogram conveys because the associated large downshift in centroid channel is not taken into account here. Terms that reduce the measured FWHM—charge recombination and photopeak alignment—are represented in the histogram by negative FWHM values, although technically these terms are imaginary when using the method of summing component terms in quadrature.

Table 6.2. A summary of important results from the physical effects study.

Process	*FWHM (channels)*	*Centroid (channels)*	*Normalized peak area*
True deposition	0	662	1.000
Fano statistics	3.74	662	0.993
Weighting potential	2.28	662	0.785
Recombination	6.77	621.7	0.736
Cloud distribution	0.40	621.7	0.739
Improper collection	(2.93*i*)	621.8	0.555
Shaping, geometry	3.34	621.3	0.550
Shaping, timing	2.50	621.0	0.534
Electronic noise	24.74	621.0	0.586
Axial nonuniformity	10.37	624.6	0.468
Peak alignment	(8.03*i*)	625.4	0.456

Table 6.2 lists the important quantitative parameters for each physical process: the process' FWHM, the measured photopeak centroid after the process is tallied, and the normalized peak area after the process is included. The only significant shift in centroid location comes from charge recombination, although the effect of axial field nonuniformity can be seen. The normalized peak area includes some uncertainty that depends on the background stripping algorithm and the placement of the region-of-interest boundaries; still, it is evident that the improper anode biasing and axial nonuniformity have real effects on the measured number of photopeak counts. The weighting potential distribution also seems to reduce the photopeak area significantly by distributing counts from the anode region far beyond the photopeak.

6.1.3 Analysis of Events Along an Arc of Fixed Radius

One question that arises from the preceding study is: how does electron termination at the noncollecting anode decrease the distribution of signal amplitudes produced by the anode differencing circuit? A hypothesis was proposed in the previous section without any analysis; the question will now be studied.

To investigate this question, let us assume the same operational conditions used in the previous simulations—i.e., the same source, electrode biasing, and shaping filter conditions. Let us fix the interaction radius at a large value, 40 mm, and simulate interactions at 0.1° intervals between 0 and 30.0°; the electric field and weighting potential should be very uniform this far from the anodes, so weighting potential and recombination differences will be negligible. The simulations described in the previous section are now repeated, and the results displayed in Figure 6.9 as a function of azimuthal angle. For reference, the collecting anode is centered at azimuth 0°, the neighboring noncollecting wire at 30°. The right panel in the figure expands the range near ordinate unity for a better view of functional behavior.

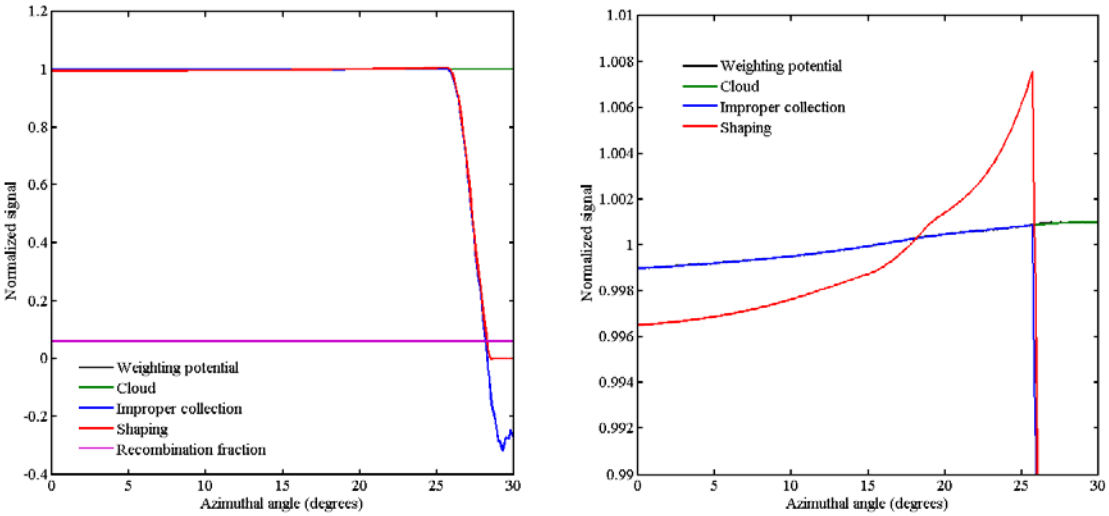

Figure 6.9. Investigating the effect of azimuthal angle on the distribution of signal amplitudes. The collecting anode is centered at 0°, the noncollecting anode at 30°. The right panel zooms in on the region around unity ordinate for clarity.

On the left panel, it is obvious that recombination is nearly constant for all of the points considered; the weighting potential difference at the interaction point (black) and averaged over the entire cloud (green) also appear to be constant with angle. The effect of improper electron collection can be seen in the blue data series: the distribution is fairly uniform to the eye between azimuths 0 and 26°, but then falls of quickly to negative values, indicating more electrons being collected at a designated noncollecting anode wire than at the collecting anode. The shaped signal amplitude (red) follows the

collected charge closely, although it does not go negative because the method for measuring the shaped signal amplitude in these simulations is to return the most positive value, not the largest deviation from the baseline.

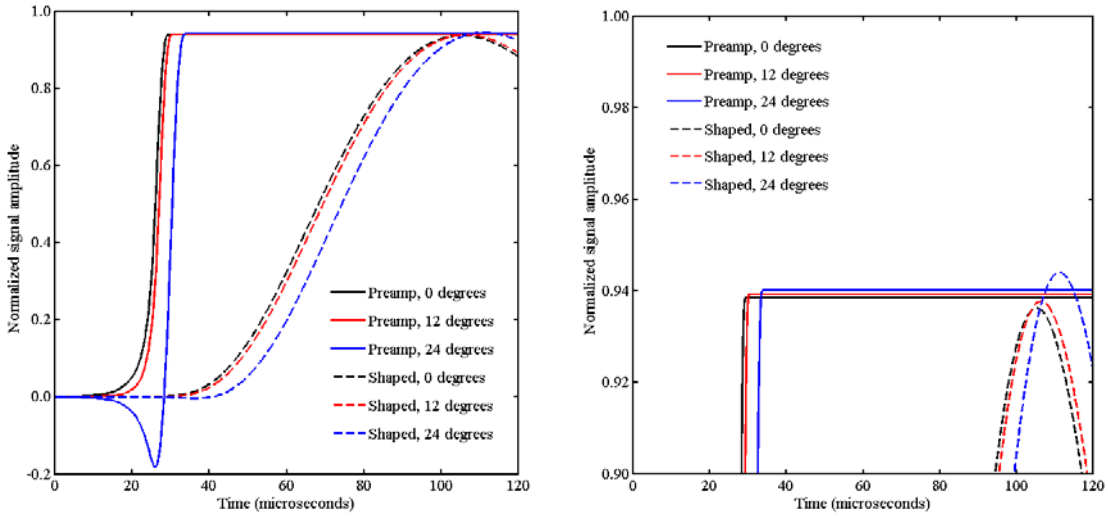

Figure 6.10. A plot of preamplifier and shaped waveforms for different azimuthal angles (left). Zooming in on the peak region shows the nonlinear response of the shaping filter (right).

The right panel of Figure 6.9 zooms in to show more subtle behavior. It is now apparent that the weighting potential difference distribution is not perfectly uniform, but instead appears to give a slightly larger net induced charge nearer the noncollecting anode (this assumes perfect collection of electrons, of course, which is not the case). Still, the weighting potential variation from one extreme to the other is only about 0.2%. The shaping filter response as a function of angle is more interesting. The filtering results in an amplitude deficit compared to the net weighting potential difference for events nearer the collecting anode; as the azimuthal angle increases, the filter response increases nonlinearly and eventually surpasses the net weighting potential difference. This indicates that the shape of the preamplifier difference signal impacts the filter response, as the preamplifier difference signal has a slightly more gradual slope for electrons directly approaching the collecting anode than those closer to the noncollecting wires. The difference in preamplifier signal shape is demonstrated for three locations in

Figure 6.10: azimuths 0, 12°, and 24°. The imperfect shaping filter response explains the process' contribution to the measured photopeak FWHM, as shown in Figure 6.8.

6.1.4 Photopeak Broadening Contributions for Realistic Shaping Times

The studies performed in the preceding sections provide useful information, but do not use shaping times comparable to the experimental conditions. The simulation of Section 6.1.2 is repeated here using a shaping time constant of 12 μs, which is used in most of the experiments performed on the system. This change will not affect the contributions from Fano charge statistics, weighting potential, recombination, or incomplete charge collection. It will, however, change the contributions from the shaping filter, as ballistic deficit will increase. In addition, the system electronic noise will decrease, as observed in experiments. The ENC used in this simulation is linearly interpolated between experimentally-measured values: 390 electrons.

The results of this study are displayed as a histogram in Figure 6.11; the data for a 20 μs shaping time is included for comparison. The spectra are not shown because they are qualitatively very similar to the 20 μs case, just with different peak widths. The measured photopeak FWHM for the 12 μs case has decreased due to the diminished electronic noise term, despite increases in the FWHM contributions from shaping and axial nonuniformities, and less improvement from photopeak alignment. The electronic noise and shaping contribution changes were predicted; the axial nonuniformities become more prominent because the shorter shaping time creates different amounts of ballistic deficit along the detector's axis, depending upon the local electric field strength. The photopeak alignment is less successful in this case because the anode sum is also shaped with a 12 μs time constant, which introduces severe ballistic deficit into the shaped anode sum amplitude and compresses the calculated radii into 5 radial bins instead of 6. There is more photopeak centroid variation within each radial bin, an effect that cannot be compensated unless the number of bins is increased. A summary of the simulation results with a 12 μs shaping time are compared to the 20 μs case in Table 6.3; only parameters that differ from those in Table 6.2 are listed.

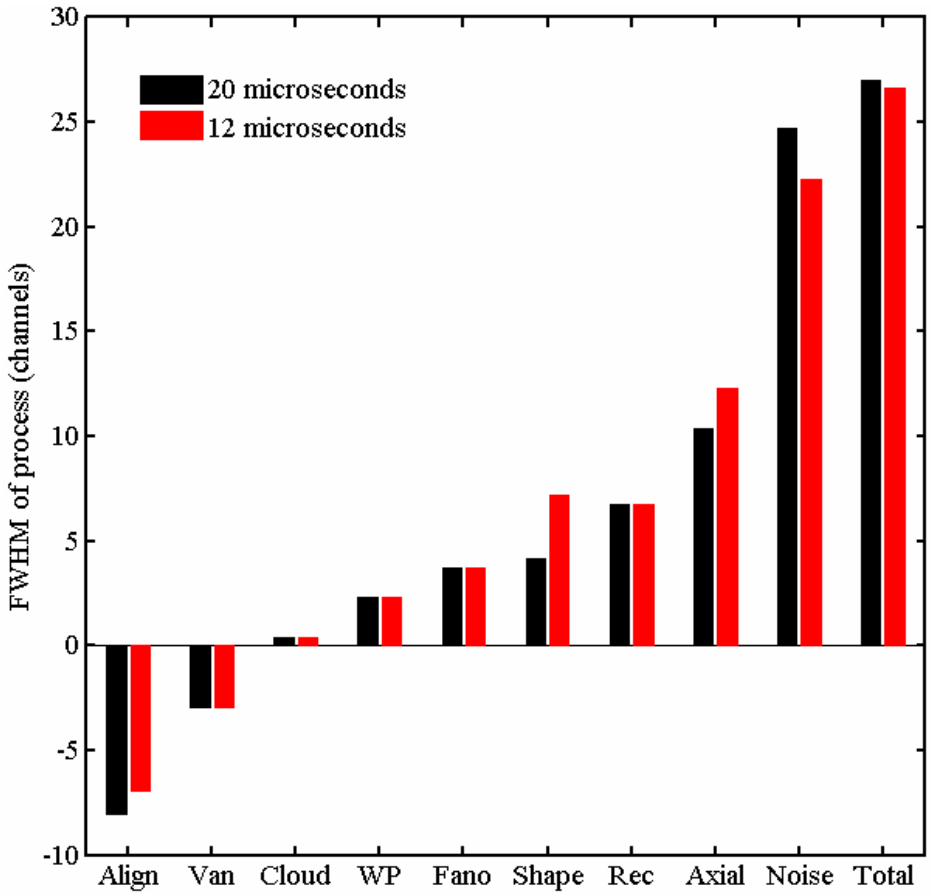

Figure 6.11. A comparison of the peak broadening terms for two different shaping times.

Table 6.3. A comparison of FWHM contributions for two shaping times.

Process	*FWHM (channels), 12 μs*	*FWHM (channels), 20 μs*
Shaping, geometry	6.99	3.34
Shaping, timing	1.64	2.50
Electronic noise	22.29	24.74
Axial nonuniformity	12.29	10.37
Peak alignment	(6.94*i*)	(8.03*i*)

6.2 The Effects of Multiple-Site Events and Interaction Location

It is reasonable to investigate how many interactions recorded in the energy spectrum are due to single-, double-, triple-, and quadruple-site events (the probability of more than four event sites in a single event sequence is quite small). Multiple-site events will contribute to the time-of-arrival contribution to the total peak FWHM, and although this effect does not appear to be significant from the above simulations, larger volumes or higher gas densities would increase the multiple-site contributions. Besides the potential for photopeak broadening, multiple-site events will not register correctly in the radially-separated spectra, but instead will appear at the product of modified individual event radii. To prove this point, consider an N-site deposition; q_n electrons are ionized at interaction location n, which has initial difference and sum weighting potentials $\varphi_n^{diff,i}$ and $\varphi_n^{sum,i}$, respectively. The superscripts *f* and *i* refer to each charge cloud's final and initial locations. In addition, assume ideal detector behavior, with proper collection of all electrons at the collecting anode and negligible difference between the two anodes' weighting potentials throughout the sensitive volume. The measured signals are

$$\begin{aligned}
\Delta Q_{diff} &= \sum_{n=1}^{N} -q_n \left(\underbrace{\varphi_n^{diff,f}}_{\simeq 1} - \underbrace{\varphi_n^{diff,i}}_{\simeq 0} \right) \\
&\simeq -\sum_{n=1}^{N} q_n \\
\Delta Q_{sum} &= \sum_{n=1}^{N} -q_n \left(\underbrace{\varphi_n^{sum,f}}_{\simeq 1} - \varphi_n^{sum,i} \right) \\
&\cong -\sum_{n=1}^{N} q_n + \sum_{n=1}^{N} q_n \varphi_n^{sum,i}
\end{aligned} \tag{6.1}$$

Equation (5.5) can be used to calculate the normalized interaction radius, r_0 / R_{cat} :

$$\begin{aligned}\frac{r_0}{R_{cat}} &= \left(\frac{R_{cat}}{R_{an}}\right)^{\left(\Delta Q_{sum}/\Delta Q_{diff}\right)-1} \\ &= \left(\frac{R_{cat}}{R_{an}}\right)^{\left(-\sum_{n=1}^{N} q_n + \sum_{n=1}^{N} q_n \varphi_n^{sum,i}\right)\Big/\left(-\sum_{n=1}^{N} q_n\right)-1} \\ &= \left(\frac{R_{cat}}{R_{an}}\right)^{-\sum_{n=1}^{N} q_n \varphi_n^{sum,i}\Big/\sum_{n=1}^{N} q_n} \\ &= \prod_{n=1}^{N}\left(\frac{R_{cat}}{R_{an}}\right)^{-q_n \varphi_n^{sum,i}\Big/\sum_{n=1}^{N} q_n}\end{aligned} \tag{6.2}$$

For a single-site interaction the radius expressed in terms of the weighting potential sum is

$$\frac{r_0}{R_{cat}} = \left(\frac{R_{cat}}{R_{an}}\right)^{-\varphi^{sum,i}} \tag{6.3}$$

Thus, comparing equations (6.2) and (6.3) shows that, in theory, the multiple-site deposition causes the calculated radius to be the product of individual radii with energy-weighted exponential arguments.

For some data in Chapter 5, the radial parameter is not calculated using Equation (5.5), but instead the data is binned as a function of the ratio of anode sum and difference signals. In this case a multiple-site event registers in the bin containing the weighted average of the individual bins: this can be shown directly from Equations (6.1):

$$\begin{aligned}\frac{\Delta Q_{sum}}{\Delta Q_{diff}} &= \frac{-\sum_{n=1}^{N} q_n + \sum_{n=1}^{N} q_n \varphi_n^{sum,i}}{-\sum_{n=1}^{N} q_n} \\ &= 1 - \frac{\sum_{n=1}^{N} q_n \varphi_n^{sum,i}}{\sum_{n=1}^{N} q_n}\end{aligned} \tag{6.4}$$

Because multiple-deposition events will in general register at incorrect radii, they cannot be compensated correctly during photopeak alignment. If it is known that these events are relatively prominent, it may be useful to implement a readout system that can properly compensate each deposition, such as pixellated anodes with depth sensing capabilities [65, 101].

To properly investigate the prominence of multiple-site events, let us run the Geant4 simulations described in Section 6.1.2 (20 μs shaping time constants) while recording the number of energy depositions for each primary photon; then, event number statistics and energy spectra can be created for each recorded event number. Let us lump all event numbers of 5 or higher together into a single tally, and let us also create separate tallies of the number of full-energy depositions and the number of events occurring in the photopeak, defined as the region between channels 550 and 700 in the energy spectra. These two tallies are not necessarily the same, since energy can be deposited in regions of low sensitivity, therefore resulting in a significantly-lower recorded pulse amplitude. The results from this simulation are specific only to the source defined in the model: changing the gamma-ray energy will certainly change the relative prominence of multiple-site events.

In Figure 6.12, it is obvious that single-site events are by far the most common of all event numbers; beyond three-site events, the contribution to the total energy spectrum is negligible, which is why this data is not displayed. There are also a few other effects that are of interest from the spectrum: the photopeak seems to broaden somewhat as the number of recorded interactions increases, likely caused by the variation of the detector response at each interaction site; the photopeak centroid decreases as the number of interaction sites increases, presumably created by drift-time differences causing the post-shaping pulse-height deficit discussed earlier in this chapter; and the photopeak becomes more prominent in comparison to the Compton continuum, which makes sense since full-energy depositions are more likely with multiple interactions. Table 6.4 lists the numerical values obtained for photopeak centroid; FWHM (without peak alignment); the peak-to-total count ratio, where the peak counts are those between channels 550 and 700; and the total number of counts in the spectrum. The photopeaks for the 4- and 5+-site spectra are so poorly defined that photopeak information was not obtained. It seems that

as a rule of thumb, increasing the number of interaction locations by one decreases the probability of occurrence by roughly an order of magnitude.

Table 6.4. Comparing spectral features as a function of the number of interaction sites.

Event Number	*Peak Centroid*	*Peak FWHM*	*Total Counts*	*Pk/Total Ratio*
1	625.9	27.36	2.378×10^6	0.067
2	621.9	28.30	4.081×10^5	0.167
3	618.3	27.88	6.091×10^4	0.258
4	-	-	7.231×10^3	0.331
5+	-	-	0.703×10^3	0.358

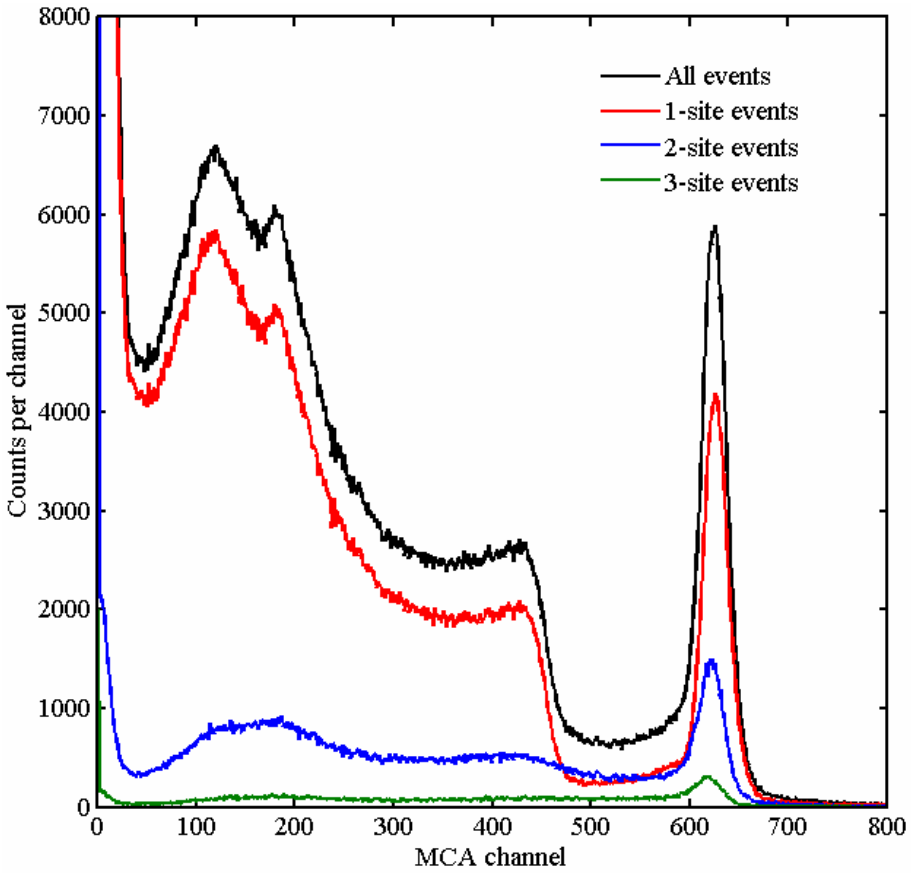

Figure 6.12. Simulated ^{137}Cs energy spectra plotted as a function of the number of interaction sites. The data for 4 and 5+ interactions are not shown because those spectra cannot be seen on this vertical scale to the small number of recorded counts.

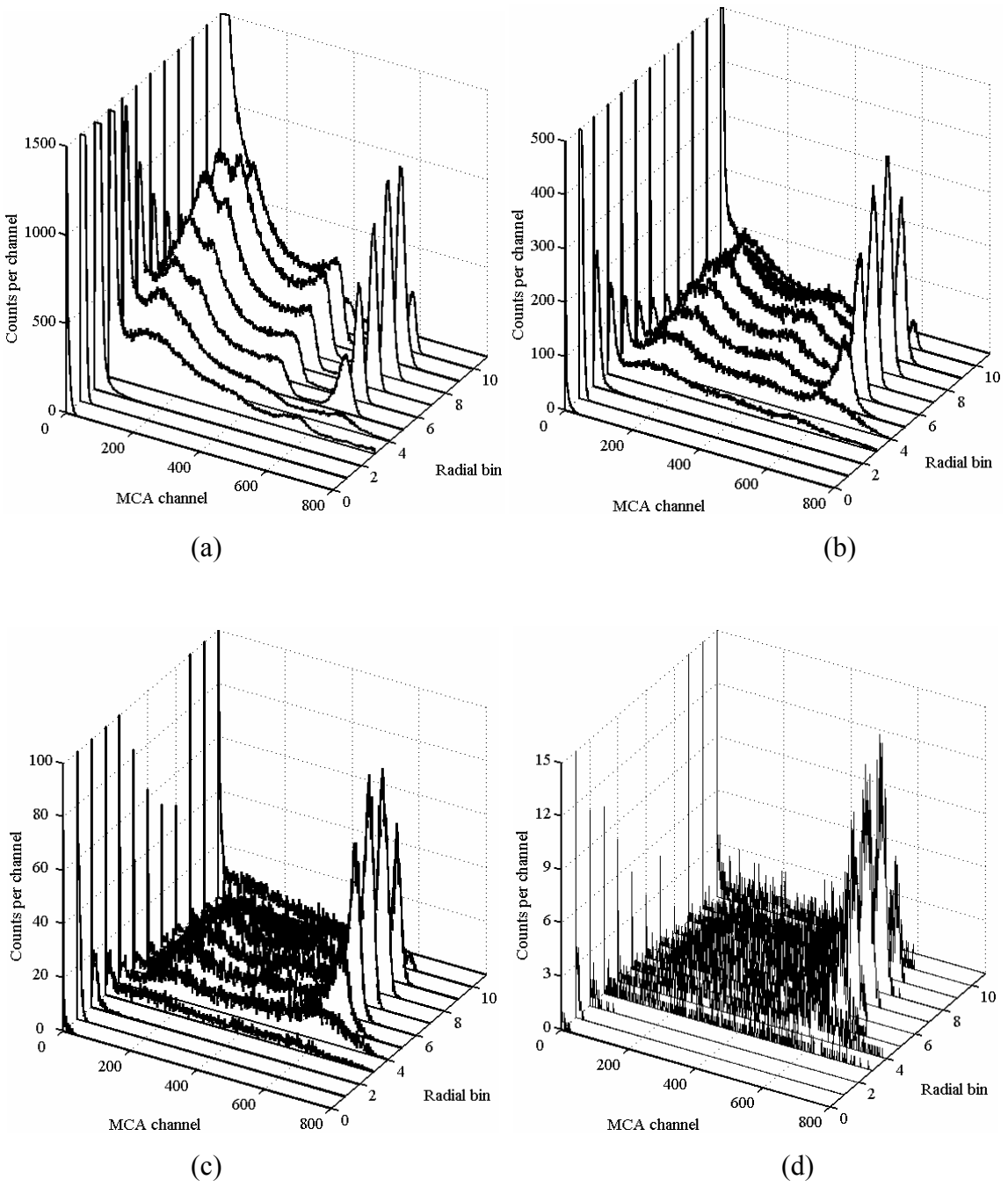

Figure 6.13. A comparison of simulated ^{137}Cs radially-separated energy spectra for (a) 1-site, (b) 2-site, (c) 3-site, and (d) 4-site events.

The radially-separated energy spectra for all event sequence types—except those with 5 or more sites, which are too rare for a spectrum to have meaningful statistics—are shown in Figure 6.13. For comparison, the corresponding all-event radial spectrum has been presented already as Figure 5.4. These spectra show that as the event number

increases, the most probable measured radius decreases, from bin 9 to 8 and finally to 7. Let us apply the photopeak alignment algorithm developed for the simulated all-event energy spectrum to each individual interaction-number spectrum to determine the effect of improper radius measurement on the ability to correct photopeak misalignment. The results from this study are presented in Table 6.5, with the spectra plotted in Figure 6.14; it is clear that the single-site interaction spectrum has improved energy resolution after the photopeak alignment procedure, but multiple-site events actually exhibit degraded resolution due to the compensation. This confirms the prediction that multiple-site events would not be properly compensated.

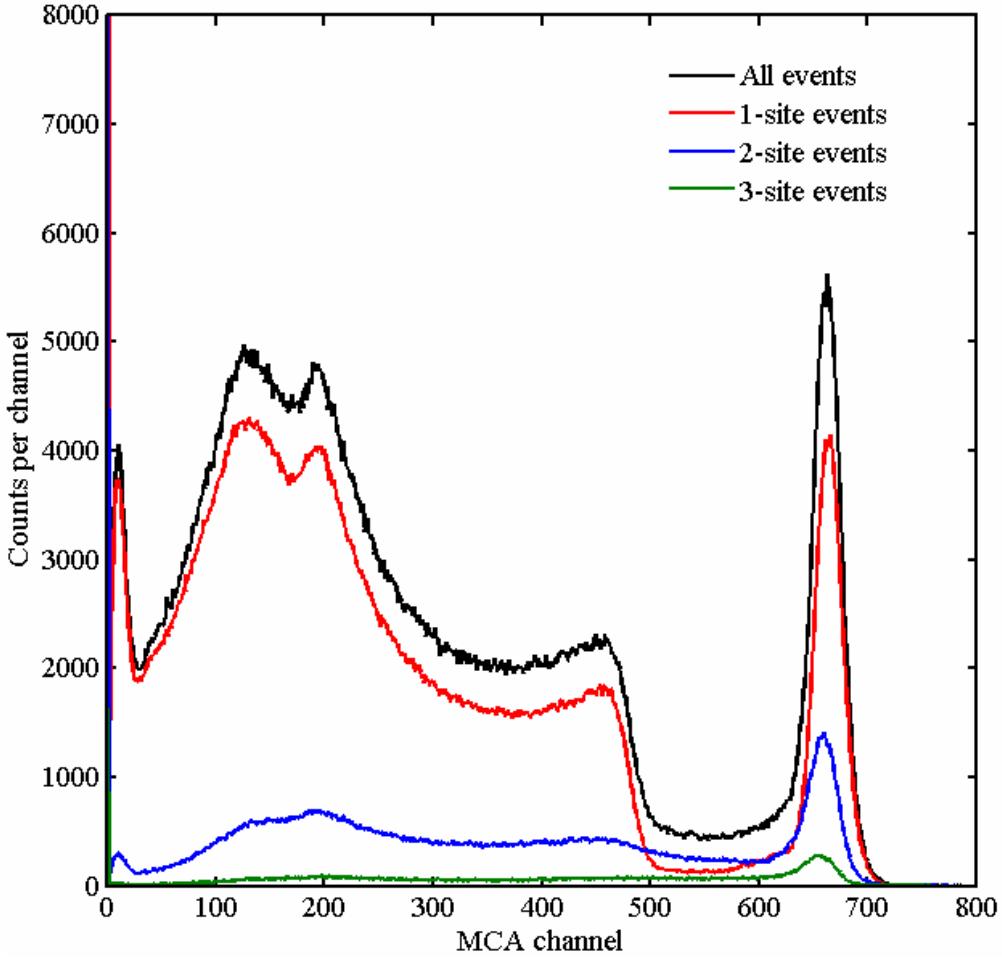

Figure 6.14. Simulated ^{137}Cs spectra sorted by the number of interaction sites. Photopeak alignment has been applied to each spectrum individually.

Table 6.5. Comparing the simulated energy resolution before and after peak alignment.

Number of interaction sites	*Resolution (FWHM at 662 keV) before peak alignment*	*Resolution (FWHM at 662 keV) after peak alignment*
1	4.4%	4.2%
2	4.6%	4.7%
3	4.5%	5.1%

Table 6.6. Comparing the prominence of event sequences for ^{137}Cs gamma-ray detection.

Number of interaction sites	*Full-energy depositions*	*Recorded photopeak events*
1	64.3%	64.6%
2	28.2%	27.9%
3	6.5%	6.5%
4	1.0%	1.0%
5+	0.1%	0.1%
Total number of events	349,828	238,970 (68.3%)

Table 6.6 shows the results of the full-energy event and photopeak tally breakdowns. The two tallies are in numerical agreement when statistical uncertainties are considered, meaning it is no more or less likely for a single-site full-energy event to appear in the photopeak than a three-site full-energy event. From this table, it is apparent that beyond three interactions the probability of an event sequence contributing to the photopeak is negligible. The last row totals the number of each tally type over all event sequences, and the results indicate that, for 662-keV gamma rays, when the full energy is deposited in this HPXe detector, 68.3% of these events will be recorded in the photopeak. The rest will be spread out to higher energies (due to weighting potential) or lower energies (weighting potential or low electric field strength). This result would seem to indicate that most of these events are shifted to low energies due to the local electric field strength, as about 1/3rd of the total gas volume lies in regions suspected to suffer low field strengths—primarily the end gas regions, but also the core of the anode structure.

The end regions of the detector are known to have weak fields from the Maxwell 3D simulations: the reason this is so is because the cathode does not extend into these

regions, so the outer boundary is held at ground potential instead of -4000 V. A plot showing the field magnitude in the XZ plane is shown in Figure 6.15. The scale is chosen such that the dark blue corresponds to regions where electrons drift at less than the saturation velocity of 1 mm/μs [48]. The field in the central gas space is uniform and sufficient to maximize the drift velocity, except inside the core of the anode structure. The very high fields at the outer wall are not in the gas volume, but are instead in the small gap between the biased cathode and the grounded pressure vessel. Outside of this central region, though, most of the chamber suffers weak field strength except for very near the anode wire ends. One final point of interest is that the field strength can be seen to increase near the cathode at the ends of the central volume, explaining the recombination variation observed in Figure 6.7.

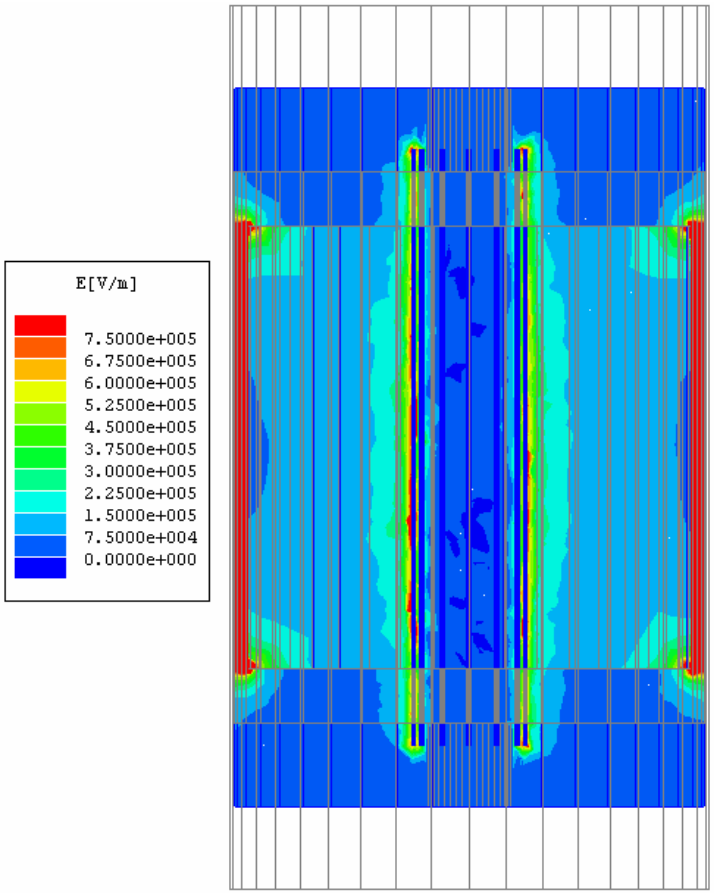

Figure 6.15. Maxwell 3D simulation results displaying the electric field strength on the XZ plane when the cathode and collecting anode are biased to -4000 V and +1400 V, respectively.

Because the fields in the end regions are weak, energy deposited in these spaces are expected to suffer from significant charge recombination and ballistic deficit. To test this theory, the previous Geant4 ^{137}Cs point source simulation used to study event sequences was also used to create two more spectra: one with all events included, and one that omitted events that deposited some energy in the end regions. The results are shown as Figure 6.16. It is clear that, as predicted, the photopeak region is not affected significantly by end-event exclusion. On the other hand, for energies in the Compton gap and below, the number of counts registered in each channel decreases when the end events are discarded. This effect can be clearly observed in collimation experiments; see, for example, Figures 4.13 and 4.14.

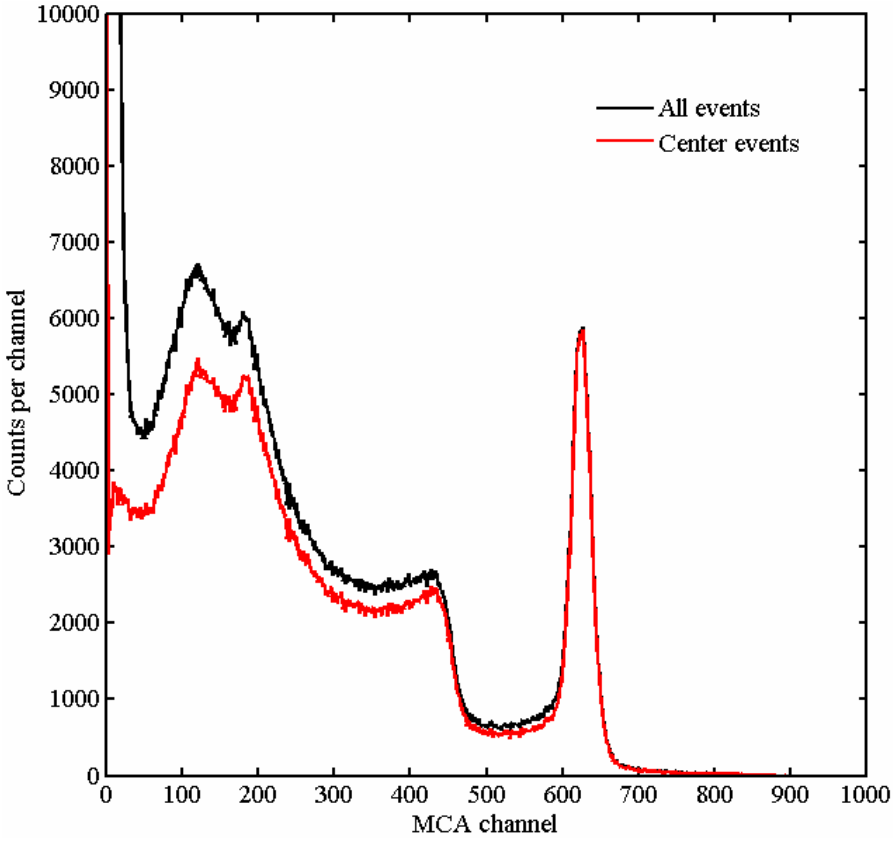

Figure 6.16. Simulation results of ^{137}Cs spectra for all events (black) and excluding events that contain at least some energy deposited in the end gas spaces (red).

6.3 Structural Material Effects on the Energy Spectrum

To clearly identify multiple photopeaks in a single energy spectrum, the prominence of Compton continua should be reduced as much as possible. This is partly a function of the cross sections of the detection medium, but it also depends upon the amount of scattering off of surrounding materials. In the case of HPXe chambers, the gas comprises only a small fraction of the total detector mass: 330 g of 4.960 kg for detector HPXe1, 295 g out of 4.670 kg for HPXe2. The significant mass attributed to structural materials is expected to contribute heavily to the Compton continuum in the recorded energy spectra. To test this hypothesis, a Geant4 simulation was set up to investigate the effects of the surrounding structural materials. A ^{137}Cs point source aligned at the detector's central axis was simulated; this is important to state because the source positioning will have an important effect on the results of this simulation. In this case, the source is positioned such that the gamma rays will generally be passing through the minimum amount of structural material possible to reach the Xe fill gas, so it is nearly a best-case scenario. If the source were irradiating the detector from one end, the thickness of steel and Macor the gammas would pass through before reaching the sensitive volume would increase dramatically, thus increasing the fraction of photons reaching the HPXe gas having been scattered into lower energies.

In this simulation, four cases have been studied: one with the normal structural materials in the appropriate dimensions; one with the steel pressure vessel replaced by a vacuum; one with the Macor internal structures replaced by a vacuum; and one with both the steel and the Macor replaced by vacuum. By substituting the normal materials with vacuum, the material effects can be isolated without geometry changes. The final simulation case effectively is modeling only the Xe gas, so it is a best-case scenario as far as the peak-to-Compton count ratio is concerned. The results are shown in Figure 6.17. It is evident from this simulation that the maximum photopeak height is reduced by about 1/7th due to the presence of scattering materials, while these materials also more than double the height of the backscatter peak. Again, since the modeled point source was placed in the most favorable geometry for this simulation, the spectral changes are expected to be even more dramatic for other source locations.

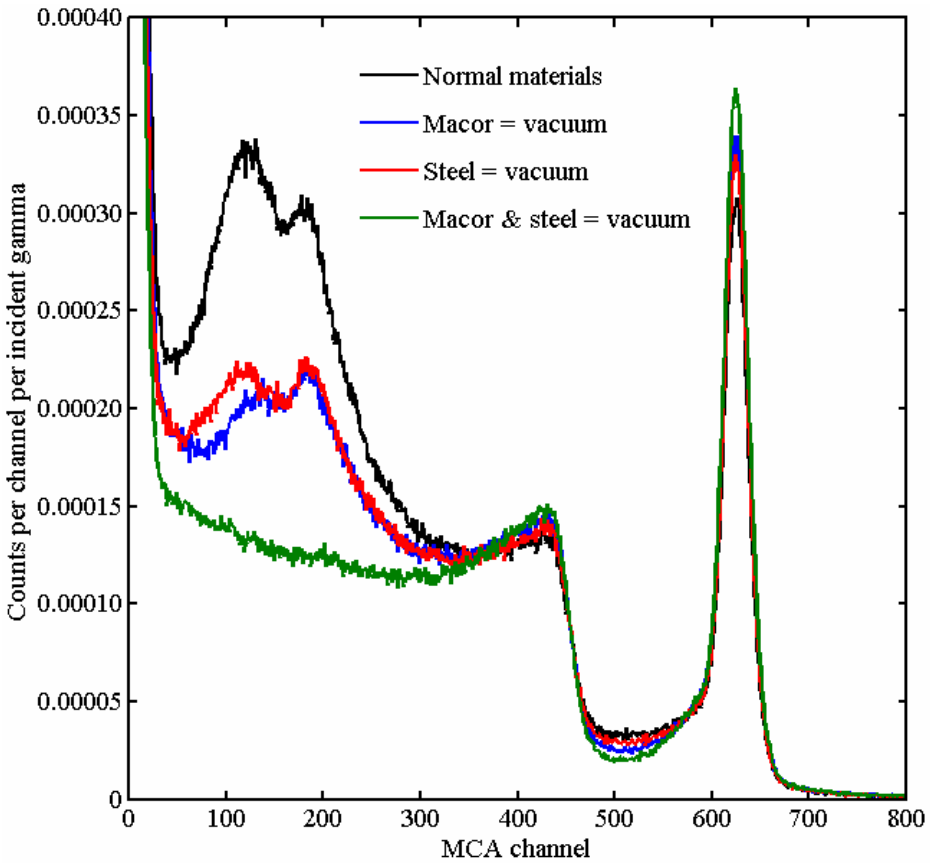

Figure 6.17. The effect of replacing structural materials in the HPXe detector with vacuum on simulated ^{137}Cs energy spectra.

6.4 Summary of Simulation Results

The simulations quantifying physical process contributions to spectral degradation point to the electronic noise as the principal problem regarding peak width. Other non-negligible factors include the axial nonuniformity of the electric and weighting fields, and the variation in charge recombination throughout the chamber. Assuming perfect compensation of every event for recombination and axial nonuniformity, and also assuming the electronic noise can be reduced to nearly nothing, the energy floor is expected to be about 0.9% FWHM at 662 keV for the 20 μs shaping time example, or 1.3% for the 12 μs example. Obviously these assumptions are impossible to realize in experiments, but they do show the absolute performance limitations.

The analysis also show that multiple-site events account for about 35% of photopeak counts for the simulated ^{137}Cs point source. These events were shown to degrade the energy spectrum via a combination of photopeak centroid shifts and peak broadening. To make matters worse, these multiple-site events generally are registered at the wrong event radius, and it is not possible to employ photopeak alignment to improve the energy resolution of multiple-site events—in fact, the alignment procedure further degrades the spectrum of multiple-site events.

The two paragraphs above point toward the necessity of three-dimensional position-sensing, which would be able to identify multiple-site events and provide the capabilities to perform three-dimensional corrections to the measured pulse amplitudes, therefore pushing the energy resolution as close to the limit as possible. In addition, these geometries generally have small capacitances that are conducive to low-noise measurements.

A final suggestion to increase the usefulness of HPXe detectors is to reduce the structural material as much as possible. The structural material decreases the measured photopeak efficiency, making it more challenging to pick out a low-activity, low-energy source when it is engulfed in the Compton continuum of a high-energy gamma ray. This problem is being approached by Ulin et al. [48], who are constructing pressure vessels out of very thin steel tubes coated with carbon fiber composites to achieve sufficient container strength while minimizing the pressure vessel's mass.

CHAPTER 7

IMPROVING ENERGY RESOLUTION WITH COOLING ADMIXTURES

7.1 Increasing Drift Velocity with Cooling Admixtures

7.1.1 The Need for Larger Electron Drift Velocities

One common problem in HPXe ionization chambers is the slow drift of electrons in pure Xe, which saturates near 1 mm/μs, creating the need for long shaping time constants [48]. As observed in this chamber, the minimum electronic noise is measured near 6 μs, but the best energy resolution is obtained using a 12 μs shaping time. The longer time constant is necessary to balance electronic noise with ballistic deficit effects. As suspected from previous experiments and from the simulation results in Chapter 6, electronic noise is the dominant contribution to the measured photopeak width, and ideal performance would be realized if the shaping time could somehow be reduced to take advantage of the lower electronic noise contributions present at smaller shaping time constants. This could occur if the electron drift velocity could be increased in the gas, thereby reducing the ballistic deficit problem at shorter shaping times.

7.1.2 The Effects of Cooling Admixtures

In HPXe detectors, cooling admixtures are small amounts of additives mixed into the purified Xe gas that have the effect of increasing electron drift speeds through the chamber. Typically, small concentrations of H_2 gas—less than 1% of the molecules in the mixture—are used to achieve these results, but other admixtures have been investigated, including He and CH_4 [102].

These admixtures absorb more energy than Xe atoms would in collisions with drifting electrons, thereby reducing the distribution of electron energies in the electron cloud; since the average electron energy is given by $\frac{3}{2}kT$, reducing electron energy can be thought of as "cooling" [103, 104]. Let us refer to the mean energy lost in a collision as $\Lambda(\varepsilon)$, where ε is the electron's energy. Then

$$\Lambda(\varepsilon) = \frac{2m}{M} + f_{inel.}(\varepsilon) \ ; \tag{7.1}$$

in this equation, the first term on the right-hand side represents the loss due to elastic scattering of electrons of mass m interacting with atoms of mass M . The second term represents inelastic scattering, and it is this term that the cooling admixtures increase substantially due to their low-energy excitation, vibrational, or rotational states [103].

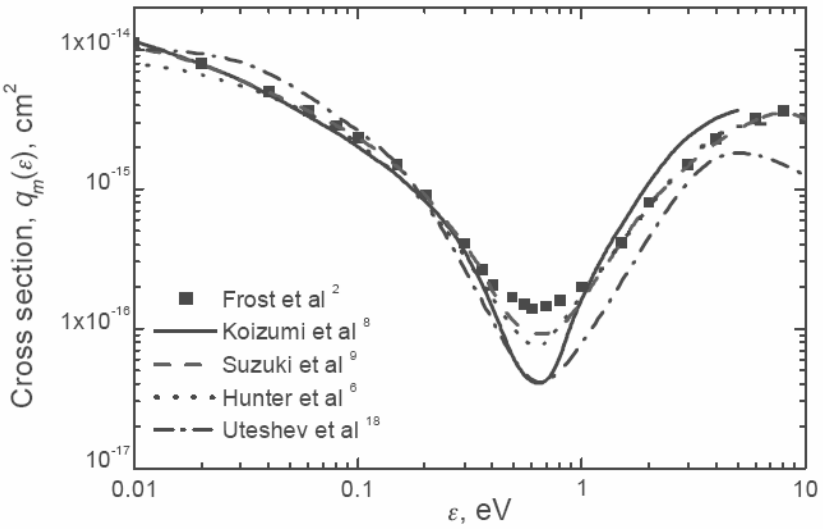

Figure 7.1. The momentum-transfer cross section for Xe (reprinted from [98]). Cooling admixtures shift the electron energies close to the deep minimum near 0.7 eV.

Although it seems counterintuitive that reducing electron energy can increase the drift velocity, the decrease in the electron thermal energy distribution coincides with a very large decrease in the momentum-transfer cross section: see Figure 7.1. This means the electrons can drift longer distances between collisions with gas molecules, with fewer

scatters that slow the electrons and alter their direction. The electrons therefore are able to follow the field lines more closely, reaching the anode having undergone fewer scatters, on average. This reduces not only the drift time, but also the diffusion of particles, resulting in a tighter distribution of electron collection times. Quantitatively, the drift velocity $\boldsymbol{W}$ and the diffusion coefficient D are represented by the equations

$$\begin{aligned} \boldsymbol{W} &= \frac{2}{3}\frac{e\boldsymbol{E}}{m}\left\langle \frac{l(v)}{v} \right\rangle + \frac{1}{3}\frac{e\boldsymbol{E}}{m}\left\langle \frac{dl(v)}{dv} \right\rangle \\ D &= \frac{1}{3}\left\langle \frac{l(v)}{v} \right\rangle^{-1} \end{aligned} \tag{7.2}$$

with $l(v)$ the mean free path between collisions, v the thermal velocity of the electrons, e the fundamental charge, and $\boldsymbol{E}$ the local electric field [104]. The parameter in brackets is simply the inverse collision frequency; by increasing $l(v)$ and decreasing v, the collision frequency decreases, thereby increasing the drift velocity and decreasing the diffusion coefficient. If one balances the energy gained from the field and lost via collisions in a given time increment, then it is not difficult to solve for v and find

$$\begin{aligned} W &\propto \sqrt{\sqrt{\Lambda} E l} \\ D &\propto \sqrt{\frac{E l^3}{\sqrt{\Lambda}}} \end{aligned} \tag{7.3}$$

Because hydrogen is the most efficient cooling admixture, it is the most frequently used in HPXe detectors. The amount of improvement in the drift velocity is a function of not only the amount of hydrogen added, but also the local electric field strength, as shown in the published data of Figure 7.2 [48]. This data shows that, with just a modest amount of hydrogen added to the xenon, the drift velocity can be increased by up to a factor of ten. It is important to note, though, that for low fields the electron drift velocity can actually be slower in the xenon/hydrogen mixture than in pure Xe.

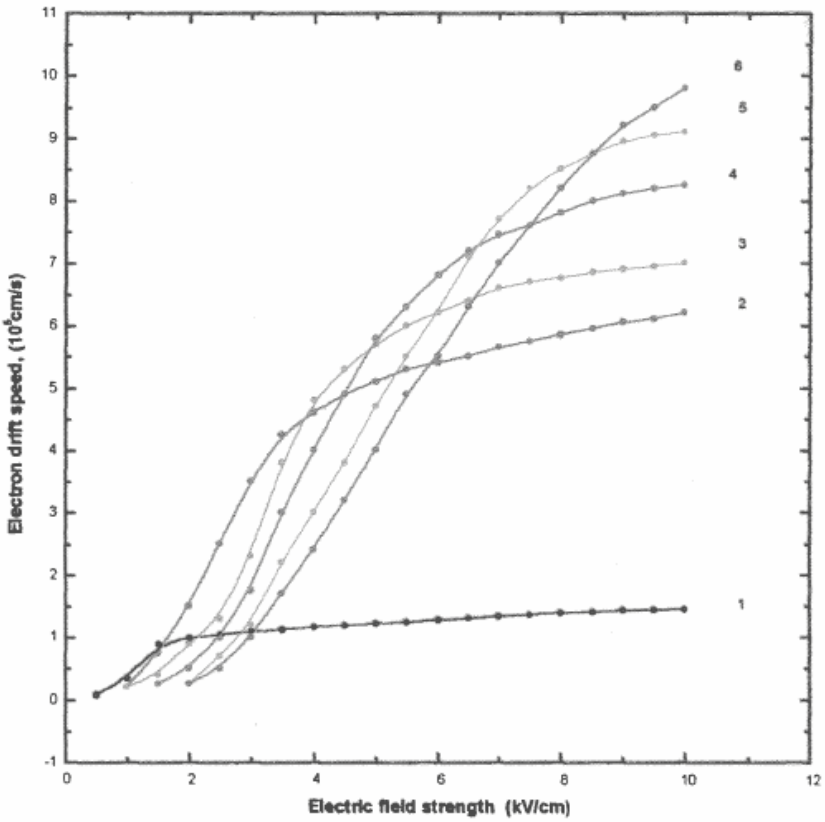

Figure 7.2. Electron drift speed (mm/μs) with different amounts of H_2 as a function of electric field strength. The gas density is held constant at 0.6 g/cm^3. The H_2 concentration for data series 1 to 6 is: 0.0%, 0.2%, 0.3%, 0.5%, 0.7%, 1.0%.

7.1.3 Effects of Cooling Admixtures on Other Detector Properties

It is reasonable to wonder whether the cooling admixtures affect other detector properties besides the drift velocity. The changes in detection efficiency and interaction cross-sections are negligible due to the very small admixture concentration. Recombination along δ-ray tracks becomes more severe due to the more efficient thermalization of electrons, meaning they do not escape the charge cloud as quickly and are more susceptible to recombination. The mean ionization energy, w, for a Xe+H_2 mixture is found to be a function of both gas density and H_2 concentration, but generally the impact of the cooling admixture is fairly small; see Figure 7.3, reprinted from Ulin [48]. Generally HPXe detectors are filled to at most 0.6 g/cm^3, so departure from the pure-Xe w is minimal.

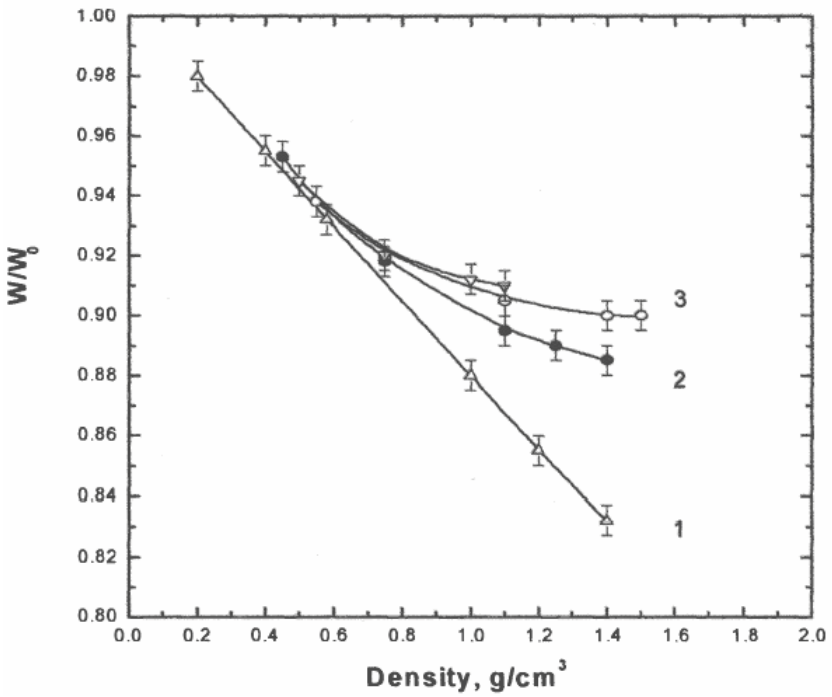

Figure 7.3. A comparison of *w* in doped HPXe, where W_0=21.9 eV. The H_2 concentration is: 0.0% (triangles), 0.1% (filled circles), 0.5% (open circles), and 0.7% (inverted triangles). Data reprinted from Ulin [48].

7.2 Simulation Results for Xenon+Hydrogen Mixtures

The simulation package developed in Chapter 6 to incorporate and quantify the effects of important physical processes has been utilized to simulate the expected energy spectra for the new mixture of Xe and H_2 gases. The only real differences between this simulation and those in Chapter 6 are:

- the gas composition is changed from 100% Xe to 0.2% H_2, 99.8% Xe;
- the shaping time has been shortened to 10 μs;
- the system ENC has been reduced to 381 electrons, corresponding to the new shaping time; and
- axial field nonuniformity is not considered at this time.

To choose a proper shaping time constant, first the detector response is modeled for a variety of shaping times; these simulations are identical in nature to those presented

in Figures 5.2 and 5.3. The only difference between this simulation and the previous case is that gas properties for a 0.2% H_2 composition have been used. The results are shown in Figure 7.4, and indicate that even for the shortest shaping time tried, ballistic deficit is no longer of concern. Choosing a time constant of 10 μs seems to do well for minimizing ballistic deficit appearing in the calculated event radius.

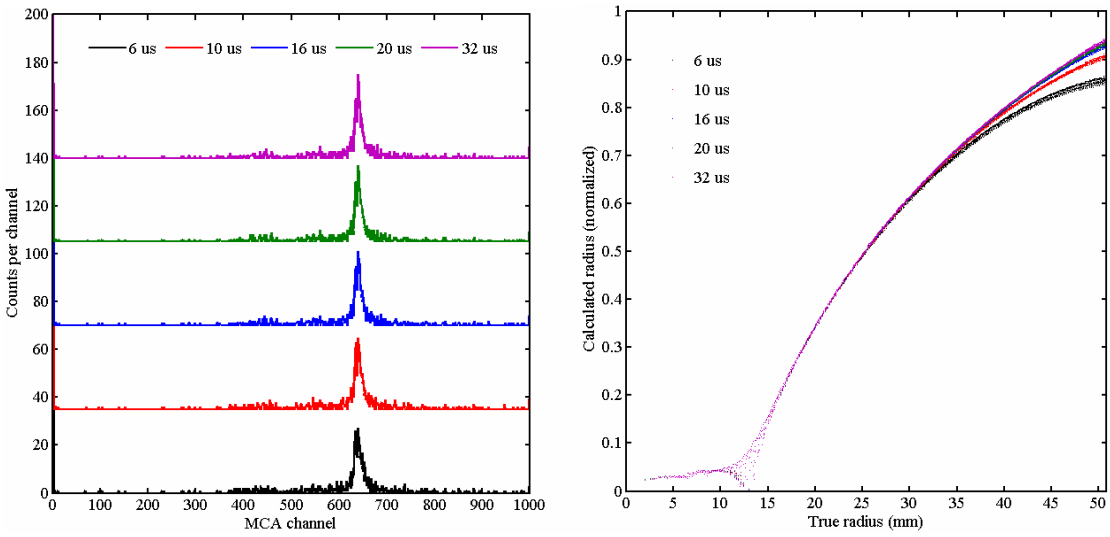

Figure 7.4. A comparison of detector responses for full-energy events when several shaping time constants are used. (Left) The energy spectrum. (Right) The calculated vs. actual event radius.

Now let us consider a full simulation using a 10-μs shaping time, similar to the studies of Section 6.1.2. The only significant difference in the new results seems to be that recombination is more prominent, which coincides with the expectations delineated in Section 7.1.3. A plot comparing the recombination for the Xe+H_2 gas mixture vs. that for pure gas with a 20-μs shaping time constant is shown in Figure 7.5. The FWHM contribution due to recombination in this case is substantial, 11.28 keV, compared to 6.77 keV in the pure Xe case. Fortunately, most of this is expected to be compensated by photopeak alignment, but that would not be possible if the HPXe detector were incapable of radial position sensing. Figure 7.6 compares these simulated spectra before and after photopeak alignment. The simulation's energy resolution improves from 3.7% to 3.3% FWHM at 662 keV via the alignment process; this result seems outstanding, but it is

important to remember that the detrimental effects of axial field nonuniformities are not currently being considered.

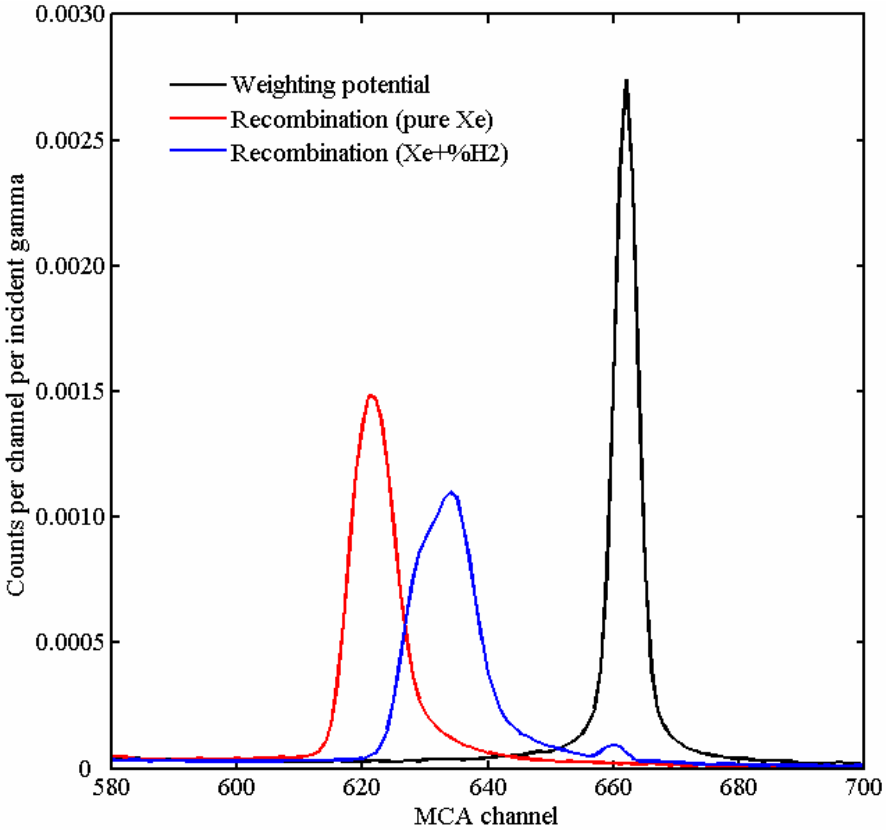

Figure 7.5. A comparison of the simulated distribution of pulse amplitudes after recombination for two gas compositions. The distribution of pulse amplitudes after weighting potential consideration is shown for comparison.

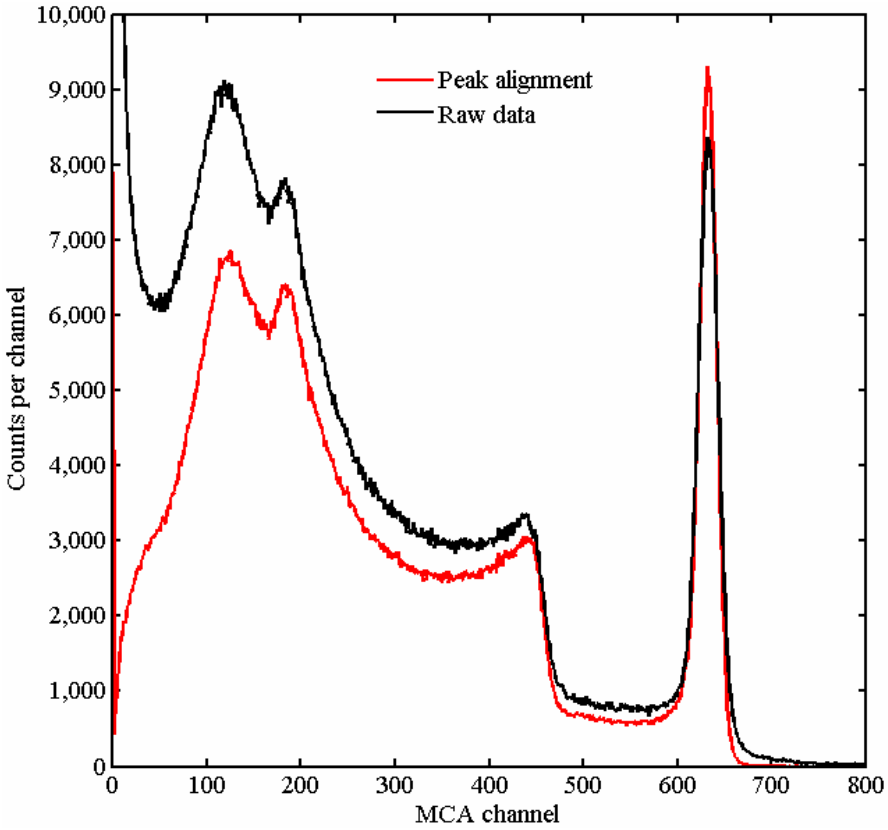

Figure 7.6. A comparison of simulated ^{137}Cs spectra using a Xe+H_2 gas mixture before and after photopeak alignment.

7.3 Hydrogen Addition and Gas Filling

7.3.1 Choosing the Optimal Hydrogen Concentration

To choose the optimal hydrogen concentration for a particular detector, two parameters must be known in advance: the desired gas density and the expected range of electric field magnitudes in the sensitive region of the chamber. Let us keep the same density used in the pure Xe filling, 0.3 g/cm^3. Let us also assume that the chamber will be biased to a maximum of -4500 V on the cathode, +1400 V on the collecting anode. This means the electric field strength near the cathode will be about 750 V/cm. After appropriately scaling the data in Figure 7.2 for density differences, a H_2 concentration of 0.2% was found to be appropriate. This corresponds to a concentration for which the

electron drift velocity in the gas mixture will be equal to, or greater than, it would be for pure Xe throughout the entire sensitive volume of the detector.

7.3.2 Gas Mixing, Purification, and Filling

The gas purification system and filling procedure is largely the same as described in Chapter 4. The detectors were baked for several days to accelerate outgassing of impurities from the detector internals; an ultra-high vacuum was established to remove these contaminants from the system. The xenon was purified in the spark purifier for several weeks prior to filling. When the Xe purification and detector baking were sufficient, the H_2 gas was added to the spark purifier. This step could not be performed far in advance of the actual filling, because the spark purifier treats H_2 as a contaminant and slowly removes it from the Xe gas, thus reducing the H_2 concentration over time.

To obtain the proper amount of H_2 in the mixture, first the mass of Xe in the spark purifier was estimated using the known vessel volume and the measured pressure at room temperature. This allowed direct calculation of the amount of H_2 necessary to achieve the desired concentration in the final gas mixture. The spark purifier was then cooled in a liquid N_2 bath: at 77 K, Xe solidifies in the bottom of the vessel, but H_2 remains a gas, so measuring the vessel's gas space pressure provides a simple way to measure the number of H_2 molecules present. It is always imperative to reduce the concentration of electronegative impurities as much as possible, since they will scavenge drifting electrons to form negative ions, so H_2 was passed through a getter to reduce H_2O, O_2, CO, and CO_2 impurities to less than 1 ppb [105]. After the H_2 was purified, it was directed into the spark purifier, which was filled until a predetermined H_2 overpressure was measured. At that point, the correct amount of H_2 had been added, and the system was sealed and allowed to warm to room temperature. After sufficient warming and gas mixing, the H_2 concentration was verified independently by passing small amounts of the gas mixture into a mass spectrometer and measuring the ratio of H_2 to Xe. Once the H_2 concentration was verified, the detector was filled to a pressure corresponding to the desired density, sealed, and removed from the filling system.

The final measured gas densities and the H_2 concentrations measured with the mass spectrometer are listed in Table 7.1. The gas filling came very close to the desired

H_2 concentration and gas density of 0.2% and 0.3 g/cm^3. Detector HPXe2 was filled about one week after HPXe1 without further addition of H_2; the scavenging of H_2 in the spark purifier can be verified in the H_2 concentration measured just prior to filling.

Table 7.1. Gas properties of the filled HPXe detectors.

Detector	*Added gas mass*	*Final gas density*	*H_2 concentration*
HPXe1	375 g	0.320 g/cm^3	0.23 %
HPXe2	390 g	0.332 g/cm^3	0.16 %

7.4 Gamma-Ray Measurements with Xenon+Hydrogen Gas Mixtures

7.4.1 Initial Experiments

After filling, the detectors were tested using the same peak-hold system described in Chapter 5. The cathode bias was set at -4800 V for detector HPXe2 and -5000 V for HPXe1. The power supply was able to deliver -5000 V, but detector HPXe2 was constrained to lower bias due to arcing at -5000 V. The collecting anodes on the detectors were held at +1400 V for HPXe2 and +1600 V for HPXe1, conditions known from previous testing to be near the point where arcing occurs.

At these biases, pulse waveforms prior to shaping were studied to determine the effect of the gas filling. The anode difference signal was split using a tee: one branch was sent to the oscilloscope, the other to a shaping amplifier. The shaping amplifier output was directed to the oscilloscope and used to trigger the system; a trigger level was set corresponding to a pulse amplitude in the ^{137}Cs Compton gap, so presumably only full-energy events were observed. Anode difference rise times in the 2-3 μs range were observed, and the rise time of the anode sum signal was always less than 20 μs. If these values are compared to the measurements for pure Xe in Chapter 4, it is evident that the new gas mixture approximately doubled the electron drift velocity throughout the sensitive volume, which is exactly the result desired from the Xe+H_2 mixture.

Once a detector was properly biased, the appropriate shaping time for the anode difference signal needed to be established. To properly choose this filter, a series of

collimated ^{137}Cs measurements was made with only the shaping time differing from one measurement to the next. The results for detector HPXe2 are listed in Table 7.2; of these choices, clearly the Canberra 2026 amplifier with a Gaussian filter and a 12 μs shaping time was the optimal choice. Evidently ballistic deficit must still be an important factor, as the optimal shaping time still does not correspond to the electronic noise minimum.

Table 7.2. A summary of collimated ^{137}Cs measurements during the shaping time study.

Shaping time	*Filter type*	*Amplifier*	*Photopeak resolution*	*Electronic noise limit*
6 μs	Gaussian	ORTEC 672	6.8%	3.6%
8 μs	Gaussian	Canberra 243	5.8%	3.5%
10 μs	Gaussian	ORTEC 672	5.9%	3.7%
12 μs	Gaussian	Canberra 2026	5.4%	4.0%
12 μs	Triangular	Canberra 2026	5.7%	3.9%
16 μs	Gaussian	Canberra 243	5.8%	4.0%

7.4.2 Radial Position-Sensing Experiments

After choosing the optimal shaping filter for the anode difference signal, radial sensing data collection commenced. For this measurement the anode sum was shaped with a 16 μs time constant to minimize any effect of ballistic deficit. The radial position was estimated using the ratio of the anode sum to the anode difference signal; the range of expected ratios was divided into 10 bins, based upon the expected position uncertainty, and extra bins were placed just outside this range to register unexpectedly high or negative radial coordinates. For the remainder of this section, data presented will be for detector HPXe2 unless noted otherwise.

Measurements were made in 30-minute intervals. First a measurement was made with a ^{137}Cs source collimated to irradiate only the central plane of the detector with a beam about ¼-inch wide. A test pulse was injected to quantify electronic noise. After this measurement, a background spectrum was recorded for an equivalent counting time. Data processing included background stripping followed by photopeak alignment as a

function of measured radial bin. Photopeak alignment was found to be much more important in the Xe+H_2 gas mixture than in pure Xe experiments with very similar biasing and shaping, as demonstrated by the measured photopeak centroid at each radial bin, presented for both detector gas fills in Table 7.3. This measured effect was predicted by the simulations in Section 7.2. Figure 7.7, which separates the background-stripped energy spectra as a function of measured radial bin, shows this photopeak shift clearly as a function of radial coordinate. The degradation of the weighting potential uniformity near the anodes (radii 2, 3, and 4) can clearly be seen in this figure.

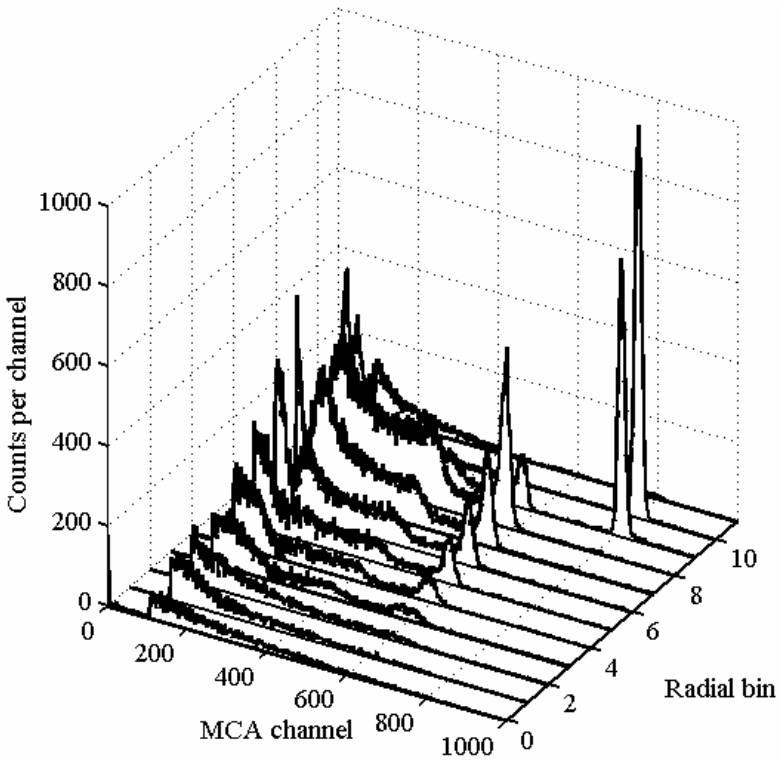

Figure 7.7. Experimental ^{137}Cs energy spectra as a function of radial bin. The peaks near channel 800 in radial bins 9 and 10 are from an injected test pulse.

Table 7.3. A comparison of measured photopeak centroids as a function of radial bin.

Gas	*Rad 0*	*Rad 1*	*Rad 2*	*Rad 3*	*Rad 4*	*Rad 5*	*Rad 6*	*Rad 7*	*Rad 8*	*Rad 9*	*Rad 10*	*Rad 11*
Pure Xe	-	-	-	639	636	635	629	-	-	-	-	-
Xe+H_2	-	-	-	-	593	592	589	585	579	566	-	-

The result of the photopeak alignment is displayed in Figure 7.8, along with the uncorrected and background-stripped spectra for comparison. It is clear that the photopeak alignment noticeably reduces the photopeak width. A test pulse appears near channel 800; the alignment process causes the test peak to be shifted in the final spectrum. The measured energy resolution of the ^{137}Cs source after photopeak alignment is 4.2% FWHM, which is a substantial improvement over the best result in pure Xe, 5.5% FWHM; nearly identical electrode biasing, source geometry, and shaping filter settings were used in these two experiments. The result for detector HPXe1 showed a similar improvement, 4.4% FWHM at 662 keV.

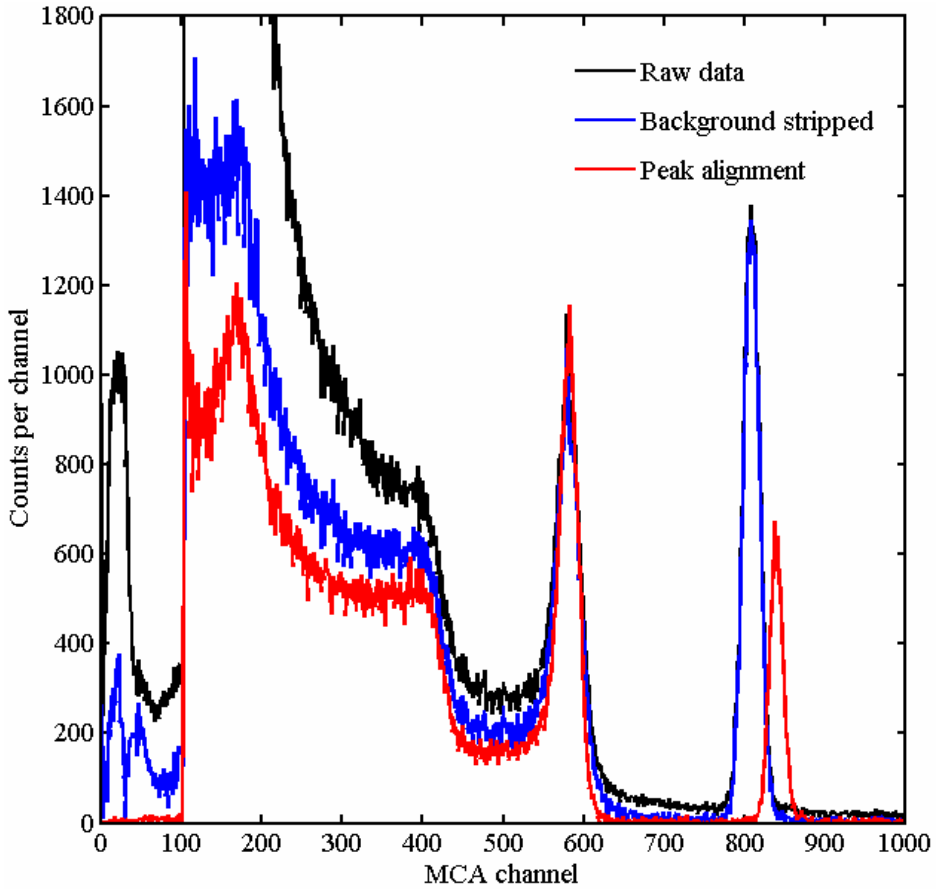

Figure 7.8. A collimated ^{137}Cs raw spectrum compared to the background-stripped and the aligned results; a test pulse appears near channel 800. The aligned resolution is 4.2%.

The next experiment investigated the effect of collimation on the detector performance. Three measurements were made in quick succession with a ^{137}Cs source

and the system settings identical to the last experiment: a collimated plane irradiating the center of the detector, a collimated plane displaced by 1.5 inches (this is only 0.5 inch from the edge of the sensitive volume), and a window collimator that blocks only gammas which might interact in the end regions of the chamber, which are known to have non-ideal responses to radiation interactions. The results are presented in Figure 7.9. The important quantitative results are presented in Table 7.4: the measured photopeak centroid, FWHM, and the peak-to-total count ratio (excluding the test pulse region). The slight upshift in photopeak centroid predicted by the simulations in Chapter 6 are observed here, along with the corresponding broadening as the beam moves closer to the end of the detector. Both of these effects were explained by recombination variation throughout the chamber. The more prominent backscatter peak in the displaced plane and window collimation data is likely due to the increased probability of gammas backscattering off of the thick Macor and steel plates near the end of the pressure vessel.

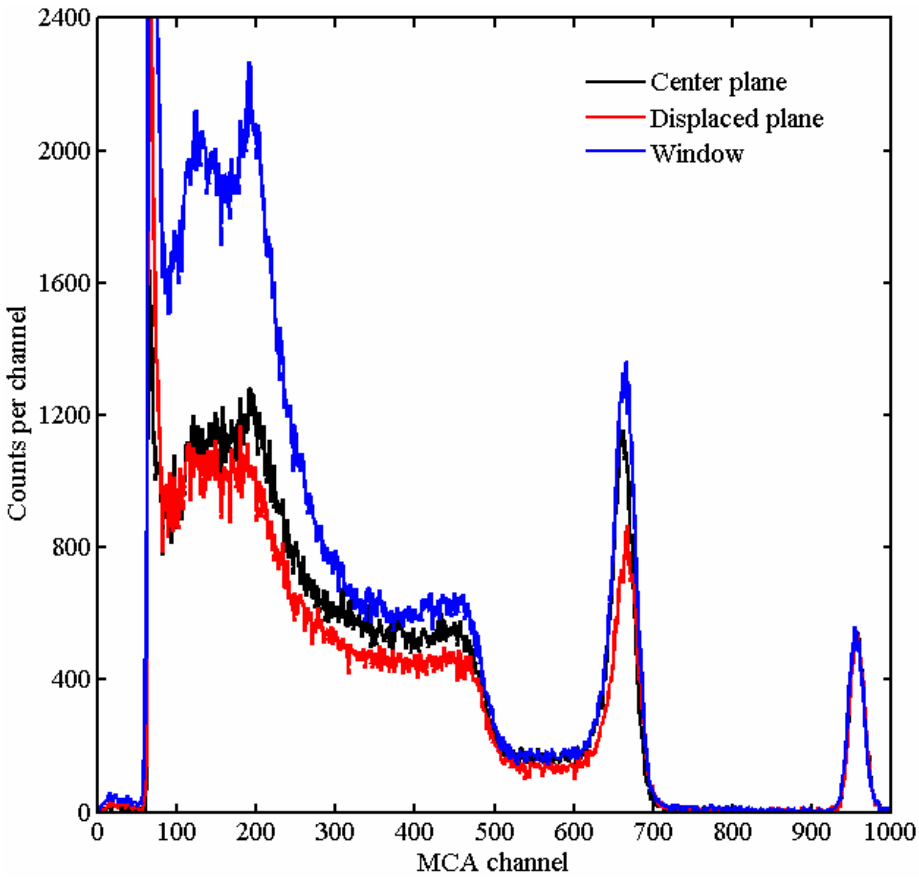

Figure 7.9. A comparison of ^{137}Cs spectra with three different collimator configurations.

Table 7.4. A comparison of spectral parameters in the ^{137}Cs collimation experiment.

Collimation	*Photopeak centroid*	*Photopeak FWHM*	*Peak/total ratio*
Center plane	661.7	30.3	0.0858
Displaced plane	666.2	32.7	0.0724
Window	663.8	31.4	0.0725

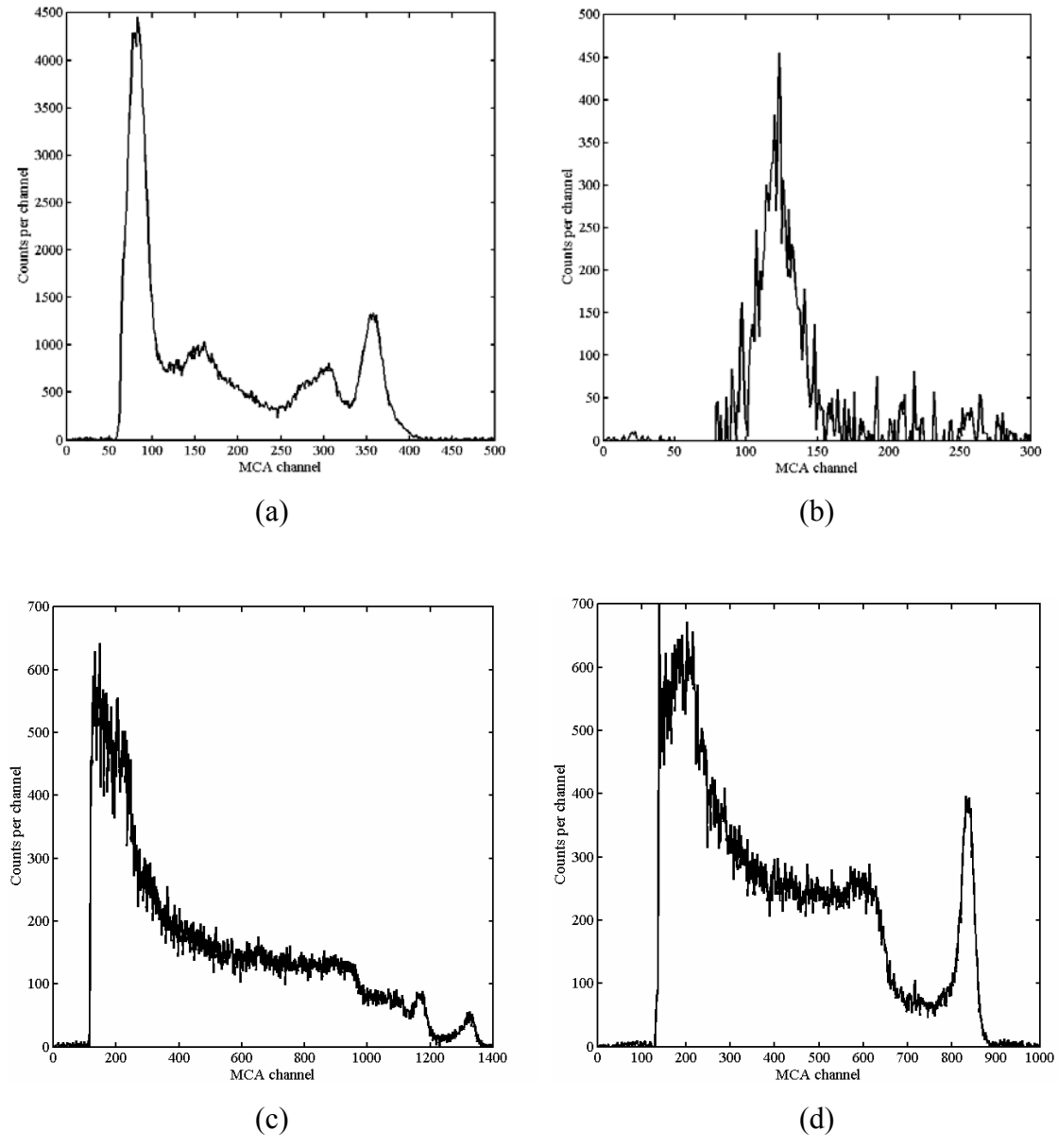

Figure 7.10. Collimated source spectra after photopeak alignment: (a) ^{133}Ba, (b) ^{57}Co, (c) ^{60}Co, (d) ^{54}Mn. All spectra were recorded using the same system settings and counting time.

A final test performed with the HPXe detector was to re-check the measured photopeak linearity and energy resolution trends with several point sources in the central-plane collimation geometry. The system settings were held constant from the previous experiments. The spectra are shown in Figure 7.10 after background stripping and photopeak alignment. The improved energy resolution immediately becomes clear when comparing the ^{60}Co spectrum to the multiple-source spectrum in Figure 4.17: the 1173 keV peak is clearly distinguishable from the 1332 keV line's Compton edge with the improved energy resolution, whereas with pure Xe this measurement could not clearly distinguish the two features.

The measured centroid location and FWHM are listed for each published gamma line in Table 7.5 [93]. The linearity is displayed in Figure 7.11, and a comparison of the intrinsic measured energy resolution—i.e., after electronic noise contributions are subtracted out in quadrature—to a line with the theoretical slope of -½ predicted by Fano carrier statistics is presented in Figure 7.12 [8]. In each plot, the error bars extend a distance of one standard deviation in each direction from the measured centroid or FWHM value, respectively [106].

Table 7.5. Collimated source photopeak data for detector HPXe2.

Source	*Gamma Energy (keV) / Intensity (%)*	*Measured Centroid (channels)*	*Measured FWHM (channels)*
^{133}Ba	81.0 keV (34.1%)	80.9	25.0
^{133}Ba	302.9 keV (18.3%)	306.5	15.2
^{133}Ba	356.0 keV (62.1%)	357.1	24.7
^{57}Co	122.1 keV (85.6%)	120.8	23.3
^{60}Co	1173.2 keV (99.9%)	1168.6	26.7
^{60}Co	1332.5 keV (100.0%)	1324.7	39.5
^{137}Cs	661.7 keV (85.1%)	661.7	30.1
^{54}Mn	834.8 keV (100.0%)	836.4	30.5

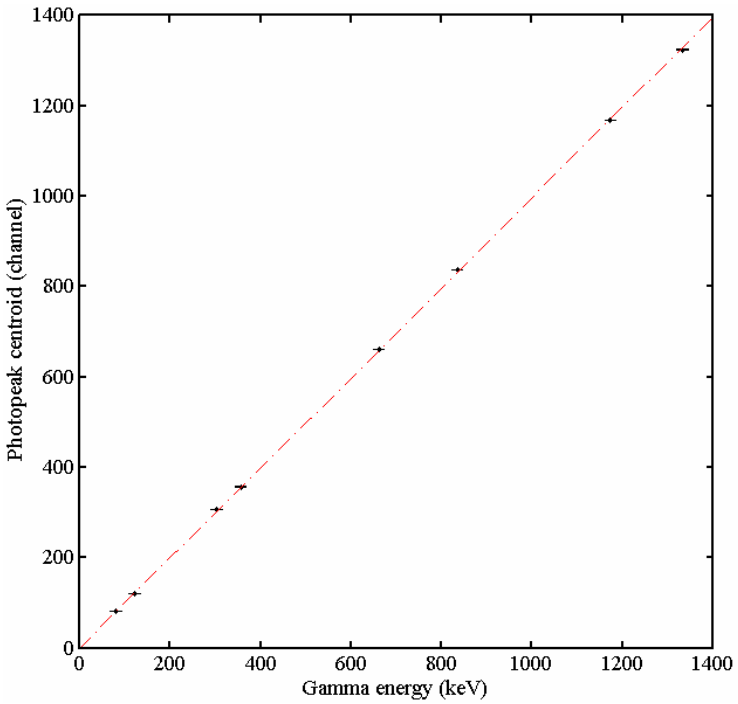

Figure 7.11. A plot of the experimentally-measured photopeak centroids vs. the published gamma-ray energy. The red line represents a linear least-squares fit.

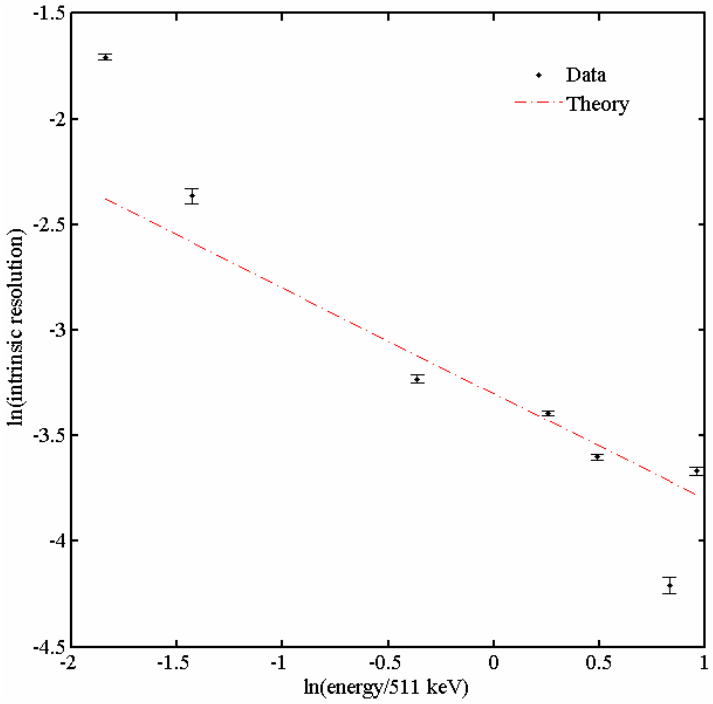

Figure 7.12. A plot of the natural logarithm of the measured intrinsic resolution as a function of the natural logarithm of the normalized gamma-ray energy. The red line shows the theoretical slope if only Fano carrier statistics are important.

In Figure 7.11 it is once again true that excellent linearity is measured with this detector. This result is not necessarily a given, since the amount of charge lost to recombination depends upon the density of ionizations, and is observed to decrease with increasing gamma-ray energy [107]. This effect, however, seems to be negligible.

In Figure 7.12 it seems that at high energies the energy resolution roughly follows the trend predicted if only Fano carrier statistics are significant, although there may be too few data points to make a strong assertion of this observation. At the lowest energy (81.0 keV) the measured resolution seems to depart from the Fano statistics significantly; it should be noted from Figure 7.10(a) that this peak is located very near the discrimination level, potentially impacting the results, although it is expected that the discriminator would seem to improve the energy resolution by cutting off the low-energy side of the distribution. If one considers other physical reasons for the low-energy departure from Fano statistics, the size of the cloud should be beneficial in terms of shaped amplitude uniformity, and the dominance of photoelectric absorptions should reduce broadening due to drift-time differences. One strong possibility is that the electric field is still fairly weak near the outer wall, as evidenced by the sharp drop in the centroid measured near the cathode—see Table 7.3. This effect will tend to impact the low-energy gammas most, since they will not penetrate into the chamber as well as photons of several-hundred keV energies. The low field strength will cause increased charge recombination and poorer energy resolution.

CHAPTER 8

CONCLUSIONS

8.1 Summary of Pure Xenon Experiments and Simulations

The purpose of this coplanar-anode HPXe ionization chamber was to develop a viable alternative to gridded detectors that would not be susceptible to microphonics-induced spectrum degradation. Although no vibrational testing was performed, it seems that this anode design can be made resistant to microphonics, and is therefore reasonable to pursue in future designs. The geometry chosen for this design was based upon simple simulations optimally balancing electronic noise and weighting potential effects.

This detector has fairly low preamplifier input capacitance, measured at 21.9±2.0 pF, most of which is between the two anode sets. This translates into electronic noise limits that are acceptable but fairly high compared to gridded chambers, estimated to be about 2.7% FWHM for 662 keV based upon system measurements. This noise floor, however, was measured with a 6-μs shaping time, which is too short based upon ballistic deficit effects: in practice, the best performance is measured with a 12-μs shaping time constant, meaning the electronic noise is measurably larger than the best-case scenario. Simulations predicted ballistic deficit minimization when using a shaping time near 20 μs, but at that point the electronic noise overwhelms the minimal contribution from nonideal shaping. Probably the largest challenge facing coplanar-anode implementation in HPXe is the unusually high electronic noise, which comes about from the combination of noise from two independent anodes, simplistically increasing the noise FWHM by $\sqrt{2}$ compared to the noise from a comparable gridded chamber, which has only one readout channel. This problem is present in CdZnTe coplanar-anode devices as well, but in those

detectors the number of ionizations per unit energy deposited is greater by a factor of about 4.5, therefore reducing the importance of the electronic noise in relative terms.

The measured energy spectra generally exhibit a very prominent Compton continuum, especially at low energies. This contribution was found to be largely from two detrimental sources: background radiation and interactions in the end regions of the detector. The end regions were shown to provide a poor response to gamma-ray interactions, with no measurable photopeak. For most subsequent experiments, these end regions were shielded to minimize their detrimental contribution to the measured spectra.

Radial position sensing methods were developed and implemented using the existing coplanar anodes. This method is among the first position-sensing efforts in HPXe ionization chambers, and is certainly the most practical to implement. Radial sensing is useful for detector diagnostics and improving the quality of the measured energy spectrum. For example, some of the Compton continuum can be rejected using this information, and photopeak alignment as a function of measured radius can improve the photopeak energy resolution: for data collected with this detector, the energy resolution improved from 5.9% to 5.5% FWHM using peak alignment. In the detector diagnostics realm, data collected using this technique indicates that the weighting potential uniformity is very poor near the anodes, and an improved anode design could help to improve the energy resolution contribution from near-anode events.

A detailed study of photopeak broadening contributions found electronic noise to be the biggest concern, which certainly is verified by experiments. Other important factors include: the collecting anode bias limitation, which reduces the number of counts measured in the photopeak; charge recombination, which reduces the measured peak amplitude while broadening the peak width due to the statistical nature of recombination and the variation in the field strength; and the axial nonuniformity of the weighting and electric fields, which causes the photopeak location to shift while its measured width changes as a function of axial location. All of these effects can be observed experimentally. The simulations predict a resolution limit of about 1% FWHM at 662 keV; the stipulations are that electronic noise must be so inconsequential as to be unmeasurable, and that variations in pulse height as a function of position must be fully compensated on an event-by-event basis.

The impact of multiple-interaction events was also studied with simulations. According to the Geant4 studies, multiple-site events account for about 35% of photopeak events, so their contribution is non-negligible. Multiple-site events were found to degrade the measured energy resolution via broader photopeak width and reduced centroid location. Because these events will often register in the incorrect radius, photopeak alignment actually degrades the contribution from multiple-site events. Unfortunately, this effect is difficult, if not impossible, to quantify experimentally.

The large mass of structural material surrounding the detection volume was found to impact the energy spectrum. By switching volumes between the actual materials and vacuum, the effect of these materials upon the energy spectrum could easily be studied. The energy resolution seems to be impacted negligibly, but the number of photopeak counts is reduced noticeably by the presence of the surrounding scattering sites. Consequently, the relative importance of the Compton continuum is larger with the surrounding materials present, doubling the height of the continuum at the backscatter peak for this particular source energy and location.

8.2 Summary of Xenon+Hydrogen Experiments and Simulations

Cooling admixtures, namely H_2, can be added to the Xe fill gas to improve electron drift speed through the chamber, in some instances by up to a factor of ten. Simulations predict that a sufficient shaping time for minimizing ballistic deficit is 10 μs for just 0.2% H_2, compared to 20 μs for the pure Xe case. Investigations into the physical contributions to photopeak broadening show that the major differences between the pure and doped Xe cases are reduced electronic noise and increased recombination contributions for Xe+H_2, which aligns with expectations and experimental observations.

In experiments with the detectors filled with ~0.2% H_2 gas, the measured energy resolution improved dramatically after photopeak alignment: 4.2% FWHM at 662 keV. The system was shown to have very good linearity over a range extending from about 80 keV up to 1332 keV. The resolution was tracked as a function of gamma-ray energy, and for high energies the trend predicted by Fano statistics held true, although at low energies the data trended toward much higher values. The explanation offered for this observation is the possibility that the electric field is not strong enough near the cathode, resulting in

comparatively large statistical contributions from charge recombination. This effect would apply mostly to low-energy photons, which will tend to be absorbed more readily near the cathode than high-energy particles.

8.3 Suggestions for Future Work

This body of work has shown coplanar-anode HPXe chambers to be a promising concept if the energy resolution can be reduced a little more. Measurements of 4.2% FWHM at 662 keV are getting close to the typical 3.5% to 4.0% measured in gridded chambers of similar diameter. To improve the energy resolution as much as is practical, the possibility of reducing the capacitance between anodes should be studied, as this parameter affects the electronic noise. Only the number of wires was optimized in this detector; optimizing the individual wire diameter and the wire offset from the detector's central axis may be useful studies. Preamplifier transistor cooling to reduce the series noise term may make sense.

The axial response of the detector should be made as uniform as possible, as nonuniformity is a detrimental effect that was measured using source collimation with the current detector. Proper high-voltage design should be considered to allow the collecting anode, as well as the cathode, to be biased optimally. In addition, the fraction of gas volume in regions with poor response, currently more than 25%, should be reduced to decrease the continuum prominence in the energy spectra.

In other efforts to reduce the continuum prominence, an effort to reduce the surrounding structural material may be worthwhile. Some literature cites efforts to use a carbon fiber shell as the pressure vessel, a promising concept. Reducing the thickness of the structural insulating plates inside the chamber is also a good idea.

Enhancing the position-sensing capability of this system is also a possible future activity. These capabilities may help to correct for variations in the detector response throughout the chamber, or may be able to separate single-site events from the resolution-degrading multiple-site events. It is unclear whether a completely different electrode concept, such as anode pixellation, would be required for such capabilities.

If coplanar-anode HPXe detectors are to ever be used in real-world applications, microphonic resistance will need to be proven. Thus, vibrational studies will need to be

performed, preferably with both a coplanar-anode and a gridded HPXe chamber to directly compare results. The current detector did not go through vibrational analysis during the design or testing phase, so it is unlikely that the current geometry is ideal for microphonic resilience.

REFERENCES

1. A.E. Bolotnikov *et al.*, *Properties of Compressed Xe Gas as the Detector Medium for High-Pressure Xe Spectrometers*. *IEEE Nuclear Science Symposium*. 1994. Norfolk, VA: IEEE.

2. C. Levin, J. Germani, and J. Markey, *Charge Collection and Energy Resolution Studies in Compressed Xenon Gas near Its Critical Point.* Nuclear Instruments & Methods A, 1993. **332**(1-2): p. 206-214.

3. V.V. Dmitrenko *et al.*, *High Pressure Xenon Filled Cylindrical Gamma-Ray Detector*. *SPIE 1734: Gamma-Ray Detectors*. 1992. San Diego, CA: SPIE.

4. Gary Tepper, Robert Palmer, and Jon Losee, *High Pressure Xenon Gamma-Ray Spectrometers: Recent Developments and Applications*. *SPIE 3768: Hard X-Ray, Gamma-Ray, and Neutron Detector Physics*. 1999. Denver, CO: SPIE.

5. S.E. Ulin *et al.*, *Influence of Proton and Neutron Fluxes on Spectrometric Characteristics of High Pressure Xenon Gamma-Spectrometer*. *SPIE 3114: EUV, X-Ray, and Gamma-Ray Instrumentation for Astronomy VIII*. 1997. San Diego, CA: SPIE.

6. V.V. Dmitrenko *et al.*, *Radiation Stability of High Pressure Xenon Gamma-Ray Spectrometers*. *1997 IEEE Nuclear Science Symposium*. 1997. Albuquerque, NM: IEEE.

7. Alexander Bolozdynya, Anatoli Arodzero, and Ray DeVito, *High-Pressure Xenon Detectors for Applications in Portal Safeguard Systems and for Monitoring Nuclear Waste*. *43rd Annual INMM Meeting*. 2002. Orlando, FL: Institute of Nuclear Materials Management.

8. Glenn F. Knoll, *Radiation Detection and Measurement*. 3rd ed. 2000, New York: John Wiley & Sons, Inc.

9. Alexander Bolozdynya and Raymond DeVito, *Vibration-Proof High-Pressure Xenon Electroluminescence Detector.* IEEE Transactions on Nuclear Science, 2004. **51**(3): p. 931-933.

10. Alexander Bolozdynya and Raymond DeVito, *Vibration-Proof High-Pressure Xenon Electroluminescence Detector*. *2003 IEEE Nuclear Science Symposium*. 2003. Portland, OR: IEEE.

11. Jeffrey L. Lacy *et al.*, *Cylindrical High Pressure Xenon Spectrometer Using Scintillation Light Pulse Correction*. *2004 IEEE Nuclear Science Symposium*. 2004. Rome, Italy: IEEE.

12. National Institute of Standards and Technology. May 3, 2006, <http://physics.nist.gov/PhysRefData/Xcom/html/xcom1.html>.

13. V.V. Dmitrenko *et al.*, *High-Pressure Xenon Detector to Identify and Monitor Nuclear Materials*. *1996 IEEE Nuclear Science Symposium*. 1996. Anaheim, CA: IEEE.

14. D.H. Beddingfield *et al.*, *High-Pressure Xenon Ion Chambers for Gamma-Ray Spectroscopy in Nuclear Safeguards.* Nuclear Instruments & Methods A, 2003. **505**(1-2): p. 474-477.

15. R.L. Palmer and G.C. Tepper, *Development of a High-Pressure Xenon Ionization Chamber Gamma-Ray Spectrometer for Field Deployment in Cone Penetrometers.* Journal of Radioanalytical and Nuclear Chemistry, 2001. **248**(2): p. 289-294.

16. S.E. Ulin *et al.*, *Cylindrical High-Pressure Xenon Detector of Gamma Radiation.* Instruments and Experimental Techniques, 1994. **37**(2): p. 142-145.

17. Yu.T. Yurkin *et al.*, *Measurement of the Gamma-Ray Lines with High Pressure Xenon Spectrometer on Board of the Orbital Station "MIR"*. *SPIE 2006: EUV, X-Ray, and Gamma-Ray Instrumentation for Astronomy IV*. 1993. San Diego, CA: SPIE.

18. S.E. Ulin *et al.*, *Gamma-Spectrometer XENON for Space-Gamma Bursts Study on Board ISS*. *SPIE 3446: Hard X-Ray and Gamma-Ray Detector Physics and Applications*. 1998. San Diego, CA: SPIE.

19. A.S. Barabash *et al.*, *Low Background Installation for the ^{136}Xe Double Beta Decay Experiment.* Nuclear Instruments & Methods B, 1986. **17**(5-6): p. 450-451.

20. C. Levin and J. Markey, *Compressed Xenon Gas near Its Critical Point as an Ionization Medium.* IEEE Transactions on Nuclear Science, 1993. **40**(4): p. 642-644.

21. O. Bunemann, T.E. Cranshaw, and J.A. Harvey, *Design of Grid Ionization Chambers.* Canadian Journal of Research, Section A, 1949. **27**(5): p. 191-206.

22. A.M. Galper *et al.*, *The Possibility of Creation of High Sensitive Gamma-Telescopes Based on Pressed Xe for 0.1-10 MeV Energy Range*. *17th International Cosmic Ray Conference*. 1981. Paris: University of Denver.

23. V.V. Dmitrenko *et al.*, *Compressed-Xenon Ionization Chamber for Gamma Spectrometry.* Instruments and Experimental Techniques, 1986. **29**(1): p. 14-17.

24. A.S. Barabash, V.M. Novikov, and B.M. Ovchinnikov, *High Pressure Ionization Chamber Designed to Search for 2β Decay of ^{136}Xe.* Nuclear Instruments & Methods A, 1991. **300**(1): p. 77-79.

25. V.V. Dmitrenko *et al.*, *Compressed Gaseous Xenon Gamma-Ray Detector with High Energy Resolution*. *SPIE 1734: Gamma-Ray Detectors*. 1992. San Diego, CA: SPIE.

26. S.V. Krivov *et al.*, *Measurement of Background 0.1-2.0 MeV Gamma-Ray Radiation on Board of the Orbital Station "MIR"*. *SPIE 2280: EUV, X-Ray, and Gamma-Ray Instrumentation for Astronomy V*. 1994. San Diego, CA: SPIE.

27. Gary Tepper and Jon Losee, *High Resolution Room Temperature Ionization Chamber Xenon Gamma Radiation Detector.* Nuclear Instruments & Methods A, 1995. **356**(2-3): p. 339-346.

28. V.V. Dmitrenko *et al.*, *High Pressure Xenon Gamma-Spectrometers with High Energy Resolution*. *IEEE Nuclear Science Symposium*. 1996. Anaheim, CA: IEEE.

29. K.F. Vlasik *et al.*, *High-Pressure Xenon γ-Ray Spectrometers.* Instruments and Experimental Techniques, 1999. **42**(5): p. 685-692.

30. V.V. Dmitrenko *et al.*, *High-Pressure Xenon Detectors for Gamma-Ray Spectrometry.* Applied Radiation and Isotopes, 2000. **52**(3): p. 739-743.

31. V.V. Dmitrenko *et al.*, *Vibrostability of High Pressure Xenon Gamma-Ray Detectors*. *1999 IEEE Nuclear Science Symposium*. 1999. Seattle, WA: IEEE.

32. V.V. Dmitrenko *et al.*, *Vibrostability of High Pressure Xenon Gamma-Ray Detectors.* IEEE Transactions on Nuclear Science, 2000. **47**(3): p. 939-943.

33. A.E. Bolotnikov *et al.*, *Factors Determining Energy Resolution of Compressed-Xenon Gamma Spectrometers at Densities of >0.6 g/cm^3.* Instruments and Experimental Techniques, 1987. **29**(4): p. 802-804.

34. Josef R. Parrington *et al.*, *Nuclides and Isotopes: Chart of the Nuclides*. 15th ed. 1996, San Jose, CA: General Electric Co. and KAPL, Inc. 64.

35. G.J. Mahler *et al.*, *A Portable Gamma-Ray Spectrometer Using Compressed Xenon.* IEEE Transactions on Nuclear Science, 1998. **45**(3): p. 1029-1033.

36. S.E. Ulin *et al.*, *High Pressure Xenon Cylindrical Ionization Chamber with a Shielding Mesh*. *SPIE 2305: Gamma-Ray Detector Physics and Applications*. 1994. San Diego, CA: SPIE.

37. S.E. Ulin *et al.*, *A Cylindrical Ionization Chamber with a Shielding Mesh Filled with Xenon under a Pressure of 50 atm.* Instruments and Experimental Techniques, 1995. **38**(3): p. 326-330.

38. S.E. Ulin *et al.*, *High Pressure Xenon Gamma-Ray Large Volume Spectrometer*. *SPIE 2806: Gamma-Ray and Cosmic-Ray Detectors, Techniques, and Missions*. 1996. Denver, CO: SPIE.

39. Gary Tepper, Jon Losee, and Robert Palmer, *Development of a High-Resolution, Room Temperature Compressed-Xenon Cylindrical Ionization Chamber Gamma Radiation Detector*. *SPIE 3446: Hard X-Ray and Gamma-Ray Detector Physics and Applications*. 1998. San Diego, CA: SPIE.

40. Gary Tepper, Jon Losee, and Robert Palmer, *A Cylindrical Xenon Ionization Chamber Detector for High Resolution, Room Temperature Gamma Radiation Spectroscopy.* Nuclear Instruments & Methods A, 1998. **413**(2-3): p. 467-470.

41. S. Ottini-Hustache *et al.*, *HPXe Ionization Chambers for γ Spectrometry at Room Temperature.* Nuclear Instruments & Methods B, 2004. **213**: p. 279-283.

42. V.V. Dmitrenko *et al.*, *The Progress in Developing of Large Volume High Pressure Xenon Gamma-Ray Spectrometers*. *13th International Conference on Dielectric Liquids*. 1999. Nara, Japan: IEEE.

43. S.E. Ulin *et al.*, *Gamma-Ray Spectrometric Equipment for Detecting Nuclear Materials*. *SPIE 3768: Hard X-Ray, Gamma-Ray, and Neutron Detector Physics*. 1999. Denver, CO: SPIE.

44. Aleksey Bolotnikov and Brian Ramsey, *Improving the Energy Resolution of High-Pressure Xe Cylindrical Ionization Chambers.* IEEE Transactions on Nuclear Science, 1997. **44**(3): p. 1006-1010.

45. Aleksey Bolotnikov and Brian Ramsey, *Development of High-Pressure Xenon Detectors*. *SPIE 3446: Hard X-Ray and Gamma-Ray Detector Physics and Applications*. 1998. San Diego, CA: SPIE.

46. S.E. Ulin *et al.*, *Gamma-Neutron Measurement Complex for Detection and Identification of Radioactive and Fissile Materials*. *SPIE 4784: X-Ray and Gamma-Ray Detectors and Applications IV*. 2002. Seattle, WA: SPIE.

47. Albert Beyerle, *Stability of High-Pressure Xenon Gamma-Ray Spectrometers*. *SPIE 5922: Hard X-Ray and Gamma-Ray Detector Physics VII*. 2005. San Diego, CA: SPIE.

48. S.E. Ulin *et al.*, *Gamma-Detectors Based on High Pressure Xenon: Their Development and Application*. *SPIE 5540: Hard X-Ray and Gamma-Ray Detector Physics VI*. 2004. Denver, CO: SPIE.

49. Aleksey Bolotnikov, *New Developments in High-Pressure Xe Ionization Chambers, New Surprises of Fluid Xe*. Instrumentation Division Seminar, January 5, 2005. Brookhaven National Laboratory, Upton, NY.

50. V.V. Dmitrenko *et al.*, *A Cylindrical Ionization Chamber for Low-Energy (0.1-3-MeV) γ-Ray Spectrometry.* Instruments and Experimental Techniques, 1982. **24**(5): p. 1146-49.

51. V.B. Komarov *et al.*, *Calculation of Characteristics of Compressed Gaseous Xenon Gamma-Ray Detectors*. *SPIE 1734: Gamma-Ray Detectors*. 1992. San Diego, CA: SPIE.

52. V.V. Dmitrenko *et al.*, *A Thermostable High Pressure Xenon Gamma-Ray Detector for Monitoring Concentration of KCl During Fertilizer Manufacturing.* Nuclear Instruments & Methods A, 1999. **422**(1-3): p. 326-330.

53. J.L. Lacy, C.S. Martin, and L.P. Armendarez, *High Pressure Xenon Proportional Tube Detector for Tc-99m Imaging*. *2000 IEEE Nuclear Science Symposium*. 2000. Lyon, France: IEEE.

54. G.L. Troyer, B.D. Keele, and G.C. Tepper, *Pulse Rise-Time Characterization of a High Pressure Xenon Gamma Detector for Use in Resolution Enhancement.* Journal of Radioanalytical and Nuclear Chemistry, 2001. **248**(2): p. 267-271.

55. M.K. Smith, E.A. McKigney, and A.G. Beyerle, *Modeling High Pressure Xenon with Geant*. *7th International Conference on Facility Operations - Safeguards Interface*. 2004. Charleston, SC: American Nuclear Society.

56. Gary Tepper and Jon Losee, *A Compressed Xenon Ionization Chamber X-Ray/Gamma-Ray Detector Incorporating Both Charge and Scintillation Collection.* Nuclear Instruments & Methods A, 1996. **368**(3): p. 862-864.

57. V.V. Dmitrenko *et al.*, *Spectrometric Applications of an Ionization-Type Drift Chamber.* Instruments and Experimental Techniques, 1982. **25**(1): p. 50-53.

58. A.E. Bolotnikov *et al.*, *Virtual Frisch-Grid Ionization Chambers Filled with High-Pressure Xe*. *SPIE 5540: Hard X-Ray and Gamma-Ray Detector Physics VI*. 2004. Denver, CO: SPIE.

59. Royal Kessick and Gary Tepper, *A Hemispherical High-Pressure Xenon Gamma Radiation Spectrometer.* Nuclear Instruments & Methods A, 2002. **490**(1-2): p. 243-250.

60. Clair J. Sullivan, *Single Polarity Charge Sensing in High Pressure Xenon Using a Coplanar Anode Configuration*. Nuclear Engineering and Radiological Sciences. 2002, Ann Arbor: University of Michigan.

61. C.J. Sullivan *et al.*, *A High Pressure Xenon Gamma-Ray Spectrometer Using a Coplanar Anode Configuration.* Nuclear Instruments & Methods A, 2003. **505**(1-2): p. 238-241.

62. Aleksey Bolotnikov *et al.*, *Dual-Anode High-Pressure Xenon Cylindrical Ionization Chamber.* IEEE Transactions on Nuclear Science, 2004. **51**(3): p. 1262-1269.

63. A. Bolozdynya *et al.*, *Detection of Thermal Neutrons in Cylindrical Ionization Chamber Filled with High-Pressure Xe+^{3}He Gas Mixture.* Nuclear Instruments & Methods A, 2004. **522**(3): p. 595-597.

64. A.I. Bolozdynya and A.E. Bolotnikov, *Threshold Dependence of Fluctuations of Thermal Neutron Ionization Yield on Density of Xe+^{3}He Gas Mixture*. *2005 IEEE International Conference on Dielectric Liquids*. 2005. Coimbra, Portugal: IEEE.

65. Yuxin Feng *et al.*, *A Pixelated Design of High Pressure Xenon Gamma-Ray Spectrometer.* Nuclear Instruments & Methods A, submitted for publication.

66. Allen Seifert *et al.*, *Implementation of a Noise Mitigation Strategy for a High-Pressure Xenon Detector*. *2005 IEEE Nuclear Science Symposium*. 2005. Fajardo, Puerto Rico: IEEE.

67. N.G. Goleminov, B.U. Rodionov, and V.Yu. Chepel, *Position-Sensitive Xenon Gamma-Quantum Detector.* Instruments and Experimental Techniques, 1986. **29**(2): p. 325-328.

68. Athanasios Athanasiades, Jeffrey L. Lacy, and Liang Sun, *Position Sensing in a Cylindrical Ionization Detector through Use of a Segmented Cathode*. *2001 IEEE Nuclear Science Symposium*. 2001. San Diego, CA: IEEE.

69. A. Athanasiades *et al.*, *Position Sensing in a Cylindrical Ionization Detector with a Resistive Cathode.* Nuclear Instruments & Methods A, 2003. **505**(1-2): p. 252-255.

70. W. Shockley, *Currents to Conductors Induced by a Moving Point Charge.* Journal of Applied Physics, 1938. **9**(10): p. 635-636.

71. S. Ramo, *Currents Induced by Electron Motion*. *Proceedings of the IRE*. 1939.

72. Zhong He, *Review of the Shockley-Ramo Theorem and Its Application in Semiconductor Gamma-Ray Detectors.* Nuclear Instruments & Methods A, 2001. **463**(1-2): p. 250-267.

73. O. Frisch, *British Atomic Energy Report BR-49*. 1944.

74. P.N. Luke, *Single-Polarity Charge Sensing in Ionization Detectors Using Coplanar Electrodes.* Applied Physics Letters, 1994. **65**(22): p. 2884-2886.

75. Zhong He and Mark H. Khachaturian, *Potential Distributions and Critical Bias Voltages for Complete Preferential Charge Collection Using Periodic Coplanar Electrodes.* Nuclear Instruments & Methods A, unpublished.

76. Zhong He, *Potential Distribution within Semiconductor Detectors Using Coplanar Electrodes.* Nuclear Instruments & Methods A, 1995. **365**(2-3): p. 572-575.

77. P.N. Luke, *Unipolar Charge Sensing with Coplanar Electrodes--Application to Semiconductor Detectors.* IEEE Transactions on Nuclear Science, 1995. **42**(4): p. 207-213.

78. Zhong He *et al.*, *1-D Position Sensitive Single Carrier Semiconductor Detectors.* Nuclear Instruments & Methods A, 1996. **380**(1-2): p. 228-231.

79. Zhong He and Ben W. Sturm, *Characteristics of Depth-Sensing Coplanar Grid CdZnTe Detectors.* Nuclear Instruments & Methods A, 2005. **554**(1-3): p. 291-299.

80. CRC Handbook of Chemistry and Physics, *Permittivity (Dielectric Constant) of Gases*. Dr. David R. Lide, Editor. 2004, CRC Press: Cleveland, OH. p. 6-174.

81. William E. Boyce and Richard C. DiPrima, *Elementary Differential Equations and Boundary Value Problems*. 6th ed. 1997, New York: John Wiley & Sons, Inc. 669.

82. Peter V. O'Neil, *Advanced Engineering Mathematics*. 4th ed. 1995, Pacific Grove, CA: Brooks/Cole Publishing Company.

83. Erwin Kreyszig, *Advanced Engineering Mathematics*. 8th ed. 1999, New York: John Wiley & Sons, Inc.

84. Zhong He and Mark Haig Khachaturian, *Analytical Derivation of Critical Bias Voltage for Complete Electron Collection in 2D Radial Room Temperature Semiconductors Using Alternating Electrodes*. 2001, Ann Arbor: University of Michigan.

85. Ansoft Corporation, *Maxwell 3D*. Version 9, 2003: <http://www.ansoft.com/products/em/max3d/>.

86. Wolfram Research Inc., *Mathematica for Students*. Version 4.1.1.0, 2000: <www.wolfram.com>.

87. Amptek Inc., *Amptek A250 Specification Sheet*. 12 September 2003, <http://www.amptek.com/a250.html>.

88. CERN, *Geant4*. Version 4.5.2, 2003: <http://geant4.web.cern.ch/geant4/>.

89. Z. He *et al.*, *Position-Sensitive Single Carrier CdZnTe Detectors.* Nuclear Instruments & Methods A, 1997. **388**(1-2): p. 180-185.

90. Corning Incorporated, *MACOR Product Data Sheet*. July 28, 2006, <http://www.corning.com/lightingmaterials/products/index_macor.html>.

91. Aleksey Bolotnikov and Brian Ramsey, *Purification Techniques and Purity and Density Measurements of High-Pressure Xe.* Nuclear Instruments & Methods A, 1996. **383**(2-3): p. 619-623.

92. EG&G ORTEC, *MAESTRO for Windows*. Version 5.10, 1999: <http://www.ortec-online.com/pdf/a65.pdf>.

93. Brookhaven National Laboratory National Nuclear Data Center. September 13, 2006, <http://www.nndc.bnl.gov/chart/>.

94. J.L. Pack, R.E. Voshall, and A.V. Phelps, *Drift Velocities of Slow Electrons in Krypton, Xenon, Deuterium, Carbon Monoxide, Carbon Dioxide, Water Vapor, Nitrous Oxide, and Ammonia.* The Physical Review, 1962. **127**(6): p. 2084-89.

95. The MathWorks Inc., *Matlab*. Version 7.0.1, 2004: <http://www.mathworks.com/products/matlab/>.

96. Aleksey Bolotnikov and Brian Ramsey, *The Spectroscopic Properties of High-Pressure Xenon.* Nuclear Instruments & Methods A, 1997. **396**(3): p. 360-370.

97. Scott D. Kiff, Zhong He, and Gary C. Tepper, *A New Coplanar-Grid High-Pressure Xenon Gamma-Ray Spectrometer.* IEEE Transactions on Nuclear Science, 2005. **52**(6): p. 2932-2939.

98. Vladimir M. Atrazhev, Irina V. Chernysheva, and Tadayoshi Doke, *Transport Properties of Electrons in Gaseous Xenon.* Japanese Journal of Applied Physics, Part 1, 2002. **41**(3A): p. 1572-1578.

99. National Instruments, *LabVIEW*. Version 8.0, 2006: <http://www.ni.com/labview/>.

100. National Instruments. October 4, 2006, <http://sine.ni.com/nips/cds/view/p/lang/en/nid/11888>.

101. Z. He *et al.*, *3-D Position Sensitive CdZnTe Gamma-Ray Spectrometers.* Nuclear Instruments & Methods A, 1999. **422**(1-3): p. 173-178.

102. G. Manzo *et al.*, *Preliminary Studies of Gas Fillings in Gas Scintillation Proportional Counters.* IEEE Transactions on Nuclear Science, 1980. **NS-27**(1): p. 204-207.

103. Aleksey E. Bolotnikov, *Re: High-Pressure Xenon*. January 6, 2006. E-mail Communication.

104. V. Palladino and B. Sadoulet, *Application of Classical Theory of Electrons in Gases to Drift Proportional Chambers.* Nuclear Instruments and Methods, 1975. **128**(2): p. 323-335.

105. NuPure Corporation, *NuPure E0040-CA-VR4-H2-XL Room Temperature Getter Product Specifications*. November 13, 2006, <http://www.nupure.com/Pages/eliminatorCA.htm>.

106. John D. Valentine and Asad E. Rana, *Centroid and Full-Width at Half Maximum Uncertainties of Histogrammed Data with an Underlying Gaussian Distribution--the Moments Method.* IEEE Transactions on Nuclear Science, 1996. **43**(5): p. 2501-2508.

107. A.E. Bolotnikov *et al.*, *Electron-Ion Recombination on Electron Tracks in Compressed Xenon.* Soviet Physics - Technical Physics, 1988. **33**(4): p. 449-454.